The Prediction of Cavitation in High Speed Centrifugal Pumps

by

Matthew John Richings

In fulfilment of the academic requirements for the degree of Master of Science in Mechanical Engineering, College of Agriculture, Engineering and Science, University of KwaZulu-Natal.

Supervisor: Professor Graham Smith
Co-Supervisors: Mr Michael Brooks
Dr. Glen Snedden (CSIR)

Declaration

I Matthew John Richings declare that

(i) The research reported in this dissertation/thesis, except where otherwise indicated, is my original work.

(ii) This dissertation/thesis has not been submitted for any degree or examination at any other university.

(iii) This dissertation/thesis does not contain other persons' data, pictures, graphs or other information, unless specifically acknowledged as being sourced from other persons.

(iv) This dissertation/thesis does not contain other persons' writing, unless specifically acknowledged as being sourced from other researchers. Where other written sources have been quoted, then:

a) their words have been re-written but the general information attributed to them has been referenced;

b) where their exact words have been used, their writing has been placed inside quotation marks, and referenced.

(v) Where I have reproduced a publication of which I am an author, co-author or editor, I have indicated in detail which part of the publication was actually written by myself alone and have fully referenced such publications.

(vi) This dissertation/thesis does not contain text, graphics or tables copied and pasted from the Internet, unless specifically acknowledged, and the source being detailed in the dissertation/thesis and in the References sections.

Signed:

.....

Mr Matthew John Richings

As the candidate's Supervisor I agree/do not agree to the submission of this thesis.

Signed:

.....

Prof. Graham Smith

Acknowledgements

I would like to thank my supervisors Prof. Graham Smith, Mr. Michael Brooks and Dr. Glen Snedden for their support and guidance in this project. Special thanks must also be given to Prof. Stefan Rosler from the University of Esslingen for inviting me to learn from him and his team in Germany.

The financial assistance of the National Research Foundation (NRF) towards this research is hereby acknowledged. Opinions expressed and conclusions arrived at, are those of the author and are not necessarily to be attributed to the NRF.

This work was also funded by the Armscor BALLAST program.

Abstract

The primary focus of this research was to analyse the flow through a high speed centrifugal turbopump and validate the original meanline design. This research forms part of a larger project which is to develop a kerosene turbopump capable of launching a hypothetical vehicle into a sun synchronous orbit. The original design work was done by Smyth (2013) which dealt with the design of the impeller. The next step, dealt with by Philogene (2014), was concerned with an experimental test rig capable of testing a scaled version of the original impeller. Unfortunately the test rig has not yet provided experimental data for the impeller leaving the meanline design as the only source of comparison for this project.

Before undertaking the computational analysis of the high speed impellers, a review was conducted into the parameters that should be used in the computational fluid dynamic models. The optimum mesh configuration was determined to be unstructured polyhedral cells away from the walls and prismatic layers near the walls to accurately capture the boundary layer flow.

The SST K-Omega turbulence model was deemed sufficient to model the turbulent eddies within the flow. The steady state models were run using a rotating reference frame which was applied to the impeller region of the model. The steady state results for the scaled impeller deviated from the meanline analysis by 12% at the operating point. This deviation increased as the flow rate was increased. The full scale model provided excellent steady state results with regards to the agreement with the meanline design. At the operating point of the full scale rotor, the difference between the results was only 1.31%. At 130% of the operating flow rate the difference between the two sets of results was only 8.5%, a remarkable improvement from the scaled impeller.

In order to model the cavitation performance of each impeller an unsteady analysis was conducted. A multiphase flow model, the Volume of Fluid model, was employed. This model recognises that the flow has two separate fluid phases present. The formulation of cavitation bubbles was then controlled by the Rayleigh Plesset Equation which determines the changing bubble radius.

The results of the cavitation modelling showed no significant change in the scaled impeller performance, which exhibited less cavitation. The low percentage of cavitating flow also meant that the flow was stable in terms of the pressure outlet fluctuations. However, the full scale model contained a much larger cavitating percentage of flow. This drastically affected the performance of the impeller, dropping the outlet pressure by 11 b at the operating point. Although both impellers were designed to exhibit similar levels of cavitation, the numerical results show differences which could be due to the complex process of cavitation scaling.

Table of Contents

List of Figures

List of Tables

Nomenclature

α	Volume fraction
β^*	Closure coefficient
C_μ	Closure coefficient
δ_{ij}	Kronecker delta
ϵ	Dissipation per unit mass
H	Head rise
I_{SP}	Specific impulse
k	Kinetic energy of turbulent fluctuations
ℓ	Turbulence length scale
n_0	Number of bubbles per unit volume
P	Static pressure
P_c	Critical pressure
P_g	Gas pressure
P_0	Total pressure
P_v	Vapour pressure
P_∞	Pressure outside the bubble
Q	Flow rate
ρ	Density
R	Radius of microbubble
R_c	Critical bubble radius
σ	Cavitation number
S	Surface tension
SF	Scaling factor
S_{ij}	Mean strain rate tensor
s_{ij}	Instantaneous strain rate tensor
τ_w	Wall shear stress
τ_{ij}	Reynolds stress tensor
t	Time
t_{ji}	Viscous stress tensor
U_i	Mean velocity in tensor notation
u_i	Instantaneous velocity in tensor notation
u^*	Reference velocity
μ	Molecular viscosity

μ_T	Eddy viscosity
$\overline{u'_j u'_i}$	Temporal average of fluctuating velocities
V	Volume
V_g	Volume of gas
V_l	Volume of liquid
ν	Kinematic viscosity
ν_t	Kinematic turbulent viscosity
ω	Specific dissipation rate
x_i	Position vector in tensor notation
y	Half the near wall cell thickness

1 Introduction

To lay the foundation for a broader knowledge base of liquid propellant rockets, UKZN's Aerospace Research Group started a liquid rocket programme four years ago. The first work in this project involved the design of a kerosene turbopump for a hypothetical launch vehicle. The project that followed dealt with the design of a high speed turbopump test facility which was meant to provide experimental data for the turbopump through the testing of a scaled down impeller, but has not yet been completed. This project provides a three dimensional numerical solution for both the scaled down and full size impellers with the goal of offering a methodology, to verify the one dimensional meanline approach that was used in the original design work. This is intended to be supplemented by results from an experimental rig that is under development separately. The CFD work can also validate the scaling process used to design the scaled down impeller and test rig.

The liquid turbopump was designed to be part of an engine system of a vehicle capable of launching 50-500 kg payloads into a 500 km circular, sun synchronous orbit (Smyth, 2013). The design was based on performance analyses which were conducted using one dimensional and quasi three dimensional calculations. The design was kept relatively simple to keep in line with the purpose of launching at modest cost from a South African site. The simplicity of the design meant the pump was designed to only use a single centrifugal impeller stage without a separate inducer. These factors lead to a turbopump which is to run at 14500 rpm while generating 889 m of head at a flow rate of 103.3 kg/s and consuming 1127.8 kW of power. The impeller itself has 6 blades with an outer diameter of 186.7 mm (Smyth, 2013).

The performance characteristics of the turbopump made it impractical to test in a laboratory setting. This meant that a scaled down version of the impeller had to be designed to allow for experimental testing to take place. The scaled impeller was designed according to the Buckingham Pi Theorem of scaling. The scaled impeller has a geometric reduction of 20% and uses water as a medium rather than kerosene. The scaled impeller is designed to run at 5000 rpm and produces a total dynamic head rise of 67.7 m at a flow rate of 18.2 kg/s.

The purpose of the CFD project was to bridge the gap between the experimental rig and the meanline design. This analysis was not intended to play the role of a validating source for the meanline design but the lack of experimental data has left only two sets of results which can be compared at this stage. The experimental rig was intended to provide data for the scaled impeller and in doing so provide the validation of the meanline design for this smaller impeller. The CFD study was then going to be

compared to the meanline design as well as the experimental data. Ideally all three results would correspond and the CFD model would therefore have validation. Validating the CFD model for the scaled impeller through the experimental rig provides indirect validation for the full scale CFD model as both (scaled and full scale) CFD models were designed with the same physics models and boundary conditions. In other words, by verifying the scaled impeller CFD model with experimental testing, the full scale numerical model would have the same validation. This full scale CFD model would then be compared to the meanline analysis and provide validation or point in the direction of a redesign. Unfortunately, the experimental rig remains incomplete such that the only comparison that could be made for the impellers was between the CFD results and the meanline data provided by Smyth (2013). The lack of experimental data necessitates that the cavitation performance of the numerical model be judged using outlet pressure data. Confidence in the CFD analysis could also be obtained through the fact that the literature review provided insight into similar CFD analyses.

1.1 Rocket Engines

Rocket engines have various different forms and make use of a number of different propellants. The three main categories of rocket engines are solid, hybrid and liquid rocket engines. The higher performance and easier control of liquid rocket engines has meant that they are the most suitable for commercial launch vehicles when compared to hybrid or solid rocket engines (Sutton, 2006). Another major advantage of liquid propellant rocket engines is the fact that they can be re-fuelled. This allows for ground testing to be done which leads to the greatly increased reliability of these engines. The re-fuelling also brings about the concept of re-usability. Reusability of a rocket engine would dramatically decrease the cost of commercial space rockets and hence it is an important design goal in the commercial launch industry (SpaceX, 2011).

In a liquid rocket engine there are two ways for the propellant to be supplied to the combustion chamber at the specified pressure and flow rate. One method of doing this is to pre-pressurise the propellant while the other option involves the use of a turbopump. Martensson, et al., (2008) discuss in great detail, the different types of rocket engines and describe a turbopump as a pump which is driven by a turbine running off combustion gases. The use of a turbopump allows for a lower vehicle mass as the propellant feed tank does not have to be pressurised and therefore can be significantly lighter. This improves the vehicles mass fraction (ratio of propellant mass to total launch mass) as well as the overall performance. Turbopumps also generate a longer and more consistent burn since they do not suffer from a decreasing output pressure. Despite the lower mass fraction, turbopumps do add complexities to the design. Rocket engines require high efficiency as well as low weight,

conditions best met with high head rise and flow rate. Generally a small diameter pump operating at high speeds is favoured as discussed by Smyth (2013) in the original design work of the turbopump.

Within liquid rocket engines there are various engine cycles that can be used. The difference between the cycles is principally in the configuration of the propellant feed system. These cycles include the expander cycle, the staged combustion cycle and the gas generator cycle. In the design of the hypothetical launch vehicle, the gas generator cycle was selected due to its simplicity. The simplicity of this cycle also makes it the most common engine cycle in use. The gas generator cycle involves the turbine being driven by a small portion of the propellant which is shown in the diagram produced by Martensson, et al., (2008) and can be seen in the figure 1.1. This propellant line runs parallel to the main propellant line which causes a decrease in specific impulse I_{SP} (the ratio of the thrust to the amount of fuel used per unit of time) which can be minimised by re-routing the turbine exhaust back into the nozzle to be further expanded (Smyth, 2013). The gas generator cycle is the easiest to control due to the direct relationship between the amount of propellant burnt and the engine's behaviour. The outlet pressure of the turbopump is determined by the chamber pressure and needs to be just above that of the chamber. Early in the design of the hypothetical launch vehicle the chamber pressure was calculated to be 50 b. This was determined by Smyth (2013) using the vehicle's I_{sp} (300 s) and the nozzle discharge pressure (1 b). The chamber pressure and the drop in the line meant that the turbopump needed to produce a pressure of 75 b to provide the chamber with sufficient pressure. This shows the high demands placed on a turbopump commonly used in a rocket engine cycle.

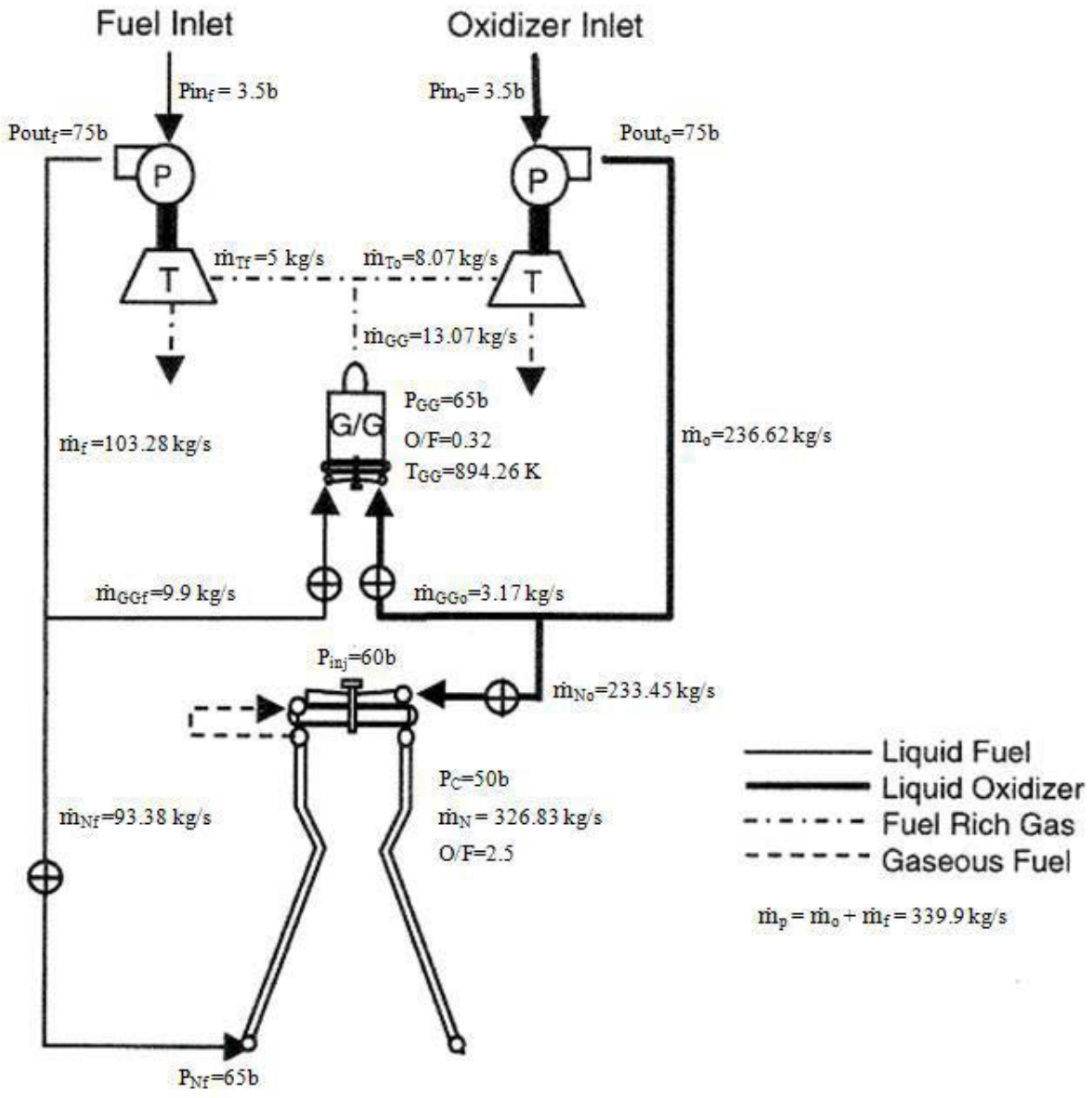

Figure 1.1: Gas generator cycle with vehicle parameters (Smyth, 2013)

1.2 Computational Fluid Dynamics (CFD)

Qiu, et al., (2010) explained that the design process generally used in turbomachinery has various different levels, with each level having a separate function. The first step of the integrated design system is the analysis of the system as a whole which was done by Smyth (2013). This involves identifying the type of machinery needed as well as the basic operating conditions of the stage/machine. The next level is the one dimensional (1D) meanline analysis where the design requirements are specified. The idea is to determine the flow path and geometry as well as the potential performance of the machine. The 1D analysis has a fast turnaround time but the reliance on empirical models means that careful validation is required to ensure the integrity of the result. The

meanline program is the starting point of a new design. The meanline process performs two main tasks. The first is the production of a new design with specified operating conditions. The second task is to predict the performance of an existing design with the secondary tasks including choke, stall and cavitation predictions.

Once the 1D results have been developed, a 3D geometry for the flow path and blading can be generated. This geometry can be refined through the use of 2D and 3D solvers by interactively altering certain geometric details until a final optimized design has been reached. However, the addition of an extra dimension (3D) means the solver run time will be increased. The highest level of analysis is full three dimensional CFD. However, this is the most computationally expensive solver as it allows the entire flow field to be resolved with minimal compromise. The design can be further refined by using CFD to achieve the desired flow field. As the design space is narrowed through the integrated design process, the optimization process becomes more efficient making CFD the best tool for detailed optimization. Once the numerical solution for the entire flow field has been computed using CFD the results can be compared to the original design. If the 3D numerical solution does not meet certain output criteria, the designer must move back to the 1D meanline program to possibly refine the design and alter the geometry.

CFD is a very powerful engineering tool that allows a wide variety of flow scenarios to be simulated and understood whilst also having the additional advantages that it can either reduce the amount of testing required or it can be used to validate certain tests.

CFD calculations are based on the three essential equations of fluid dynamics, namely: the conservation of mass, momentum and energy. These equations form the Navier Stokes equations, which are a set of partial differential equations (PDEs) that, in the majority of cases, do not have an analytical solution. However, PDEs can be approximated by a set of algebraic equations through the use of a discretisation method. There are numerous discretisation methods, the most common being the finite element method, the finite difference method and the finite volume method. In essence the approximated algebraic equations are applied to small sub-volumes within the flow; a process which is repeated numerous times in order to cover the entire volume of the flow.

Typically a CFD simulation follows a specific process that consists of several stages which are described below (de Souza, 2013). These stages are general stages for all CFD software and differ slightly for each individual software package.

The first stage is the approximation of the geometry. The geometry is developed in a three dimensional modelling program and needs to be as accurate as possible if it is to replicate the

performance of the actual machine. The geometry is then imported into the relevant CFD software package.

The second stage is the meshing of the geometry. In order to identify the discrete locations where the variables will be calculated, the geometry is divided up into a finite number of cells that make up the numerical grid. This grid is also known as a mesh. Before the mesh models can be selected, the flow characteristics (such as turbulence, compressible flow, shocks, multiphase flow and boundary layer flow) need to be known so that the correct meshing models can be chosen.

The next stage involves the selection of the physics models which represent the flow characteristics. The mathematical models and parameters for the flow phenomena are selected and the boundary conditions are defined for the domain.

The fourth stage deals with the prescription of initial conditions. Discretisation results in a large number of algebraic equations which are solved iteratively whereby a guess is made for the first set of variables. Error values (residuals) are computed from the discretised equations and the calculations are repeated numerous times until the residuals values have decreased sufficiently and the solution is judged to have converged. The initial conditions specify the value of the fluid variables throughout the flow domain at the starting point of a simulation.

The following stage is determining whether or not the solution has converged once the simulation has been run. When the sum of the residual values has become sufficiently small, the solution is considered converged. Another check is that the additional iterations produce negligible variations in other outputs being measured such as drag coefficient or pressure.

The penultimate stage is post processing whereby the results are represented in various formats at the discretion of the user. The results can be displayed in numerous ways such as graphs, velocity vectors and contours of constant values. The most significant part of post processing is understanding the results and what they mean.

The final stage of running a CFD simulation is solution verification and validation. Ideally, each solution should be compared to theoretical calculations or experimental data. In the current research a comparison with experimental data is not possible as the experimental rig remains incomplete, therefore, the comparison that is presented relies entirely on the results obtained from the 1D software (PUMPAL) as used by Smyth (2013). This development was beyond the control of the author. At the outset of this project the aim was to compare the CFD analysis with the experimental results and have the validation required to properly assess the meanline design of the full scale impeller.

Unfortunately, the complex alterations required for the volute casing have not yet been completed. The test rig also requires further modifications to the inlet piping in order to visually assess the cavitation.

2 Literature Review

A literature review was conducted to further understand the CFD process, the different techniques and models as well as the basics of cavitation; a flow phenomena which limits the negative pressures that can be tolerated in a liquid flow. The following chapter deals with the various categories of CFD relevant to this study. Naturally this involves the different types of mesh and turbulence models. The chapter also deals with several key papers which are similar to the work at hand. Cavitation is also discussed as well as the modelling parameters that predict its formation.

2.1 Mesh Models

As already stated, the governing equations are discretised before they are solved. The most common technique for discretisation in fluid simulations is the Finite Volume Method (FVM). The Finite Difference Method was more popular in the past but has a lack of flexibility when compared to the FVM. The Finite Element Method is also popular but more so in multiphysics simulations which are simulations where several physical phenomena are present and coupled systems of partial differential equations are required (De Beristain, 2012).

In the Finite Volume Method the domain is divided into a finite number of control volumes which correspond to the cells of a computational grid. Discrete versions of the integral form of the governing equations are then applied to each control volume in the domain. Star CCM+ uses the FVM to discretise these governing equations and obtain a set of linear algebraic equations which are solvable. This software formed the basis of the author's work.

The mesh of the computational domain is the discretised representation of the domain which is used by the solvers to provide a numerical solution. Star CCM+ has various mesh tools (surface and volume) and models available to accurately represent different geometries.

The *Polyhedral Mesher* provides a balanced solution for complex geometries. Polyhedral meshes are also easy to generate and require five times fewer cells than a tetrahedral mesh for a given starting surface. This makes the polyhedral mesh less computationally expensive. The polyhedral mesh is made up of arbitrary polyhedral cell shapes with 14 cell faces which are used to build the core mesh. Star CCM+ uses a special dualization scheme to generate the polyhedral mesh from a tetrahedral mesh which is built as part of the process (CD-Adapco, 2013). While various works made use of a tetrahedral mesh (Barrio, et al., 2010) (Dick, et al., 2001) (Montomoli, et al., 2010) (Bacharoudis, et al., 2008) or hexahedral mesh (Hellstroom, et al., 2012) (Spence & Amaral-Teixeira, 2009) a polyhedral mesh was used in the current work due to its lower computational cost.

Naturally, an important aspect of any fluid simulation that encounters turbulence is the boundary layer. To capture the boundary layer flow accurately the *Prism Layer Mesher* is used. This mesh model projects the core mesh back to the wall boundaries to create orthogonal prismatic cells next to the wall an example of which can be seen in figure 2.1.

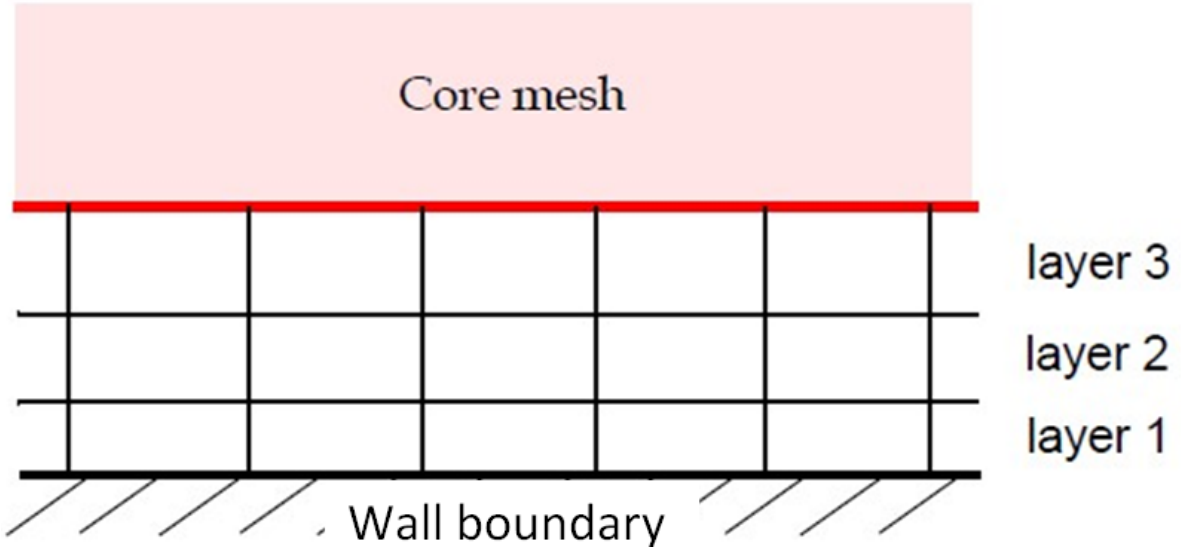

Figure 2.1: An example of 3 prism layers

The distribution of the prism layers is linked to the wall y+ value of the model. The y+ value is an indication of how accurately the mesh will capture the boundary layer. A low y+ (<1) means that the first cell centroid is within the viscous sublayer of the flow which will result in an accurate depiction of the boundary layer. A high y+ (30< y+ <100) means that the near wall cell centroid is in the log-law region of the boundary layer. The ideal y+ value for an impeller of this nature is debatable. Montomoli, et al., (2010) aimed for a y+ value of 1 in their study of the tip gap and fillet radius effects in turbomachinery while Lucius & Brenner, (2010) use only a Y+ value of 3.1. Westra, et al., (2010) also deemed a Y+ value of 3 to be sufficient while (Balasubramanian, et al., 2011) were content with a Y+ of 5.

The default method of setting prism layers is through the use of the stretching factor (seen in figure 2.2), the number of cells wanted and the overall prism layer thickness. The individual cell sizes are then based on these three variables. However, this can be altered and the stretch factor method can be changed to the wall thickness method. In the latter method, the thickness of the first cell is set as well as the number of cells and the overall prism layer thickness. Care must be taken when choosing this method though as the cells are not automatically sized to fit the overall prism layer thickness.

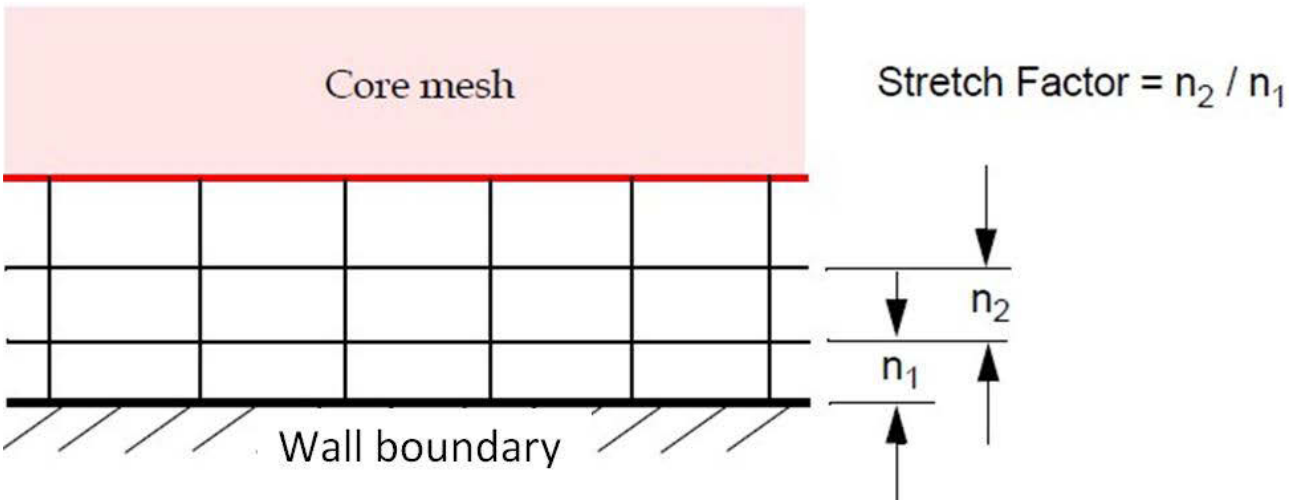

Figure 2.2: Stretch factor

As stated, the value of the wall Y+ can be set by defining the thickness of the prism layer closest to the wall. Equation 2.1 shows how the Y+ value can be calculated. In this equation, y is the distance from the wall to the first cell centroid. By selecting a Y+ value, the thickness of the first cell ($2y$) can be calculated. The thickness can then be prescribed in Star CCM+ after altering the method used to define the prism layers. The Y+ value is also dependent on the reference velocity, u^*, (which is a function of the wall shear stress, τ_w, and density, ρ,) as well as the kinematic viscosity, ν, of the fluid.

$$y^+ = \frac{u^* y}{\nu} \tag{2.1}$$

$$u^* = \sqrt{\frac{\tau_w}{\rho}} \tag{2.2}$$

2.2 Turbulence Modeling

One of the main obstacles in modeling Turbomachinery flows is the accurate modeling of the turbulence that is present in the flow field. Several methods described below are used to model the turbulence in fluid flow. Due to the popularity and convenience of the Reynolds Averaged Navier Stokes (RANS) techniques, the author has provided a more in-depth look at these models.

Literature suggests (Ferziger & Peric, 2002) the best way to approach turbulence modelling is to use a RANS technique as a starting point and if the results are inadequate, move on to a more in depth technique such as Large Eddy Simulations (LES) or Direct Numerical Simulations (DNS) (if the computing power is available). While DNS may be the most accurate way to simulate turbulence, the computational expense generally outweighs the accuracy. Montomoli, et al., (2010) used the K-Omega model to model the flow behaviour at the rotor tip to see how small geometric differences affect the flow behaviour. Ranade & Krishnan (2002) argued that the K-Epsilon model was inadequate in modelling the flow around an impeller. Despite this, Ranade & Krishnan (2002) stated that in most cases the mesh quality affected the accuracy of results more than the turbulence model being used and that if the turbulence model yielded reasonable results, it was not necessary to use a more complex model. Jafarzadeh, et al., (2010) performed a comparison between K-Epsilon, Re-Normalisation Group (RNG) K-Epsilon and Reynolds Stress Model (RSM), finding that the standard K-Epsilon model provided the least accurate results when compared to a particular experimental data set. However Barrio, et al., (2010) also used the standard K-Epsilon model but found the results accurate to within 4% of the experimental data. Bacharoudis, et al., (2008) used the K-Epsilon successfully, claiming that the numerical predictions predicted the total performance as well as the global characteristics of the laboratory pump reasonably well compared to experimental data. Shojaeefard, et al., (2012) used the Shear Stress Transport (SST) K-Omega model due to its high precision when modelling near-wall flow when looking at the performance of a centrifugal pump when certain geometric characteristics of the pump were altered. The numerical predictions of Shojaeefard, et al., (2012) were within 4% of the experimental results when using the SST K-Omega turbulence model. This information generally illustrates that different turbulence models are sensitive to the application at hand and are not universally better. The current work will use the SST-Menter K-Omega model, for reasons discussed in the information below. A brief description of the different turbulence models is presented below, with a more in depth look at the two most popular turbulence models, namely the K-Omega and K-Epsilon models.

2.2.1 Direct Numerical Simulation

The most accurate approach to turbulence simulation is Direct Numerical Simulation whereby the Navier-Stokes equations are solved without averaging or approximation (Ferziger & Peric, 2002). In Direct Numerical Simulation the Navier-Stokes equations are solved to determine the velocity field for one realization of the flow. DNS is especially computationally expensive because all length scales and timescales have to be resolved, in other words all the motions in the flow are resolved. The approach is also restricted to flows with a low Reynolds number as the computational cost increases at a rate proportional to the cube of the Reynolds number (Re^3) (Pope, 2000). Due to the comprehensive

nature of the results obtained using DNS it is too expensive to be used as a design tool and should rather be used as a research tool to create numerical flow visualization (Ferziger & Peric, 2002). Due to the high computational cost of DNS, it is not available in many commercial software packages and was not considered a viable option for this study. Some examples of where DNS has been used are:

- Understanding the mechanisms of turbulence production, energy transfer and dissipation in turbulent flows
- Simulation of the production of aerodynamic noise
- Understanding the effects of compressibility on turbulence
- Understanding the interaction between combustion and turbulence
- Controlling and reducing drag on a solid surface

2.2.2 Large Eddy Simulation

In LES, equations are solved for a 'filtered' flow field, where the larger turbulent motions are the most important (Pope, 2000). The large scale motions are more energetic than the smaller ones and are effective transporters of the conserved properties, due to their size and strength. The small scale motions are weaker and provide poor transport of the conserved properties. LES solves for the large scales of the turbulence and models the small scale motions. LES is three dimensional, time dependent and computationally expensive but not when compared to DNS. LES is the preferred method for flows through complex geometries and flows with a high Reynolds number (Ferziger & Peric, 2002).

2.2.3 Detached Eddy Simulation

Detached Eddy Simulation (DES) is a hybrid modeling approach that applies RANS techniques in some areas of the flow and LES methods in others areas. A DES model uses a base RANS model to solve the shear layers and then uses LES in the unsteady separated region of the flow (CD-ADAPCO, 2013). Majority of DES computations use Spalart-Allmaras as the base model. DES appears to use RANS as the near wall treatment and then LES away from the wall (Viswanathan, 2006).

While the DES approach seems promising for certain types of simulations, it must be noted that DES is not always the solution to turbulence modeling. The creation of a suitable grid is vital when using DES (CD-Adapco, 2013).

The recommended base RANS model is the Spalart-Allmaras detached eddy model. However, the SST (Menter) K-Omega model is also a viable option (CD-Adapco, 2013).

2.2.4 Reynolds Averaged Navier-Stokes

The oldest approach to turbulence modelling is Reynolds Averaged Navier-Stokes (RANS). In the RANS approach to turbulence, the Navier-Stokes equations for the instantaneous velocity and pressure fields are broken down into a mean and fluctuating component. Then, in the RANS approaches, all of the unsteadiness and fluctuations are averaged out. The RANS approach involves the solution of the Reynolds equations to determine the mean velocity field (Ferziger & Peric, 2002). The Navier Stokes equations consist of the equations for conservation of mass and momentum, which can be seen in equation 2.3 and 2.4 respectively (Wilcox, 1993)

$$\frac{\partial u_i}{\partial x_i} = 0 \tag{2.3}$$

$$\rho \frac{\partial u_i}{\partial t} + \rho u_j \frac{\partial u_i}{\partial x_j} = -\frac{\partial P}{\partial x_i} + \frac{\partial t_{ji}}{\partial x_j} \tag{2.4}$$

The vectors u_i and x_i represent velocity and position while t is time, p is pressure, ρ is density and t_{ji} is the viscous stress tensor which is defined by Wilcox as

$$t_{ji} = 2\mu s_{ij} \tag{2.5}$$

Where μ is the molecular viscosity and s_{ij} is the strain rate tensor,

$$s_{ij} = \frac{1}{2}\left(\frac{\partial u_i}{\partial x_j} + \frac{\partial u_j}{\partial x_i}\right) \tag{2.6}$$

Combining the above equations yields the Navier Stokes equation in conservation form.

$$\rho \frac{\partial u_i}{\partial t} + \rho \frac{\partial}{\partial x_j}(u_j u_i) = -\frac{\partial P}{\partial x_i} + \frac{\partial}{\partial x_j}(2\mu s_{ji}) \tag{2.7}$$

Time averaging the conservation of mass and the above Navier Stokes equation results in the Reynolds Averaged equations of motion in conservation form as defined by Wilcox (1993),

$$\frac{\partial U_i}{\partial x_i} = 0 \tag{2.8}$$

$$\rho \frac{\partial U_i}{\partial t} + \rho U_j \frac{\partial U_i}{\partial x_j} = -\frac{\partial P}{\partial x_i} + \frac{\partial}{\partial x_j}\left(2\mu S_{ji} - \rho\overline{u'_j u'_i}\right) \tag{2.9}$$

Aside from the replacement of the instantaneous variables by mean values, the time-averaged equations are identical to the instantaneous equations with the exception of what is termed the Reynolds Stress Tensor denoted (τ_{ij}) (Wilcox, 1993):

$$\left(\tau_{ij}\right) = -\rho\overline{u'_i u'_j} \tag{2.10}$$

Due to the presence of the extra term above, the conservation equations contain more variables than there are equations. So for three dimensional flows there are four mean-flow properties that are unknown (three velocity components and pressure) as well as six Reynolds stress components. This yields ten unknowns and only four equations (the continuity equation and three components of the Navier Stokes equation) (Davidson, 2011) and therefore the system is not closed. To close the conservation equations, approximations have to be made. These approximations are known as the turbulence models that make use of the RANS approach (Ferziger & Peric, 2002). Two major classes of RANS modelling exist, namely the eddy viscosity models (turbulent viscosity models) and the Reynolds stress transport model. Other categories exist such as algebraic models and one equation models which are described in detail by Wilcox (1993) but are not applicable to this work.

Eddy viscosity models are based on a turbulent viscosity which is computed using an algebraic model. The most common approximation which forms the basis of all eddy viscosity models is the Boussinesq approximation (Davidson, 2011). This assumption relates the Reynolds stress tensor to the

velocity gradients through the turbulent viscosity. The resulting stress tensor can be seen in equation 2.11 below:

$$\tau_{ij} = 2\mu_T S_{ij} - \frac{2}{3}\rho k \delta_{ij} \tag{2.11}$$

The most significant area of focus in this work is the two equation class of models. These models are deemed complete because two transport equations are derived which define two scalars (such as turbulent kinetic energy, energy dissipation or the specific dissipation rate). The Reynolds stress tensor is then computed using an approximation which relates the tensor to the velocity gradients and eddy viscosity (Davidson, 2011). The assumption that is made is dependent on the model being used, as discussed below.

In eddy viscosity models an expression for the turbulent viscosity is wanted, the dimensions of which are [m^2/s]. This dimension can be achieved by multiplying a turbulent velocity scale by a turbulent length scale such as

$$\nu_t = U\ell \tag{2.12}$$

Within the eddy viscosity models are two of the most common RANS models, the K-Epsilon and K-Omega models. The K-Epsilon and K-Omega models are both two-equation turbulence models, which means two turbulent quantities are solved in the model equations. From the two quantities in each model, a length scale, a timescale and so on can be formed (Pope, 2000). The K-Epsilon model is the most widely used turbulence model where the transport equations for the turbulent kinetic energy k and the energy dissipation (ε) are solved (Davidson, 2011). These transport equations are used to determine the velocity scale and the length scale of the turbulence (Ferziger & Peric, 2002). The length scale is defined by Davidson (2011):

$$\ell = \frac{k^{\frac{3}{2}}}{\epsilon} \tag{2.13}$$

Wilcox defines the turbulent viscosity for the K-Epsilon model as per equation (2.14).

$$\mu_T = \frac{\rho C_\mu k^2}{\varepsilon} \tag{2.14}$$

The profile of the turbulent kinetic energy has greater amplitude near the wall than in the mean velocity profile. These peaks (regions of greater amplitude of turbulent kinetic energy) make it difficult to accurately capture the flow data near the wall. To overcome this, a finer mesh needs to be used near the wall. At high Reynolds numbers an insufficient mesh becomes an even greater problem as the viscous sub layer is extremely thin. This is where separate wall functions are introduced to overcome the issue (Ferziger & Peric, 2002). The K-EPSILON model performs reasonably well for two-dimensional thin shear flows where the streamline curvature and mean pressure gradients are both low (De Beristain, 2012). There are several variations of the K-Epsilon model available in Star CCM+ with the most relevant model being the Realisable K-Epsilon Model.

The second most widely used turbulence model is the K-Omega model. Here, the standard turbulent kinetic energy (k) equation is used but ω is introduced as a length determining equation. In this model ω is defined as the specific dissipation rate or "the rate of dissipation of energy in unit volume and time" (Wilcox). This property derives its name from its definition$\left(\omega \propto \frac{\varepsilon}{k}\right)$. The K-Omega model has the following definitions for turbulent viscosity, energy dissipation and length scale (Wilcox, 1993).

$$\mu_T = \frac{\rho k}{\omega} \tag{2.15}$$

$$\varepsilon = \beta^* \omega k \tag{2.16}$$

$$\ell = k^{1/2}\omega \tag{2.17}$$

The K-Omega model is superior to the K-Epsilon model in the way that it handles the viscous near-wall regions and the effects of streamwise pressure gradients in boundary layer flow (Pope, 2000). The K-Omega model provides a more accurate prediction of the flow than the K-Epsilon model in stronger pressure gradients (De Beristain, 2012). One disadvantage of the K-Omega model is that, in its original form, boundary layer computations are very sensitive to the values of Omega in the free stream. Various versions have been modified to overcome this sensitivity issue. There are three

versions of the K-Omega model in star CCM+, namely, the standard K-Omega model, the SST K-Omega model and the SST K-Omega detached eddy model (CD-Adapco, 2013).

The SST K-OMEGA was proposed by Menter who recognized that the Epsilon transport equation could be transformed, using variable substitution, into a transport equation for Omega. The transformed equation looks similar to the equation in the K-OMEGA model but it has an added cross-diffusion term. If this cross-diffusion term is included in the K-Omega model, the results are identical to that of the K-Epsilon model. Menter then introduced a blending function that includes the cross-diffusion term far from the walls but not near the wall. The result is that the SST K-OMEGA approach uses the K-Epsilon model far from the walls and the K-Omega model near the wall which provides the advantages of both the K-Omega and K-Epsilon models (CD-Adapco, 2013).

Recalling that the RANS approach also has a second category of turbulence models. These models solve for the Reynolds stress tensor terms rather than the turbulent viscosity term in the averaged Navier Stokes equations. In this category there are the Reynolds Stress Transport (RST) models. The RST models are the most complex turbulence models in Star CCM+. They account for effects such as streamline curvature, rapid changes in strain rate and anisotropy due to swirling motions by solving transport equations for all components of the specific Reynolds Stress tensor. The complexity of the RST models is such that seven additional equations need to be solved in three dimensions as opposed to the two equations of a K-Epsilon model. This makes the RST models computationally expensive and not a very likely option. There are three different RST models in Star CCM+, namely, Linear Pressure Strain, Quadratic Pressure Strain and Linear Pressure Strain Two-Layer (CD-Adapco, 2013).

2.3 Previous Research

Several other studies were examined during the literature review. A few of these are presented below. These works influenced parameters and characteristics of the numerical model designed for the scaled and full size turbopump impellers.

Hellstroom, et al., (2012) modelled the unsteady flow in a radial compressor using the LES technique. The reasoning behind the use of the LES technique was that the flow in the compressor has unsteady large scale structures and separation zones. In the study carried out by Hellstrom et al, no explicit sub-grid scale model was used. Instead only numerical dissipation accounts for the sub-grid scale dissipation at the smallest scales (Hellstroom, et al., 2012).

Jafarzadeh, et al., (2010) performed a general three dimensional simulation of turbulent flow through a centrifugal pump to predict the velocity and pressure fields. The results were used to form the characteristic curve of the pump which were compared to experimental data and proved to be within an acceptable range. Once the model had been validated the study went on to investigate the effect the number of blades on the impeller had on the efficiency of the pump. Jafarzadeh, et al., (2010) uniquely modelled the impeller as well as the volute, taking into account the interactions between them. Jafarzadeh, et al., (2010) used three different regions in their model, namely, the inlet, the rotating region and the outlet. Each region was discretised independently. The inlet and rotating regions made use of structured grids while the outlet region had a mixture of a structured and unstructured mesh leading to a cell count of 5.8 million cells. Jafarzadeh, et al., (2010) also tested three different turbulence models to find the most suitable one. The models tested were standard K-Epsilon, RNG K-Epsilon and RSM. During the validation of the CFD model against the experimental data, RNG K-Epsilon and RSM showed a greater accuracy than the standard K-Epsilon model. Jafarzadeh, et al., (2010) selected RNG K-Epsilon as the most suitable as it has a lower computational time when compared to RSM.

Barrio, et al., (2010) present a numerical investigation on the performance of a commercial centrifugal pump operating in direct and reverse mode. The solver used by Barrio, et al., (2010) was FLUENT. The model was validated with experimental data of head versus pressure rise. Once validation was complete the model was used to investigate global flow as well as the radial thrust on the impeller. The model made use of an unstructured tetrahedral mesh which discretised the impeller as well as the volute and resulted in a cell count of 800 000 cells. Prismatic cells were used in the inlet and outlet ducts. Barrio et al., (2010) used the standard K-Epsilon model plus the standard wall functions to simulate turbulence. Second order discretisation was used for the convection and diffusion terms. The model was first simulated using a frozen rotor interface and once convergence had been achieved the velocity and pressure fields obtained from the frozen rotor simulation were used as initial conditions for the unsteady calculations. To correlate between the numerical and experimental results, the flow versus head characteristics were compared. The numerical predictions showed a maximum error of less than 4% when compared to the experimental results which was deemed acceptable.

Bacharoudis, et al., (2008) were concerned with the influence of the outlet blade angle on the performance of a centrifugal pump. In the study three shrouded impellers were simulated, each with a different outlet blade angle. For accurate comparison the design and off-design performance characteristic curves, the local and global variables of the flow field and the resulting non-uniform circumferential pressure field were numerically predicted for all three impellers. The turbulence of the flow was modelled with the standard K-Epsilon model (which the study rated as the most used model) stating that this model combines simplicity, robustness and reasonable accuracy and that it shows

satisfactory results for a wide range of industrial flows. The domain was split into three sub-domains. The first zone represents the inlet pipe and the third zone represents the outlet portion where the flow is fully developed with a less possible reacting outlet boundary condition. These two zones were meshed using unstructured wedges. The second zone or sub-domain, consists of the impeller of the pump and is meshed using an unstructured mesh that consists of tetrahedral cells. The mesh is refined in the near tongue region as well as close to the leading and trailing edges of the blades. Around the blades, structured hexahedral cells are used. Bacharoudis et al., conclude that the numerical predictions seem to predict, reasonably, the total performance of the laboratory pump.

Dick, et al., (2001) analyze two test pumps with low and medium specific speeds. For both of the pumps the head as a function of flow rate for a constant rotational speed is known from experimental data. One of the aims of the research was to determine how far the Multiple Reference Frame (frozen rotor technique) can take into account the circumferential pressure variation caused by the volute for flows different from the operating point. For the frozen rotor technique the impellers were modelled in two different positions; in the first position the tongue of the volute was in between blades while in the second position an impeller blade aligned with the tongue. This links to the work of Zhu & Chen, (2012) who stated that the steady simulation (frozen rotor technique) is strongly dependent on the relative location of the impeller and volute. The mesh characteristics used in this study are fairly standard. For the first pump the impeller is meshed with hexahedra and wedge cells while the inlet is meshed with prisms and the volute has an unstructured tetrahedral mesh. The resulting cell count is 300 000 cells for the first pump. The second pump has a cell count of 500 000 cells and differs from the first pump in the rotating region where the impeller has an unstructured tetrahedral mesh. Like many other works this paper uses a second order upwind scheme for convective terms as well as a RANS turbulence model. More specifically, the Realizable K-Epsilon model was used with non-equilibrium wall functions. Dick, et al., (2001) determined the turbulent intensity from a formula for fully developed pipe flow. This is worth noting as a tool to be used in the current work.

Montomoli, et al., (2010) studied the effect of varying small geometries such as the gaps and fillets. An initial analysis was carried out considering a pre-described value for the fillet radius to underline the high impact of geometrical variations on the flow field. Then, five different fillet radii and three different tip gaps were used to provide an understanding of geometrical uncertainties. Montomoli et al., (2010) use the traditional two equation K-Omega model stating that it “demonstrates higher performances allowing accurate computations and good stability properties simultaneously”. The work goes on to explain that the revised low Reynolds formulation allows a realistic evaluation of the turbulent boundary layer growth with only a small numerical cost. The numerical model is carried out as a steady state simulation using a mixing plane approach. This work uses a computational mesh consisting of 6.2 million cells. This mesh is made up of prismatic layers near the wall and

tetrahedrons inside the vane. The wall Y+ value that was aimed for was 1, with a total number of prismatic layers being 20. Montomoli et al., (2010) found this sufficient enough to accurately capture the boundary layer flow. The boundary conditions consisted of a stagnation inlet where the stagnation temperature and pressure were set. At the outlet, the mean static pressure was set while the shape of the radial distribution was extrapolated from the field.

Shojaeefard, et al., (2012) looked at the performance of a centrifugal pump when certain geometric characteristics of the pump were altered. The alterations include changing the outlet angle and passage width of the impeller. As with the majority of the studies the domain consists of three regions, the volute, impeller and outlet pipe. The mesh configuration consists of a structured mesh near the wall to allow greater accuracy in the boundary layer region. At regions away from the wall, an unstructured mesh was used to accurately discretise the complex geometry. This unstructured mesh configuration consists of six sided, pyramid and wedge shaped elements. As already stated, the analysis of flow in centrifugal pumps can be done in a steady or transient state. Shojaeefard et al. state that if the volute has fixed blades the flow is unsteady in nature and should be modelled as such. This is due to the interaction of the impeller and diffuser blades at the impeller outlet. However, if the volute does not have fixed blades the system can be modelled as 'steady' by defining a rotating reference frame which is applied to the impeller region. Shojaeefard, et al., (2012) make use of a rotating reference frame (applied to the impeller) while the volute remains in the fixed reference frame. To capture the turbulent effects on the flow field, the study used the K-Omega SST turbulence model because of the models high precision when modelling near wall flow. The boundary conditions used for this particular research consist of a pressure inlet and a mass flow outlet. The turbulence intensity at the inlet was set to 5%, although the authors admit it to be an empirical value. The no-slip condition was applied to the solid boundaries and a surface roughness of 100 μm was set. The study used both water and oil for the numerical simulations. Shojaeefard, et al., (2012) also did a mesh independency study and found the optimum number of mesh elements. The total pressure rise inside the pump and the mean differences of circumferential velocity values were used to evaluate the mesh characteristics of the model. The optimum mesh had been reached when the least number of dependent mesh elements were used and the pressure change was negligible. The authors compared the numerical and experimental results and found that the average difference percentage in each case was approximately 4% (the highest was 4.06% and the lowest 3.35%) which Shojaeefard, et al., (2012) deemed to be satisfactory.

The above information shows various trends common with other research. These trends include the definition of three separate regions usually the inlet, the volute and the impeller. The review also showed that an unstructured mesh is used away from the walls while a more structured scheme is opted for close to the walls. Another commonality is to start with a steady simulation using a rotating

reference frame and then if needed, moving onto an unsteady simulation. While the choice of turbulence models may vary for each study, all the results show a good degree of accuracy.

2.4 Physics Models

Selecting the appropriate physics models within the CFD program is vital to obtain an accurate solution. There are various categories of physics models that need to be known before the simulation to allow for a true representation of the physical problem at hand. Some of these categories include space, time and motion, materials, flow and energy, species, turbulence and transition, and multiphase flow (CD-Adapco, 2013). While all of these categories are significant some are easier to understand than others. Several of the physics models are discussed below.

Within the 'space category' one simply needs to ascertain whether the geometry is axisymmetric, two dimensional or three dimensional. Due to the complexity of the geometry in the current work a full three dimensional model needed to be used.

The time models provide solvers that control the iteration as well as the unsteady time stepping. There are three time models that can be selected, namely steady, implicit unsteady and explicit unsteady. The steady model is used for steady state calculations and when this model is used, the concept of a time step is meaningless. The steady time model will be used for the rotating reference frame simulations. The implicit unsteady model and the explicit unsteady model both deal with transient analyses. The implicit model is capable of running in conjunction with the segregated flow solver as well as the coupled flow solver whereas the explicit model is only available with the coupled flow solver and is used in inviscid, laminar flows. For the rotating motion simulations the implicit unsteady model will be used in the current work as the flow is neither inviscid nor laminar.

There are a wide range of motion models available in Star CCM+. However, only two will be made use of in this study. The first model is the rotating reference frame model also known as the frozen rotor method. A rotating reference frame converts an unsteady motion problem into a steady state problem by imposing a moving frame of reference on a static mesh. Many studies have used this model as a starting point for their solution. Zhu & Chen, (2012) state that a steady state simulation using a rotating reference frame is strongly dependent on the relative location of the impeller and volute. They go on to explain that this is the reason an unsteady simulation is necessary when modelling a volute. In order to provide an unsteady simulation, rigid body motion is needed which involves the actual displacement of mesh vertices in real time. Rigid body motion also has to be used in conjunction with a transient analysis which requires an unsteady time solver.

2.5 Cavitation

Cavitation is a common occurrence in the majority of pumping applications and causes material damage, a decrease in pump performance as well as unwanted vibrations and noise. Cavitation occurs as a result of a local pressure loss in the liquid which causes the liquid to vaporise, in the case of a centrifugal pump, commonly at the inlet to the pump impeller. The vapour bubbles then collapse when the local static pressure increases above the saturation pressure resulting in intense pressure waves that impact and cause material loss on the impeller. The process of cavitation can be described in three stages (Balasubramanian, et al., 2011):

i. Cavitation inception- the formation of vapour bubbles near the leading edge
ii. Bubble growth and transport of vapour bubbles downstream of the leading edge
iii. Cavitation destruction and condensation- collapse of vapour bubbles when the surrounding local pressure increases above the saturation pressure.

A number of design factors can influence the onset of cavitation in a pump such as the inlet casing design, impeller geometry (especially at the eye) and discharge volute design. The discharge volute has little influence on the cavitation behaviour near best efficiency point (BEP) operation but gets more important as the pump performance is drawn away from BEP due to the recirculation of flow in the volute. The most influential factor is the impeller geometry such as the inlet and hub diameters, blade inlet angles, blade number, blade thickness and surface roughness (Balasubramanian, et al., 2011).

Cavitation can occur in various machines dealing with liquid flow where the pressure drops below the vapour pressure of the fluid. When the local static pressure falls below the vapour pressure of the fluid the liquid can locally flash to vapour. This results in the formation of a vapour cavity (bubble) which significantly alters the flow pattern. The bubble changes the shape of the flow passage which effectively alters the local pressure field. The changing local pressure field can result in the flow becoming unsteady as the bubble size is dependent on the pressure. The unsteady flow can cause the entire flow to oscillate and the machine to vibrate.

As cavitation starts, it diminishes the performance of a pump drastically. In addition to reduced pump performance, erosion damage and surface pitting are a high probability due to the vapour bubbles imploding on the impeller surface. Naturally cavitation must be avoided for optimum performance as well as to prolong machine life.

In a pump cavitation tends to begin where the flow is accelerated into the impeller and the chances of cavitation are greatly increased when local flow speeds are increased. This occurs whenever flow rate or machine operating speed are increased.

Cavitation can be avoided if the pressure everywhere is kept above the vapour pressure of the operating fluid. To do this the pipe inlet pressure should be well above the vapour pressure as the inlet piping will have losses.

The net positive suction head (NPSH) is defined as the difference between the absolute stagnation pressure at pump suction and the liquid vapour pressure. In other words, the NPSH is a measure of the difference between the maximum possible pressure in the given flow and the pressure at which cavitation will occur. The larger the NPSH, the smaller the chance of cavitation will be. Naturally the NPSH available (NPSHA) needs to be larger than the NPSH required (NPSHR) if cavitation is to be avoided. Inlet piping losses increase as the flow rate increases thus for any system the NPSHA decreases with an increasing flow rate. There are various ways to reduce the inlet pressure losses such as increasing the diameter of the piping (Fox, et al., 2010).

Cavitation is categorised by a dimensionless number known as the cavitation number (equation 2.18). The cavitation number is dependent on the vapour pressure (P_{sat}), the liquid density (ρ_l), the flow pressure (P) as well as the flow velocity (U). As the cavitation number decreases, the probability of cavitation increases (Asnaghi, et al., 2010).

$$\sigma = \frac{P - P_{sat}}{\frac{1}{2}\rho_l U^2} \tag{2.18}$$

The cavitation number is an important parameter especially when dealing with different operating conditions. A constant cavitation number found despite different operating conditions implies a similar degree of cavitation susceptibility in a given configuration. This means that for two pumps with the same cavitation number, the level of cavitation should be the same relative to the pump size. In the scaling process done by Smyth (2013) the cavitation number was kept relatively similar (0.087 in the full pump and 0.091 in the scaled down case) which means that the degree of cavitation in the three dimensional models of the two pumps should be similar.

2.5.1 Cavitation Patterns

There are several different patterns of cavitation which are defined by the growth of vapour. The interfaces between the liquid and vapour phases hold different shapes which are vital in identifying the type of cavitation present. Some of the cavitation patterns include travelling bubble cavitation, attached cavities, vortex cavitation and shear cavitation which are described below.

2.5.1.1 Travelling bubble cavitation

Figure 2.3 shows a typical visualization of travelling bubble cavitation on a foil section in a hydrodynamic tunnel. In travelling bubble cavitation, separate bubbles are present which grow on the suction side of the foil. These bubbles are to some extent, similar to the bubbles produced by a boiling liquid on a heated wall.

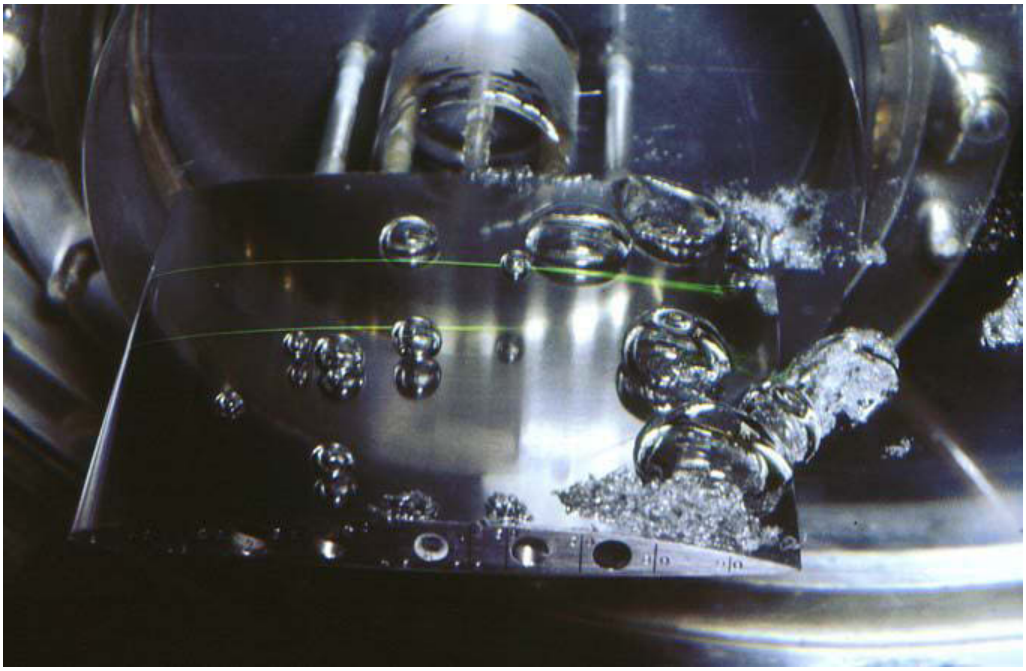

Figure 2.3: Travelling bubble cavitation (Franc, 2006)

This type of cavitating flow shows the weak point in the liquid from which the bubbles are able to form. These weak points are known as cavitation nuclei and are typically microbubbles in the flow. These microscopic bubbles become macrobubbles as the flow passes through a region where the pressure drops below the saturation pressure of the liquid. The bubbles are often not simply spherical in shape as the presence of a wall or nearby neighbouring bubbles cause deviations from the spherical shape. This configuration has its name as the bubbles are conveyed by the flow over the wall. The bubbles grow in the low pressure region and then collapse in the region of pressure recovery downstream.

2.5.1.2 Attached cavitation

In attached cavitation the vapour cavity interface is partly attached to a solid surface in a quasi permanent way. Leading edge cavitation (figure 2.4) occurs at low pressure zones of the blade surface and is also known as sheet cavitation when it closely resembles a thin film-like layer on the solid surface. Leading edge cavitation can be partial or appear as super cavitation when the cavity grows sufficiently to envelope the whole body. Leading edge cavitation often occurs in hydraulic machinery that operates under off-design conditions (Franc, 2006) . The cavity interface can either be smooth, glossy and transparent or frothy (similar to that of a highly turbulent boiling surface). In figure 2.4 the detachment is smooth which shows a locally laminar flow which becomes more turbulent downstream.

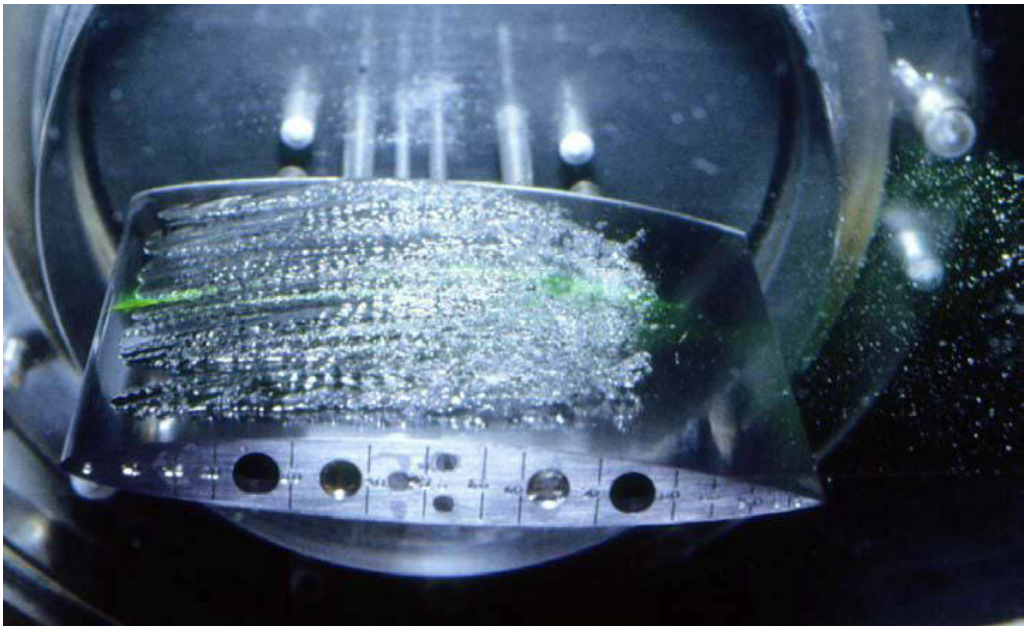

Figure 2.4: Leading edge cavitation (Franc, 2006)

2.5.1.3 Vortex Cavitation

In the configuration of a 3D hydrofoil the pressure difference between the pressure side and suction side of the hydrofoil produces a secondary flow which goes around the tip and generates a vortex. This vortex source is at the tip of the foil. The centre of the vortex has the lowest pressure as the centrifugal forces create a higher pressure away from the core. This low pressure region at the vortex core causes the formation of cavitation as seen in figure 2.5. A common example of vortex cavitation is the cavitation that often occurs on marine propellers where a vortex is produced at the tip of each of the blades as seen in figure 2.6. Tip vortex cavitation is usually the first type of cavitation experienced on marine propellers.

Figure 2.5: Vortex cavitation generated by a three dimensional hydrofoil (Franc, 2006)

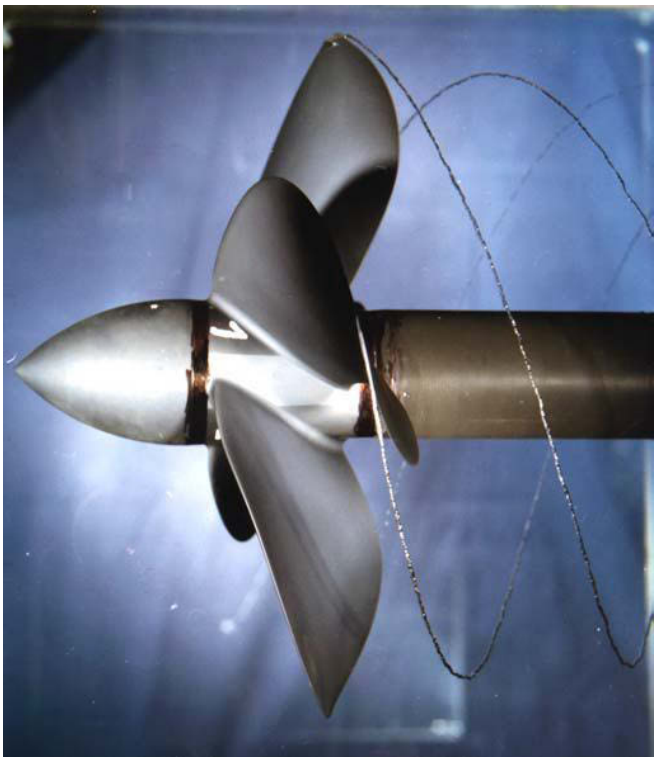

Figure 2.6: Vortex cavitation generated by a marine propeller (Franc, 2006)

2.5.1.4 Cavitation Nuclei

As expressed earlier, there are points in a liquid flow which act as nuclei for the growth of the vapour phase. The most common model of a nucleus is that of a microbubble (Franc, 2006) and a summary of Franc (2006) describes this model below.

Unless a liquid is treated and deaerated, it contains dissolved gas. An example of this is the presence of Nitrogen and Oxygen in tap water. The microbubbles that form when a liquid is subjected to a low pressure contain non condensable gas (such as nitrogen and oxygen) as well as vapour.

Thermodynamic equilibrium is assumed at the interface of the microbubble. This equilibrium requires that equation (2.19) is satisfied, where P_g represents the partial pressure of the gas in the bubble and P_v is the partial pressure of the vapour in the bubble which is assumed to be equal to the vapour pressure of the liquid (Franc, 2006). P_∞ is the pressure of the liquid flow while S represents the surface tension on the bubble and R is the radius of the microbubble.

$$P_g + P_v = P_\infty + \frac{2S}{R} \tag{2.19}$$

The equation means that the total pressure inside the bubble is actually greater than the pressure of the flow (P_∞) because the surface tension term ($\frac{2S}{R}$) is needed to make up the difference.

When looking at the bubble formation there is a link between the critical radius and the pressure. A nucleus is characterised by the mass of non-condensable gas. This mass is assumed constant irrespective of the evolution of the nucleus because the assumption means the transfer of mass through the interface of the microbubble (via diffusion) can be ignored.

The growth of the nucleus is ideally isothermal which means, according to Franc (2006), that the gas pressure is inversely proportional to the bubble volume as can be seen in Equation 2.20 (the perfect gas law).

$$P_g = \frac{K}{R^3} \tag{2.20}$$

Franc states that the constant K is characteristic of the considered nucleus. Equation (2.20) can be rewritten by substituting equation (2.19) to produce equation (2.21).

$$\frac{K}{R^3} + P_v = P_\infty + \frac{2S}{R} \tag{2.21}$$

For any nucleus with the characteristic K, equation (2.21) allows for the computation of the equilibrium radius (R) for any pressure of the flow. This can be seen from the equilibrium curve (figure 2.7) which is generated from equation 2.21. The equilibrium point has a minimum point defined by a critical radius and a critical pressure which can be denoted as:

$$R_c = \sqrt{\frac{3K}{2S}}$$
$$P_c = P_v - \frac{4S}{3R_c} \tag{2.22}$$

This point acts as a stability point. To the left of this point the curve is stable however, to the right of the critical point is the unstable region. A summary of Franc's (2006) work follows.

Prior to reaching the critical point (R_c,P_c) the curve is in the stable region. A nucleus that is represented by point 1 on the curve is stable. If the pressure of the liquid was decreased slightly it is expected that the nucleus will grow. The radius will increase slightly and the nucleus will reach equilibrium again at point 1'.

However, a nucleus at point 3 will grow indefinitely after any decrease in pressure. This indefinite growth occurs because the equilibrium curve is not crossed again which means that equilibrium is not reached. The indefinite growth of this nucleus will result in the formation of a cavitation bubble. This shows that the dotted part of the curve is unstable.

If a nucleus at point 2 on the curve experiences a pressure decrease that takes the pressure below that of the critical pressure (p_c), the nucleus will grow indefinitely without reaching a new equilibrium. As with the previous case of point 3, the nucleus here will form a cavitation bubble. The P_c value can therefore be seen as a critical value, below which the nucleus will grow indefinitely, become destabilised and form a bubble.

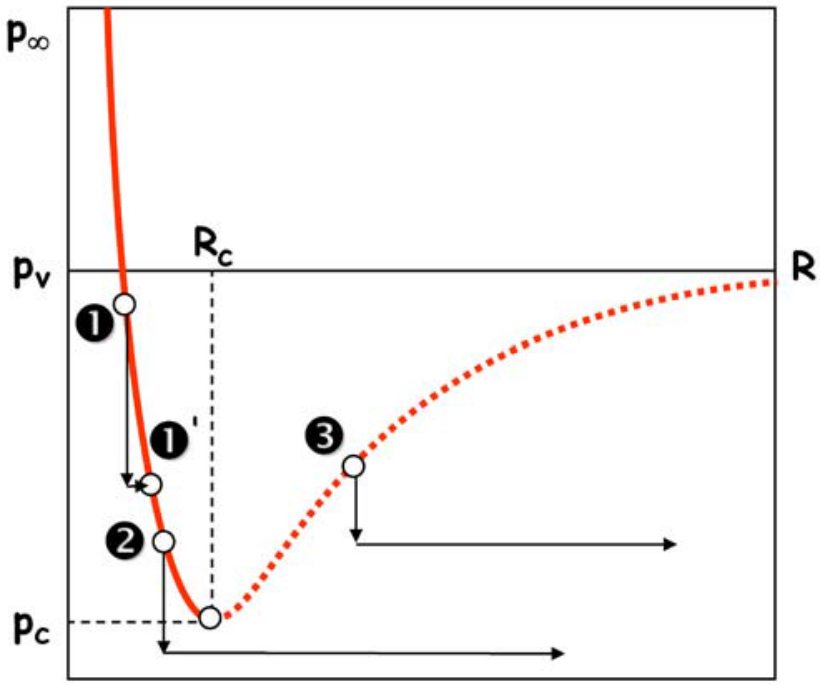

Figure 2.7: Equilibrium radius of a nucleus as a function of pressure (Franc, 2006)

The above model shows that the critical pressure for the onset of cavitation is slightly lower than the vapour pressure. The model also shows that the smaller the nucleus radius is, the greater the deviation from the vapour pressure. This delay in the start of cavitation is due to the surface tension (Franc, 2006). Despite this, the critical pressure is often taken as the vapour pressure of the liquid. Franc explains that in a liquid where a large variety of nuclei exist, it is common practice for the pressure at which cavitation will form to be taken as the critical pressure of the largest nuclei. It can be seen from the discussion above (and equation 2.22) that the larger the nuclei is, the closer the critical pressure is to the vapour pressure. While it is generally acceptable to take the vapour pressure as the starting point of cavitation, this model shows that deviations can be expected depending on the liquid quality in terms of nuclei content.

2.6 Cavitation Modelling

To model cavitation in Star CCM+ one needs to recognise that cavitation is classified as a multiphase flow as it consists of both liquid and vapour simultaneously. In multiphase flow, distinct interfaces exist between the different phases which mix on a macroscopic scale. There are two distinct categories of multiphase flow, dispersed flow and stratified flow. Cavitation falls into the dispersed flow category. For these two flow types, Star CCM+ offers five different models (CD-Adapco, 2013) to best suit the application at hand, namely:

- The Multiphase Segregated Flow model: also known as the Eulerian Multiphase model, it solves conservation equations (for mass, momentum and energy) for each phase. Phase interaction models are present to allow the influence of one phase on another to be modelled.
- The Lagrangian Multiphase model: solves the equations of motion for parcels of the dispersed phase as they travel through the system. It is best suited to systems that consist mainly of a single continuous phase which has a relatively small secondary phase volume (droplets/bubbles). It also deals well with modelling the interaction of the discrete phase with physical boundaries.
- The Discrete Element model (DEM): is an expansion of the Lagrangian model. The main difference being that here individual particles are modelled instead of representative parcels, as in the Lagrangian model.
- The Fluid Film model: using boundary layer approximations as well as velocity and temperature profiles of a fluid film, this model predicts the dynamic characteristics of wall films. Film motion is predicted using thin shells located on the surface of solid walls on which the film is formed.
- The volume of fluid (VOF) model: is used in flows that have two (or more) immiscible fluid phases, where each phase contributes a significant structure within the flow. This model captures the motion of the interface between phases.

The VOF model is best suited for modelling cavitation due to the interface between phases being captured. The VOF model has two methods of predicting mass transfer from one phase to another. The first method is known as interface resolution. This method is numerically expensive as it involves the capturing of fine details such as microbubbles with multiple cells. The evaporation/condensation model uses interface resolution. The cavitation model however, uses a homogenous approach. The homogenous approach makes assumptions regarding the interfaces between phases on a subcell level. This makes it a more efficient method but it is limited in terms of the physical phenomena it can capture. Despite this, it has been proven for use in industrial design studies. Both cavitation and gas dissolution make use of the same homogenous seed based approach in Star CCM+.

The seed based approach consists of two interacting phases, liquid (l) and gas (g), with positive mass transfer from liquid to gas. The volume fraction of gas is described as:

$$\alpha_g = \frac{V_g}{V} = \frac{V_g}{V_g + V_l} \tag{2.23}$$

The gas phase in each control volume is assumed to be in the form of bubbles which each have the same radius (R). The number of bubbles per unit volume is denoted as n_0. This yields the following relationship between the phases:

$$V_g = n_0 V_l \frac{4}{3}\pi R^3 \tag{2.24}$$

Making the volume fraction of gas:

$$\alpha_g = \frac{n_0 \frac{4}{3}\pi R^3}{1 + n_0 \frac{4}{3}\pi R^3} \tag{2.25}$$

This allows the gas bubble radius to be prescribed as:

$$R^3 = \frac{\alpha_g}{n_0 \frac{4}{3}\pi\left(1 - \alpha_g\right)} \tag{2.26}$$

The mass transfer rate ($kg/m^3 s$) can then be described by the following equation:

$$\dot{m} = n_0 \alpha_l 4\pi \rho_g R^2 \frac{DR}{Dt} \tag{2.27}$$

The liquid therefore vapourises with a volume rate of:

$$\dot{V}_l = -\frac{\dot{m}}{\rho_l} \tag{2.28}$$

The unknown factor which gives the increase in bubble radius as the liquid loses volume is $\frac{DR}{Dt}$. This factor is modelled using the Rayleigh Plesset (RP) equation which describes the development of the bubble radius when the bubble lies in an infinite domain. The equation represents the equilibrium of stress at the interface of the bubble. To obtain the RP equation, the mass and momentum conservation equations in both fluid and gas are considered and the stress equilibrium is then prescribed (Liuzzi,

2012). The RP equation takes into account the inertia, viscous and surface tension effects and can be seen in equation 2.29 where μ_l is the liquid viscosity and σ is the surface tension.

$$R\frac{d^2R}{dt^2}+\frac{3}{2}\left(\frac{dR}{dt}\right)^2=\frac{p_{sat}-p_\infty}{\rho_l}-\frac{2\sigma}{\rho_l R}-4\frac{\mu_l}{\rho_l R}\frac{dR}{dt} \tag{2.29}$$

Various works have made use of the cavitation models mentioned above. The work of Balasubramanian, et al., (2011) as well as Zhu & Chen, (2012) are discussed below.

Balasubramanian, et al., (2011) investigated the effect of different blade leading edge profiles on cavitation and suction performance through the use of CFD as well as an experimental rig. Blunt, circular, elliptic and parabola leading edge profiles were studied as well as the effect of these profiles on the cavitation inception, bubble growth and cavity length. To model the cavitation a two phase homogenous mixture model was employed with the Rayleigh Plesset Equation controlling the bubble growth. Balasubramanian, et al., (2011) explains that this model solved for two phases, the vapour phase (α_V) and the liquid phase (α_L) at each cell volume. Naturally the sum of both phases is equal to 1 at each location. Turbulence was modelled using the SST turbulence model. The wall y+ was less than 5 everywhere which Balasubramanian, et al., (2011) deemed sufficient to accurately capture the boundary layer flow. A total pressure was defined as the inlet boundary condition along with the volume fraction of water ($\alpha_L = 1$). At the outlet, the mass flow rate was set. The inlet pressure was then gradually reduced to compute the head drop in the performance curves. The CFD and experimental results showed good correlation. The results of the study found that the best performance was produced by the parabola leading edge shape while a blunt leading edge produced the worst performance due to the high shock losses.

The main aim of Zhu & Chen, (2012) was to further understand the cavitation suppression mechanism of the gap structure impeller. The gap structure impeller consists of a regular rotor with small blade introduced on the suction side of the regular blades. To further understand this mechanism, Zhu and Chen analysed the cavitation characteristics in a low specific speed centrifugal pump. Zhu and Chen predicted the cavitation performance of two centrifugal pumps and compared them with experimental data which showed a good agreement of results. The two impellers were similar with the only difference being that the second impeller had a small vice blade offset from the suction surface of the main blade which created a gap between the overlap area of the main and vice blades. Zhu and Chen adopted a hexahedral meshing strategy to effectively control the grid distribution. The model was split into three domains separated by interfaces at the inlet and outlet locations of the impeller. The conventional impeller had a total of 1.52 million cells while the gap impeller had 1.19 million cells.

O-type grid technology as well as local mesh refinement were used to control the near-the-wall mesh which ensured the requirements of the corresponding turbulence models. The turbulence model that was used was K-Epsilon SST with automatic near wall treatment. Zhu and Chen explain that this model can automatically switch from wall functions to a low Re near wall formulation as the mesh is refined.

To introduce the cavitation component to the numerical modelling, the homogenous multiphase flow model was applied. Bakir's Rayleigh-Plesset cavitation model was selected to calculate the interphase mass transfer rate when the saturation pressure and mean nucleation site diameters were given. To decrease the numerical dissipation in the steady and unsteady simulations, the second order high resolution scheme and second order backward Euler scheme were used separately for the advection and transient terms.

As with the majority of the work reviewed, Zhu & Chen (2012) first modelled a steady simulation and a non-cavitating result was used as an initial guess for the transient cavitation case. For the steady simulation the frozen rotor interface model was used by Zhu and Chen. The frozen rotor reference frame treats the flow from one component to another by changing the frame of reference while maintaining the relative position of the components. For the unsteady simulation however, the transient rotor-stator interface model was used. This motion model takes into account all the transient flow characteristics and allows a smooth rotation between components.

The boundary conditions used by Zhu and Chen are slightly different from the other work that has been reviewed thus far. Zhu and Chen used a total pressure inlet and a mass flow outlet stating that is often more appropriate for the case that assumes the pump is drawing from a static tank. Zhu and Chen used dimensionless coefficients to determine the characteristics of the pump. The coefficients used were the flow coefficient, the head coefficient, the NPSH and the cavitation number. Zhu and Chen explained that it is difficult to get convergent results for the steady simulation when the pump is operating at part load. Zhu and Chen go on to say that the steady simulation is strongly dependent on the relative location of the impeller and the volute. Thus the unsteady simulation is necessary and the data obtained from the transient analysis should be regarded as the ultimate results.

2.7 Pump Scaling Laws

The scaling laws had been used by Smyth (2013) to reduce the massive power consumption of the original impeller, to that required to drive a smaller, similar impeller according to the power available and the laboratory test rig. The smaller impeller, which is to be tested experimentally, would then allow the conclusions from the experimental testing to be useful, providing the scaled impeller

retained the same operating characteristics as the original impeller. The scaling process needed to keep the operating characteristics similar across a range of flow rates and not at the singular operating point to allow a pump curve to be developed using the experimental rig which can then be compared to the meanline and numerical results.

The scaling process looked at the affinity laws described below which are based on the Buckingham Pi Theorem (Smyth, 2013):

$$\frac{Q_a}{Q_b} = \frac{N_a SF^3}{N_b} \tag{2.30}$$

$$\frac{H_a}{H_b} = \left(\frac{N_a SF}{N_b}\right)^2 \tag{2.31}$$

The first affinity law ensures that the inlet flow coefficient is kept constant and determines the flow rate (Q_b) for the scaled pump. The second law was used to calculate the head rise (H_b) across the scaled pump while ensuring that the head coefficient remains constant between the pumps.

To be useful, a scaled item must be geometrically similar, kinematically similar and dynamically similar (Fox, et al., 2010). The first (geometric similarity) is obvious in that the scaled object should have the same shape as the original model. The linear dimensions of the scaled object should correspond to the original model through a constant scale factor. Naturally this is difficult with objects as complex and turbomachinery. The kinematic similarity deals with the velocity vectors whereby at the same points in the different models they need to be in the same direction and only differ by a constant scale factor. The dynamic similarity involves the forces within each model which also need to be in the same direction and vary by the scale factor.

3 Scaled Down Impeller

The scaled impeller was modelled first because, theoretically, it was less computationally expensive and therefore allowed a more detailed study of the effects of different modelling parameters on the solution. The process described below was an iterative one, with various mesh characteristics being used until mesh independence was acquired. During the mesh independence study, one of the aims became the optimisation of tip gap meshing as the impact of cell number on the pressure rise and loss in the tip gap is poorly documented in the literature. While Hellstroom, et al., (2012) used 10 cells in the radial direction between the blade edge and the shroud wall when modelling a compressor operating near surge, other authors fail to mention the level of refinement in this region.

3.1 CAD preparation

The scaled impeller geometry was generated in the original work by Smyth (2013) using AXCENT. The geometry consisted of the impeller hub and blades as a solid and a shroud surface with no tip gap, as seen in figure 3.1.

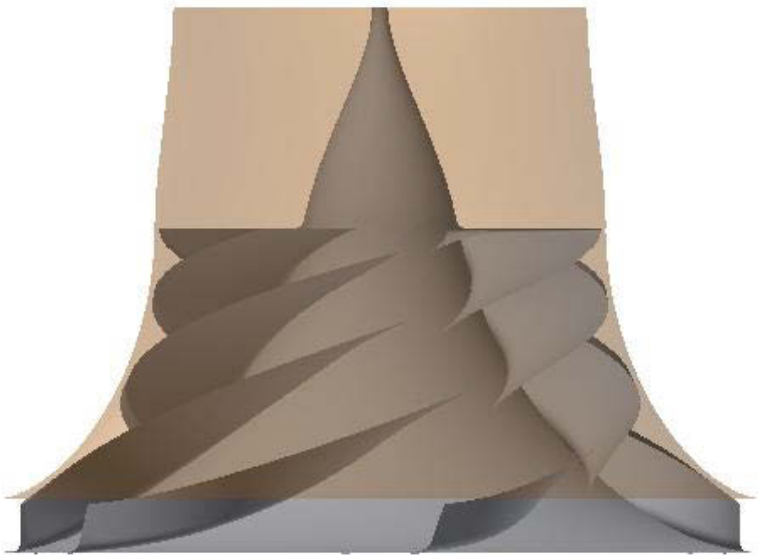

Figure 3.1: Original geometry

Consequently, various steps had to be taken by the author to obtain a more realistic geometry that was suitable for fluid flow simulation. Firstly the shroud was generated as a solid and a tip gap of 0.5 mm was introduced. A solid model of the impeller was the result as seen in figure 3.2. It is standard practice in fluid flow simulations that the fluid region is represented as a solid and the solid body (the

impeller and shrouding) is represented by open space. In other words, a negative of the real life is created. The fluid flow needs a solid representation so that spatial discretisation can occur and the fluid be represented by cells defined by the user. Once the solid model was formed, the impeller was removed from the domain to create a negative of the solid. Figure 3.3 shows the negative of the impeller, in other words, a cavity exists where previously the solid material of the rotor could be found.

Figure 3.2: Shrouded impeller with 0.5 mm tip gap clearance

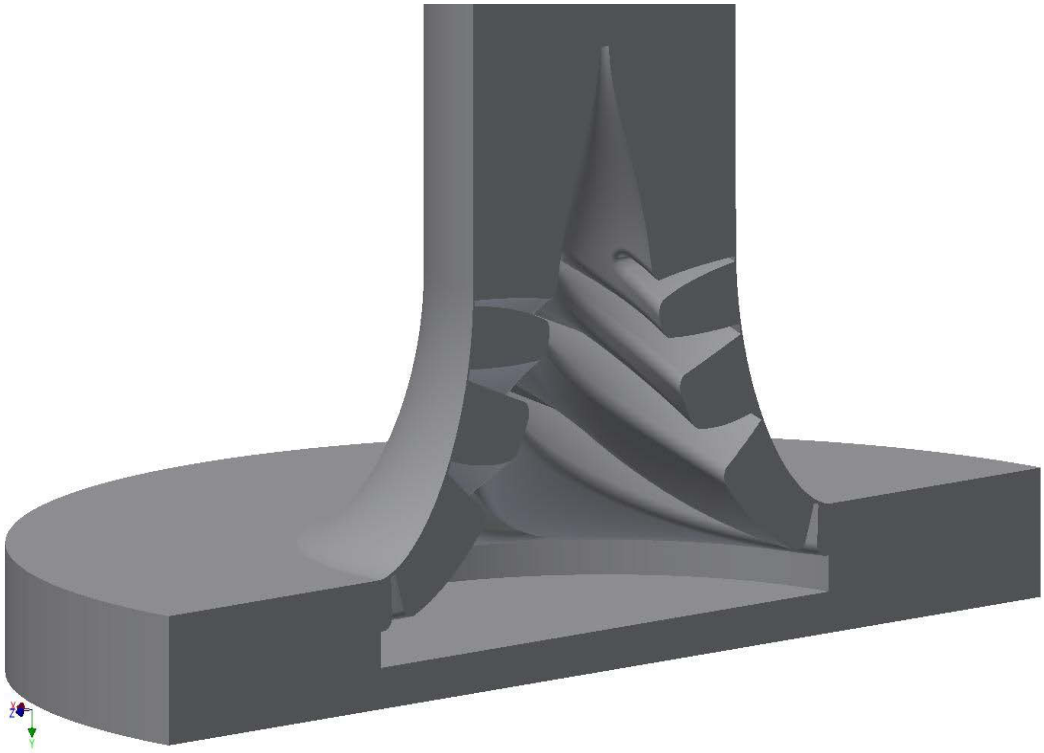

Figure 3.3: Negative of the impeller with 0.5 mm tip gap clearance

3.2 Computational domain

As stated previously, the model consists only of the inlet section, the rotating impeller and an outlet section. The outlet section is not a true representation of the designed or experimental volute. The proposed experimental rig consists of an adapted commercial pump casing whose volute is not suited for the scaled impeller. Complex modifications to the volute are necessary to test the impeller experimentally. As already mentioned, these modifications have not yet been completed, leaving the meanline analysis as the only means of comparison for this numerical study. The meanline analysis provided results at the outlet of the impeller and the experimental rig focuses solely on the impeller, which allowed the impeller to be the main focus of this study. Hence the outlet section of the 3D model consists of a vaneless diffuser with the mass flow rate specified at the final boundary of the model. The use of a vaneless diffuser also allows faster convergence of simulations (van der Merwe, 2012). The outlet surface of the vaneless diffuser was located at a radius of 145 mm. The computational domain can be seen in figure 3.4 with a transparent view on the right-hand side.

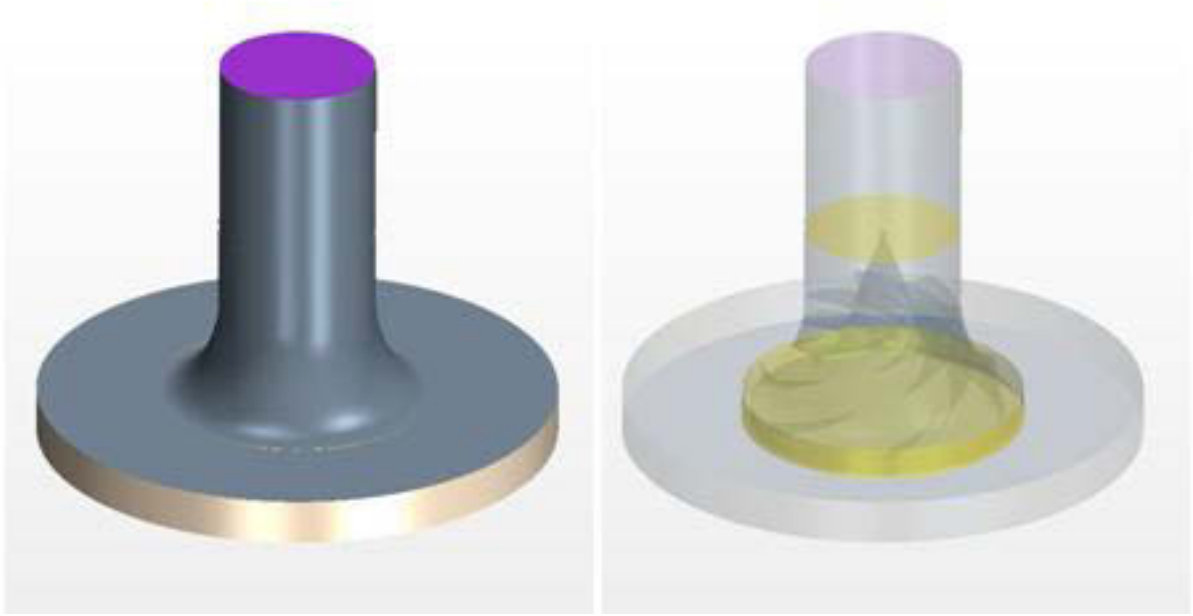

Figure 3.4: Computational domain in standard and transparent view

3.3 Mesh generation

To obtain an accurate solution a study of mesh independence was done. This required an optimisation of the mesh until the change in result from one mesh to the next was negligible. The result was measured in terms of the pressure outlet at the exit of the impeller. Each mesh was an improvement of the previous mesh. In total four meshes were generated which are described below.

Following the common trend of various other works (Barrio, et al., 2010) (Dick, et al., 2001) (Montomoli, et al., 2010) (Bacharoudis, et al., 2008) an unstructured mesh was used to mesh the computational domain away from the walls. Despite various works using tetrahedral and hexahedral meshes (as discussed in the literature review), a polyhedral mesh was used for its low computational cost. To allow accurate capturing of the boundary layer, prismatic layers were generated on all the walls within the model. An iterative process was used to alter the mesh characteristics until mesh independency was reached. After a basic mesh was generated (base size of 5 mm and no refined sections) it was clear from the poor geometric representation of the blade leading edge seen in figure 3.5, that various regions needed to have a finer mesh to allow the geometry to be accurately represented. The original cell size was too large to capture the small leading edges of the blades which are only 0.2 mm thick. Figure 3.5 shows the poor geometric representation of the leading edge (highlighted by the oval outline) prior to mesh refinement.

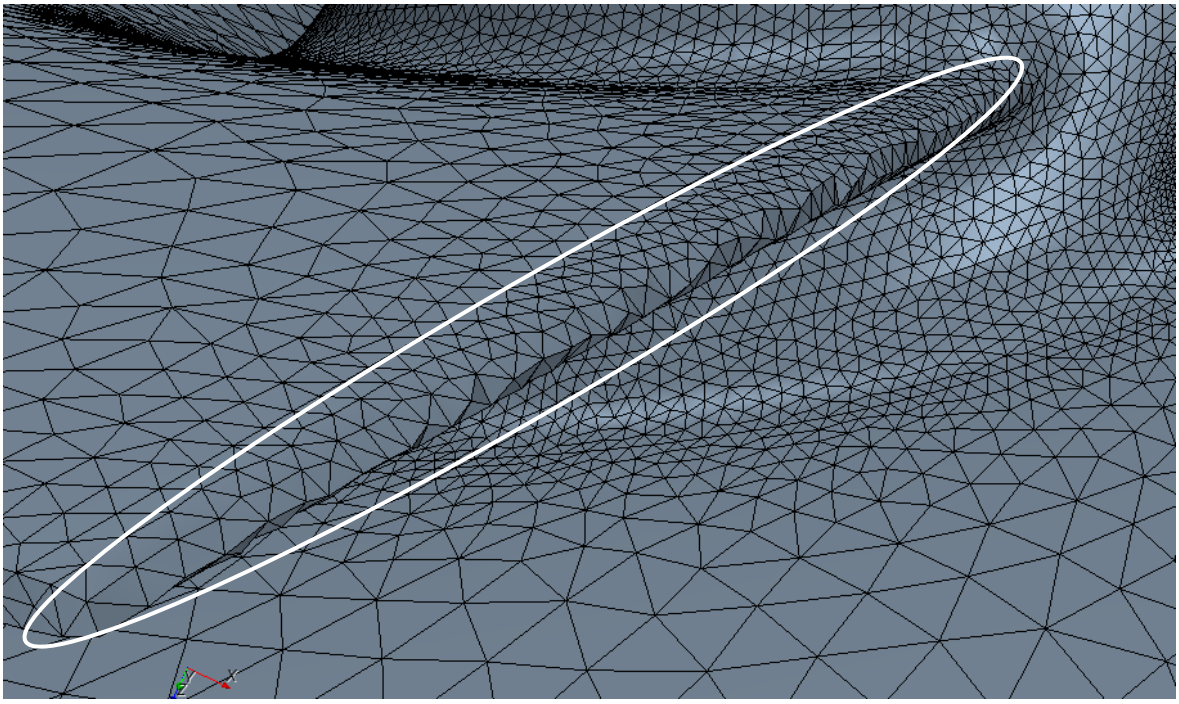

Figure 3.5: Poor mesh on the leading edge of the blades

To overcome the issue, volumetric controls were generated and applied to cylindrical shapes that surrounded the leading edge of each blade which is shown in figure 3.6. The surface and volume mesh values were customised in these regions with a value of 0.2 mm since the leading edge has a thickness of 0.2 mm. The refined blade mesh can be seen in figure 3.7 below. The surface size of the mesh on each blade as well as the hub of the impeller also needed refinement for the fillets between the blade and hub to generate correctly. The tip of the impeller also required a custom mesh to provide the detailed geometry.

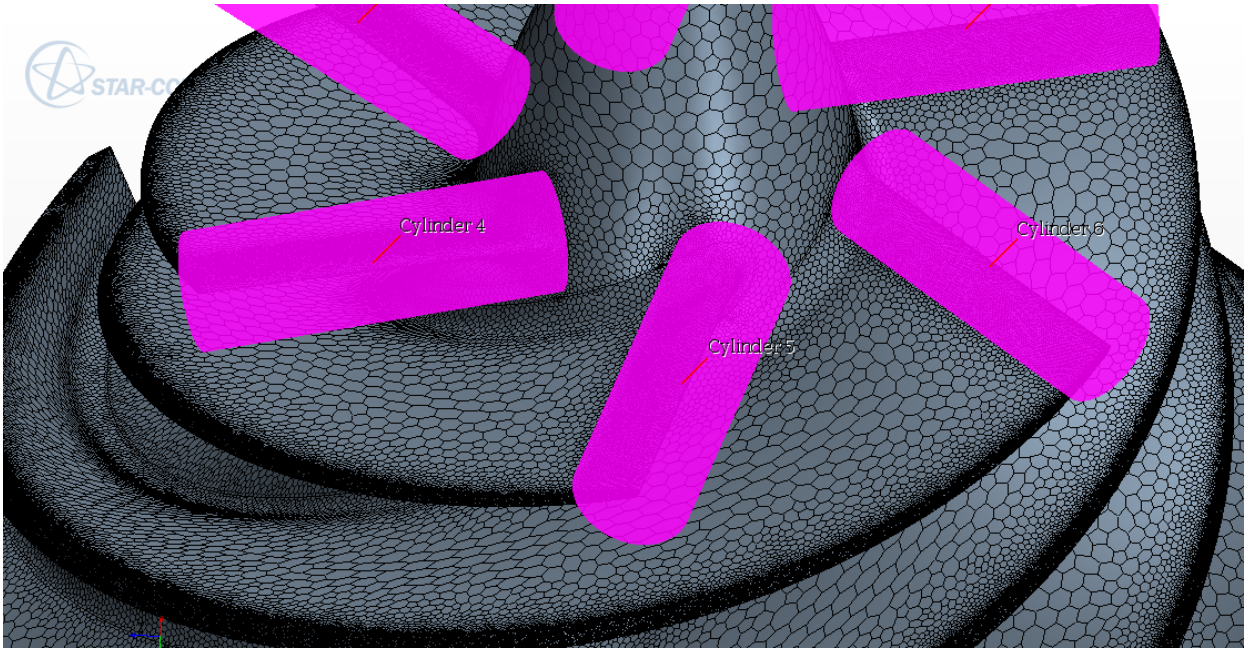

Figure 3.6: Volumetric controls on the leading edges

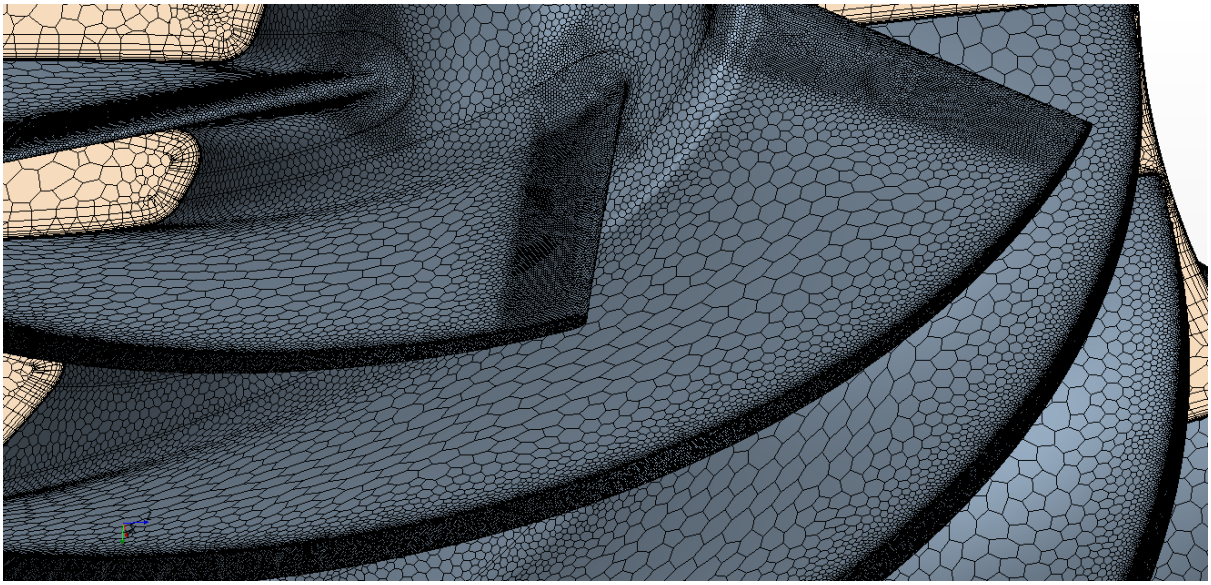

Figure 3.7: Refined mesh on the blades

The tip gap of the model, between the blade edge and the shroud, was only 0.5 mm. This meant that the general mesh settings were not suitable for accurate flow capture in the tip gap as seen in figure 3.8 where they are only two polyhedral cells. As already stated, the number of cells necessary for accurate modelling of the flow in this clearance space is poorly documented in the literature. A volumetric control was developed that encompassed the tip gap. This allowed for customised mesh generation in the tip gap resulting in a greater degree of accuracy. The surface mesh, volume mesh and prism layers were all customised for the tip gap.

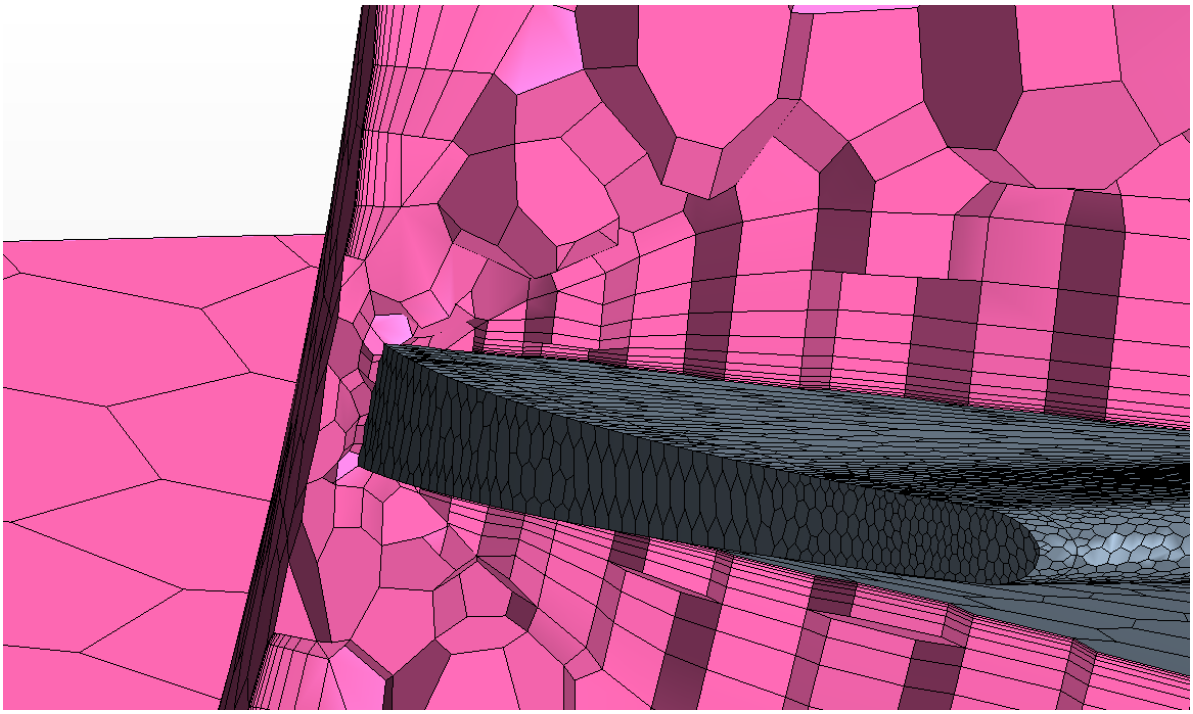

Figure 3.8: Poor tip gap meshing

The first simulation run that had reasonable results had the following mesh characteristics:

Table 3.1: Mesh characteristics

General Values		Base size (mm)	5
		Minimum surface size (mm)	1.25
		Absolute surface size (mm)	5
		Prism layer number	10
		Prism layer thickness (mm)	2
Refined Areas	Tip Gap	Base Size (mm)	0.1
		Prism layer number	2
		Prism layer thickness (mm)	0.1
		Number of cells	7
	Blade	Leading edge (mm)	0.2
		Minimum surface size (mm)	0.5
		Absolute surface size (mm)	2
	Hub	Minimum surface size (mm)	2
		Absolute surface size (mm)	3
Total Number of Cells			7 398 960

After each mesh had been successfully generated the model was run at different flow rates which were determined by the meanline data which is provided in Table 3-2. After each run the results were analysed and the mesh was improved with particular attention focusing on the tip gap and wall Y+ value.

Table 3.2: Meanline data points for scaled simulations

Mass flow rate (kg/s)	12.73	15.46	18.19	20.92	23.64
Speed (rpm)	5000	5000	5000	5000	5000

In addition to Star CCM+ performing, automatically, certain mesh validation tasks where unclosed cells, invalid cells, zero area faces and zero/negative volume cells are noted, various visual checks carried out by the author were used to determine if the mesh was acceptable. The first check was the skewness angle of the cells. The skewness angle is a measure of the orientation between cells. The skewness angle determines if the cells on either side of a face are orientated in such a way as to allow for the effective diffusion of quantities. To obtain diffusive fluxes with good accuracy and robustness, the line connecting neighbouring cell centroids should be as close to orthogonal as possible to the face between the cells. Skewness angles of 90^0 and greater can cause convergence issues. It is suggested that the cell skewness angle remain below 85^0 (CD-Adapco, 2013). The distribution of cell skewness of the final mesh can be seen in figure 3.9 where the majority of the mesh has a low cell skewness angle, with the exception of a few points where the skewness crept up to 88^o.

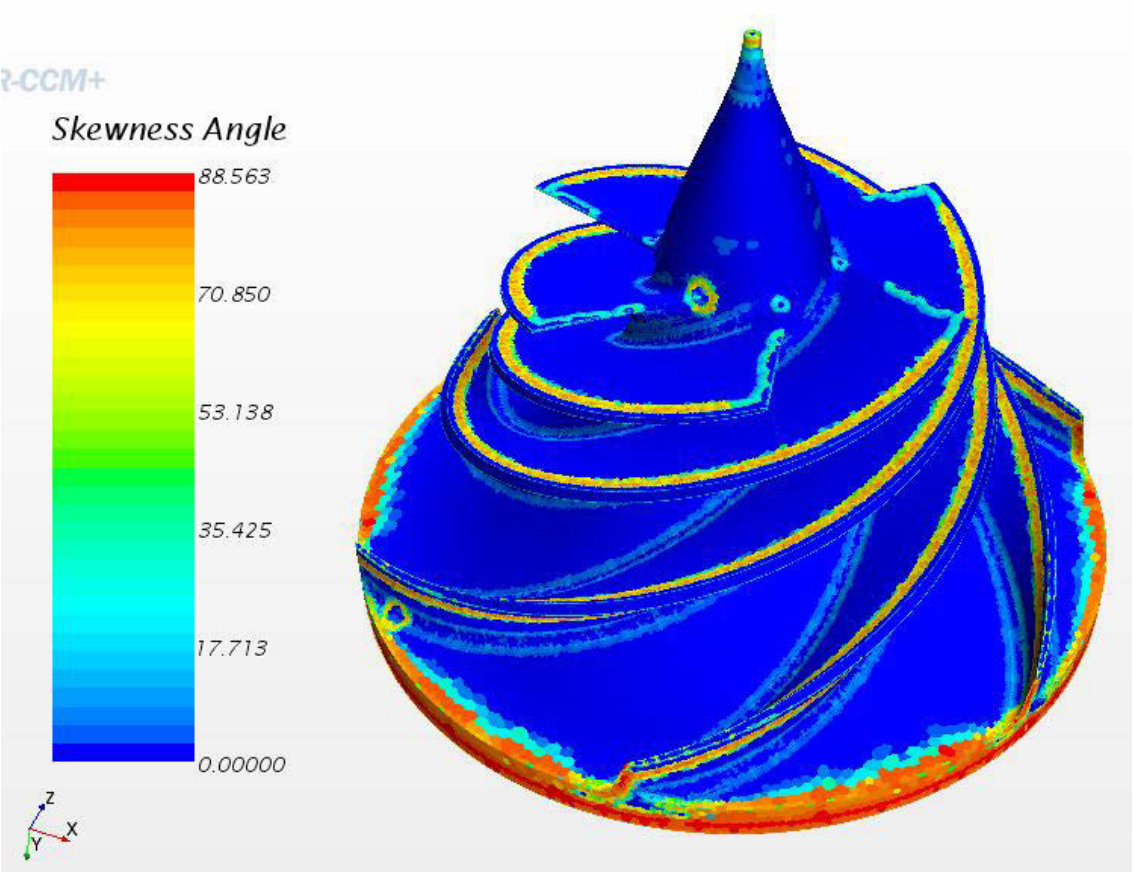

Figure 3.9: Cell skewness angle

The second visual check of the mesh used the cell relative velocity. By looking at the cell relative velocity on a surface one can see whether the velocity from one cell to the next is a smooth transition. This can be aided by increasing the number of colours used in the scalar scene from 32 to 512. Figure 3.10 shows, usually, a smooth transition of velocity from one cell to the next and each individual cell cannot be identified by a discontinuity or step in velocity. Naturally the velocity of the cells is increased as one moves outward in a radial direction. If the cell size is too large, the relative velocity scene would show steps or 'jumps' in the relative velocity rather than a smooth transition.

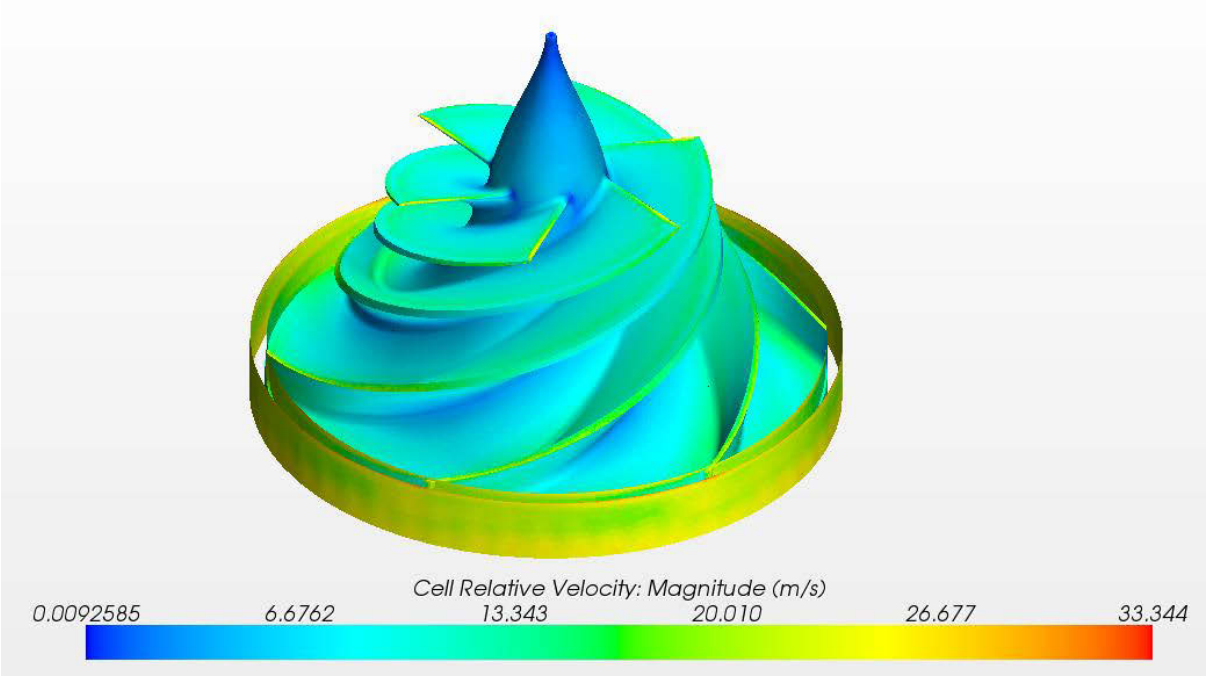

Figure 3.10: Cell relative velocity

Despite the tip gap having a customised prism layer mesh, the prism layers failed to generate due to the close proximity of the blade wall and the shroud. The tip gap prism layers were only generated successfully in a later mesh configuration. Although the first mesh resulted in high Y+ values the aim of the second mesh was to improve the tip gap meshing rather than address the high Y+ values which were addressed at a later stage. The second mesh only had one difference to the first mesh which was a smaller cell size in the tip gap in the hope that the tip gap prism layers would then generate. This however was not successful.

There are several factors that control the generation of the prism layers in Star CCM+. When two boundaries are close together the prism layers are reduced and eventually deleted if the gap is too small.

- *The Gap Fill Percentage* controls the portion of a gap that is filled by prism layers when two boundaries are in close proximity with one another. The default setting is 25% and was changed to 40% in this work. This meant that in a narrow gap, the prism layers would be able to make up 40% of the gap width. Other factors were also altered to assist the formation of the prism layers in the tip gap.
- *The minimum thickness percentage* is used to calculate a threshold thickness. The overall prism layer thickness is reduced until it reaches the threshold. Once the prism layer thickness reaches the threshold thickness, the prism layers will not be generated. This prevents the formation of several layers, or an excessive number of layers, being squeezed into a thin

section. The minimum thickness percentage is prescribed as a percentage of the overall thickness with the default being 10%.

- The final factor that controls prism layer generation in small gaps is the *Layer Reduction Percentage* which is used to calculate a threshold thickness below which the number of prism layers is progressively reduced (as the overall thickness is reduced). This allows the prism layers to form in small gaps while maintaining an adequate aspect ratio. Once the gap fill percentage had been increased the prism layers formed on the blade and shroud surface as seen in figure 3.11.

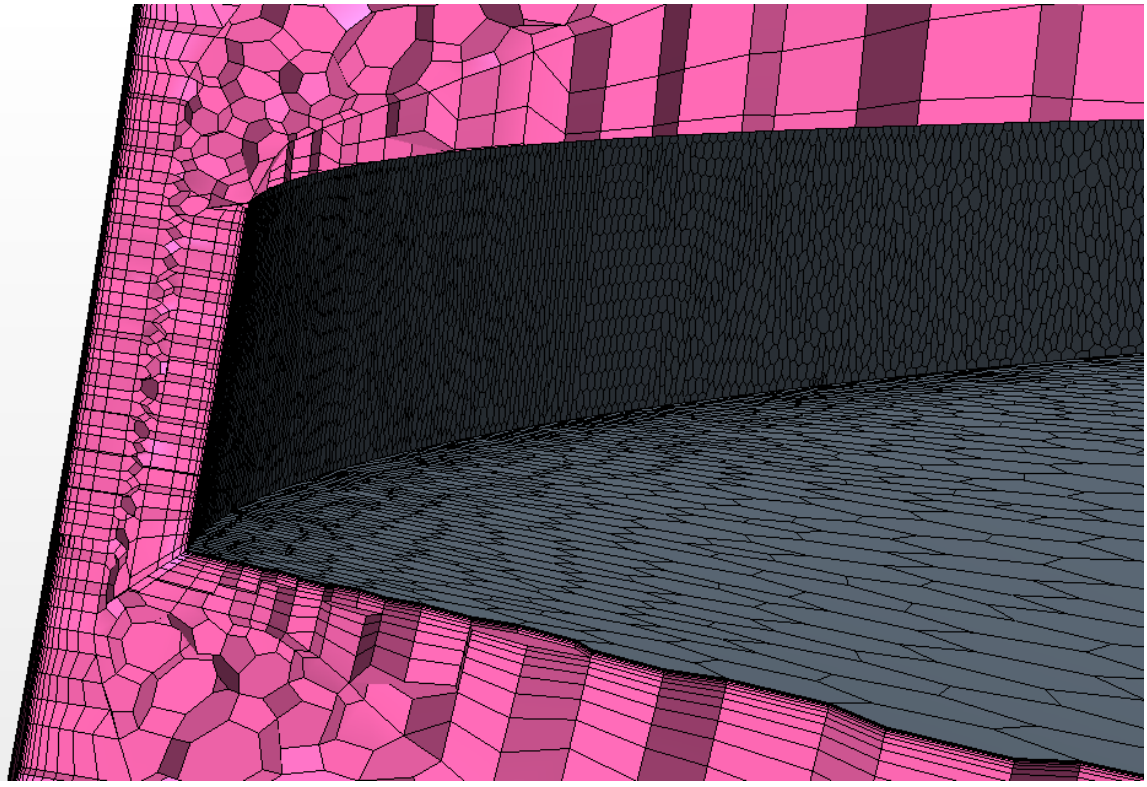

Figure 3.11: Prism layers in the tip gap

After the second mesh there were various factors and mesh qualities that were altered one-by-one until the third mesh was successful. In the process various different unsuccessful arrangements of the prism layers in the tip gap were generated. The third mesh also returned a large improvement in the Y+ value of the model. This was achieved by increasing the number of prism layers on the solid surfaces. In an attempt to get a low Y+ value while maintaining a low computational cost the third mesh applied different prism layers values to the different regions. The inlet had 8 layers at an overall thickness of 2 mm while the rotating region and the outlet had 12 and 13 layers respectively with an overall thickness of 1.8 mm. The tip gap was up to 3 layers with an overall thickness of 0.2 mm. This reduced the Y+ values considerably, with the exception of the inlet which can be seen in table 3.3.

The width of the prism layers was also reduced by decreasing the surface size of the cells on the walls upon which the prism layers are generated. This prevents the generation of elongated cells which can cause irregularities.

Table 3.3: Y+ values of mesh 2 and 3

Surface	Mesh 2 Y+	Mesh 3 Y+
Inlet walls	3	3.5
Impeller	14	3.5
Tip gap	>40	26
Outlet walls	10	2

The method of prescribing the prism layers was changed in the fourth mesh. Here, rather than prescribing the stretch factor (which was always left at the default of 1.5), the first cell thickness was now prescribed. This allowed a target Y+ value to be set and the corresponding cell size to be calculated, as discussed in section 2.1 earlier. The target Y+ value was approximately 1 everywhere except the tip gap. In the tip gap the Y+ target was approximately 2 in an attempt to keep the computational time down. As discussed in the literature review the Y+ calculations are based on the wall shear stress which was determined to be 1200 Pa through a scalar scene (figure 3.12). The scene shows that the majority of the impeller has a shear stress of less than 800 Pa but the shear stress was taken at the edge of the blades and end of the blade passages where it is higher. This means that the calculation will be true for these regions as well.

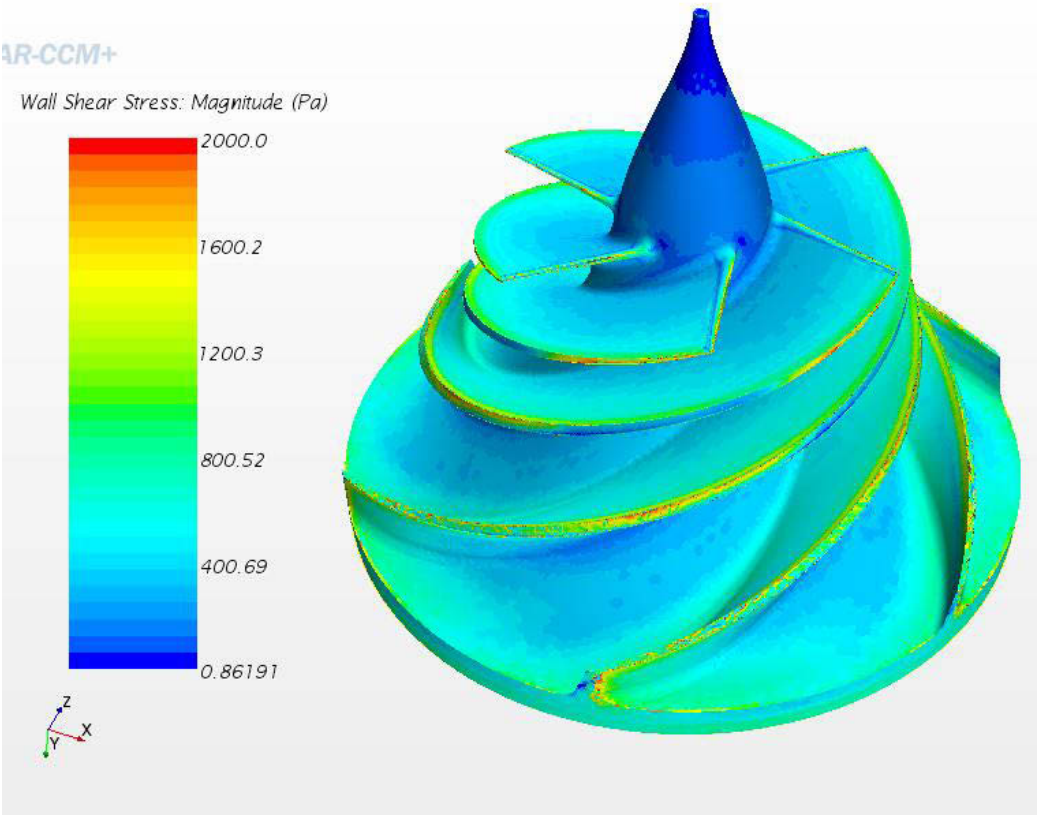

Figure 3.12: Wall shear stress

The knowledge of the shear stress allowed the reference velocity (u^*) to be calculated, since density is constant and recalling from Section 2.1 that,

$$u^* = \sqrt{\frac{\tau_w}{\rho}}.$$

The size of the first cell could then be calculated since

$$y^+ = \frac{u^* y}{\nu}.$$

The individual prism layer values can be seen in table 3.4 with the scalar scene of the Y+ values in figure 3.13.

Table 3.4: Prism layer parameters for the final mesh

Variable	Inlet	Rotating	Outlet	Tip Gap
Prism layer thickness (mm)	2	1.8	1.8	0.2
Number of Prism Layers	12	15	15	6
Near-wall layer thickness (mm)	0.008	0.002	0.002	0.004

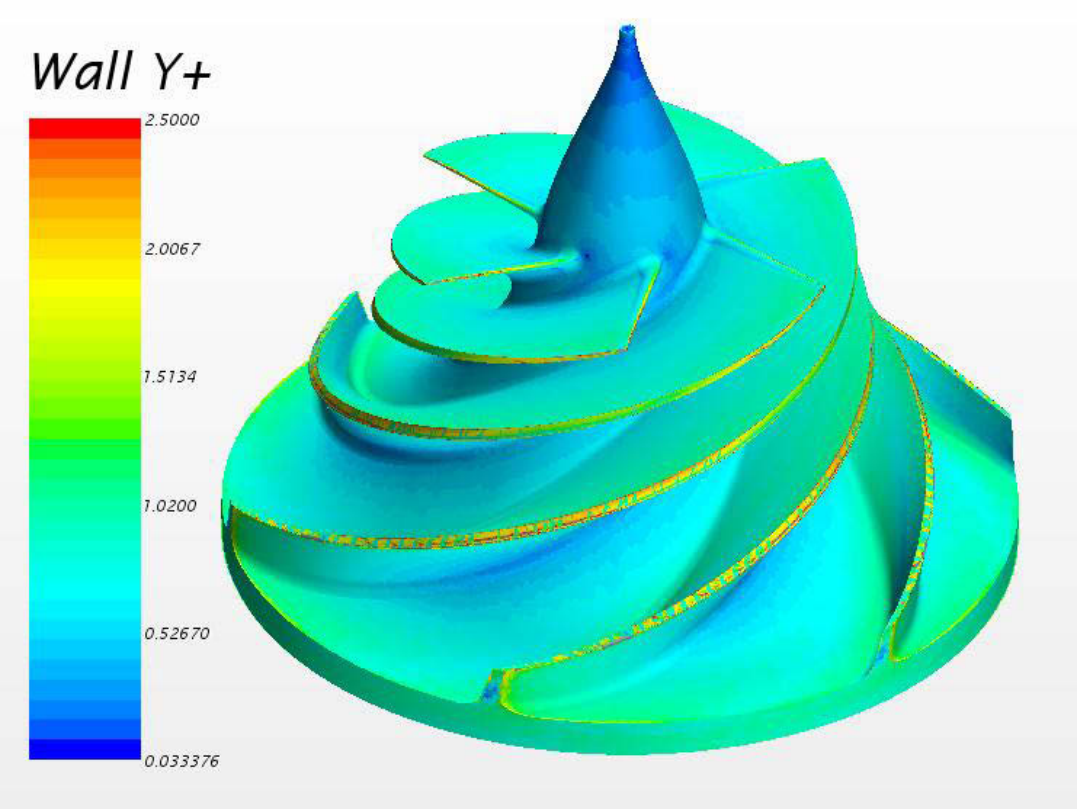

Figure 3.13: Wall Y+ values

The final (fourth) mesh characteristics can be seen in table 3.5, not forgetting the individual prism layer specifications given above. An important feature to note in table 3.5 is the number of cells in the tip gap, which was double that of the first mesh. The total number of cells is also an important figure at just over 12.3 million cells.

Table 3.5: Final mesh parameters

General Values		Base size (mm)	5
		Minimum Surface size (mm)	1.25
		Absolute Surface Size (mm)	5
		Prism layer number	15
		Prism layer thickness (mm)	1.8
Refined Areas	Tip Gap	Base Size (mm)	0.1
		Prism layer Number	6
		Prism layer Thickness (mm)	0.2
		Number of Cells	14
	Blade	Leading edge (mm)	0.2
		Minimum Surface Size (mm)	0.5
		Absolute Surface Size (mm)	2
	Hub	Minimum Surface Size (mm)	1.25
		Absolute Surface Size (mm)	2.5
Total Number of Cells			12 369 550

When the different mesh configurations were compared the value of the output static pressure at the exit of the impeller was used as the reference. The results of the mesh study can be seen below in table 3.6 where the predicted pressure difference between each mesh is given. The same result can be seen in the graph that follows (figure 3.14). Although the difference in the pressure measured at outlet was low (maximum 1.12%) between mesh and 1 and 2, the mesh was improved further to decrease the wall y+ values as well as to further refine the tip gap mesh to study the effect that the tip gap had on the solution. The table and figure show that the mesh optimisation had minimal effect on the results of the CFD model where between mesh 2 and mesh 3, the maximum change in result was on 2.31%. The final mesh optimisation between mesh 3 and 4, yielded less than a 1% difference in result.

Table 3.6: Table of mesh independence results

Flow rate (kg/s)	Mesh 1 to 2	Mesh 2 to 3	Mesh 3 to 4
12.73	0.34%	0.34%	0.17%
15.46	0.54%	0.36%	0.18%
18.19	1.12%	1.11%	0.18%
20.92	0.20%	2.31%	0.39%
23.64	1.04%	1.83%	0.20%

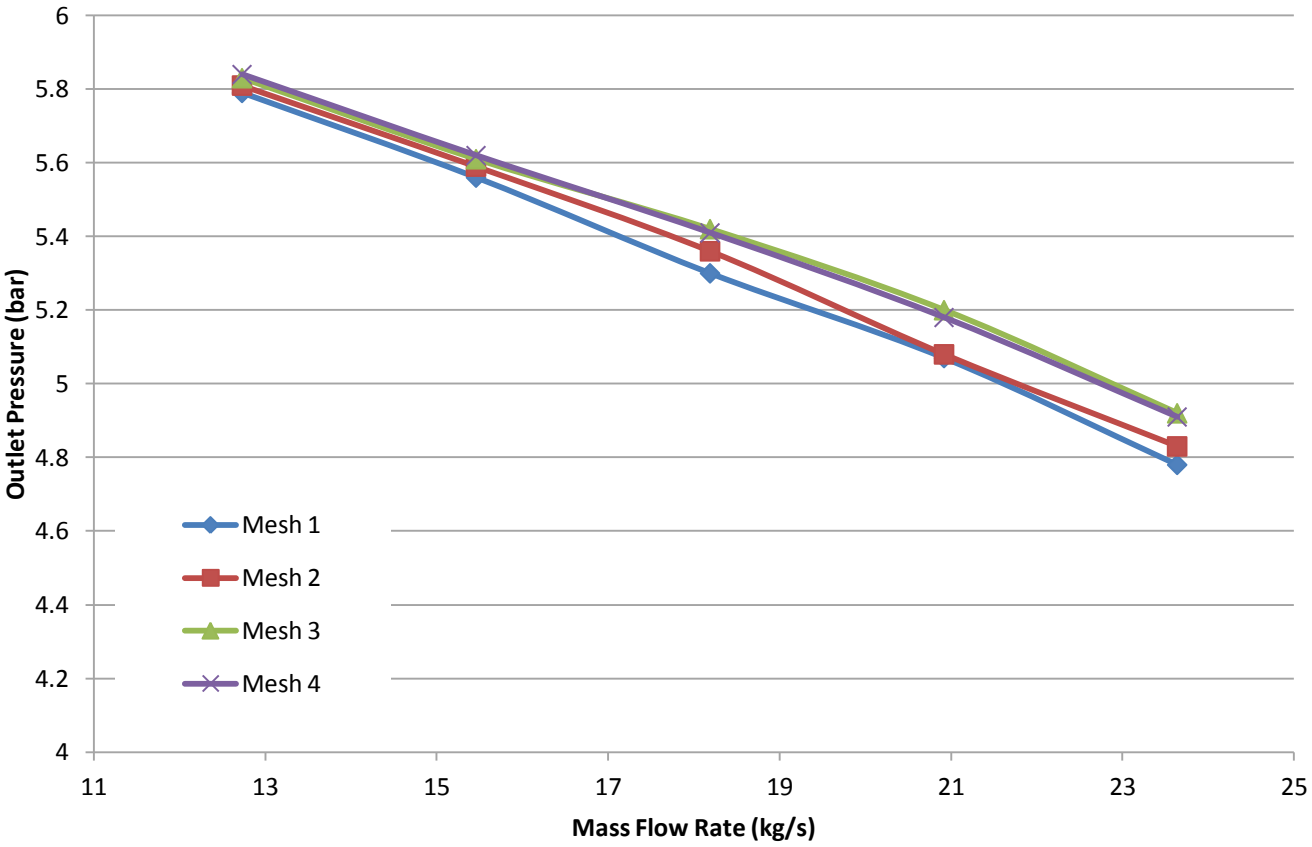

Figure 3.14: Mesh independence results

3.4 Model Development (Physics)

The fluid used in the CFD model of the scaled impeller was water, as it was the fluid to be used in the experimental testing. The turbulence model used was the SST K-Omega model since it has been used with good results as discussed in the literature review. Although the turbulence suppression model was selected as part of the physics models, it was not engaged on any of the walls as the transition from laminar to turbulent was not a key focus of this work. The turbulence suppression model allows the location of the transition point to be set. The "All Y+ Treatment" was used as the values for the Y+ were not below 1 everywhere, which is a requirement for the "Low Y+ Treatment" model.

It must be noted that the use of Double Precision was investigated. Using Double Precision in Star CCM+ requires a separate download from the Star CCM+ portal. Several simulations were run using single precision and then run again using double precision. The result was unchanged. The only notable difference was the increase in the solver run time which was due to the added memory of the

simulation. Despite the unchanged results, the unsteady simulations for both impellers were run using double precision to allow for greater accuracy when the cavitation model was run.

The boundary conditions consist of a stagnation inlet where the total pressure and temperature are defined and a mass flow at outlet. The parameters used at these boundaries were set by the meanline design process. The idea behind these conditions is that they allow the outlet pressure to be measured which in turn leads to the production of the pump curve. The pump curve allows for quick comparisons to be done with experimental and meanline analysis. The same conditions and method of comparison were used by Balasubramanian, et al., (2011), Shojaeefard, et al., (2012) and Dick, et al., (2001).

In addition to these conditions, other boundary conditions were implemented to provide a more accurate model. The first condition relates to the shroud walls. While they are inside the rotating region of the model, they do not rotate in real life. To prevent these walls from rotating in the CFD model, the wall tangential velocity specification was altered. The method for defining the tangential velocity was set to *None* and the reference frame set to *Absolute*. This ensured the shroud walls remained stationary. All other walls were also set to the no-slip condition with a surface roughness value of 100 µm (which appears as a common value in the literature).

With regard to the initial conditions of the model, the only parameter that was initialized was the velocity in the axial direction (normal to the inlet surface). This was done in an attempt to assist the convergence of the model. The reference pressure was also set to 1 atm.

As already stated, the steady analysis made use of a rotating reference frame. This technique treats the flow from one component to another by changing the frame of reference while maintaining the relative position of the components. This meant that the impeller was placed in a rotating reference frame while the inlet and outlet regions were in a stationary frame of reference. Rotational terms are included in this type of simulation but the transient terms are neglected (Shojaeefard, et al., 2012). This provides a good starting point for the unsteady simulation and is a common method in different works.

To ensure that the rotation was applied to the impeller correctly and that it was rotating about its own axis, a new coordinate system was created. This coordinate system was created on the base of the impeller, with its ‘z’ axis being the rotational axis of the impeller. The direction of the rotation was dependent upon the orientation of the new ‘z’ axis. The basic boundary conditions that were applied to the model can be seen in table 3.7.

Table 3.7: Scaled model boundary conditions and parameters

Parameters	Mass Flow rate (kg/s)	12.73	15.46	18.19	20.92	23.64
	Speed (rpm)	5000	5000	5000	5000	5000
Stagnation Inlet	Pressure (bar)	0.34	0.34	0.34	0.34	0.34
	Temperature (K)	300	300	300	300	300

3.5 Steady State Results

To allow the meanline data, and eventually the experimental data, to be correlated with the CFD simulations, pressure was plotted as a function of flow rate. The same procedure was carried out by Shojaeefard, et al., (2012) in a numerical study of the effects of certain geometric characteristics on the performance of a centrifugal pump. Dick, et al., (2001) also used this method of correlation in the performance prediction of a centrifugal pump when comparing results between the CFD predictions and the experimental results. The pressure was measured on a cylindrical plane that was placed at the outlet of the impeller, as seen in figure 3.15. The surface (area) average was taken and compared to the mixed flow outlet pressure given by the meanline data. The mixed flow outlet was used instead of the primary or secondary flow zones as the CFD results were taken over the entire surface making it more accurate to compare the CFD results to the mixed flow outlet.

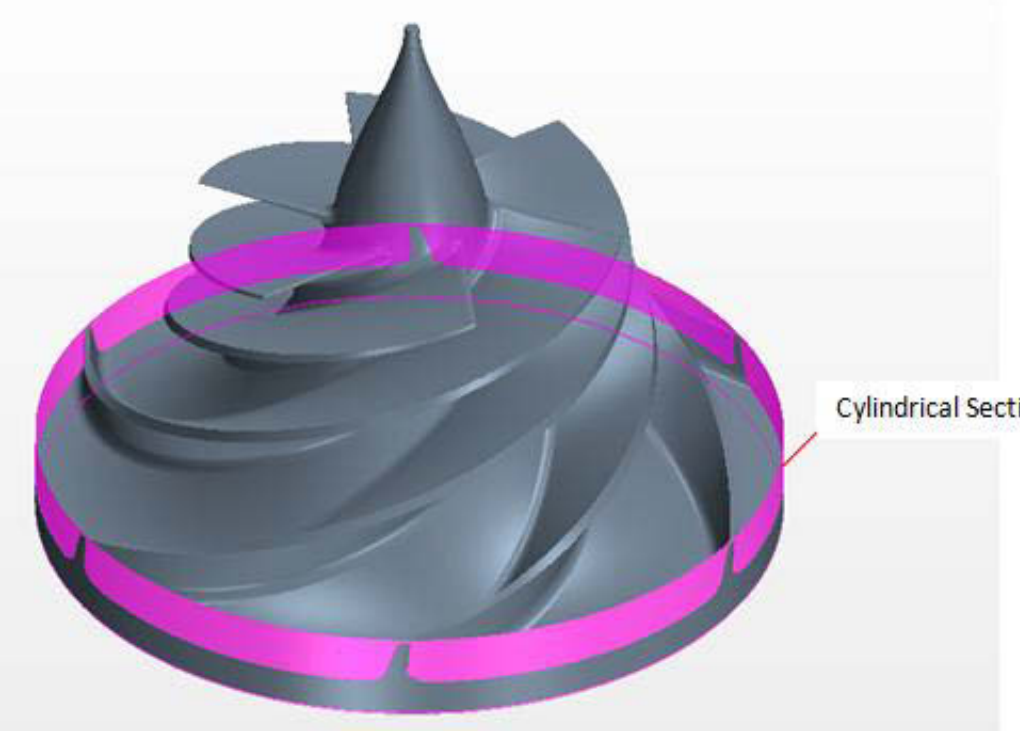

Figure 3.15: Cylindrical plane on which the output was measured

Naturally the convergence of the solution had to be considered before the results could be accepted. Convergence was deemed acceptable based on the status of the residual monitor and the stability of the pressure plot. Figure 3.16 shows the residual plot for the simulation run at the rotor's operating point for the final mesh. Figure 3.16 shows that the residuals have decreased by four orders of magnitude, indicating a stable level of convergence. The stability of the pressure graph can be seen in figure 3.17 which shows that the solution has converged and is steady. In terms of computational time, each simulation for the final mesh ran at approximately 20 seconds per iteration for 2000 iterations, yielding a total time of approximately 11 hours.

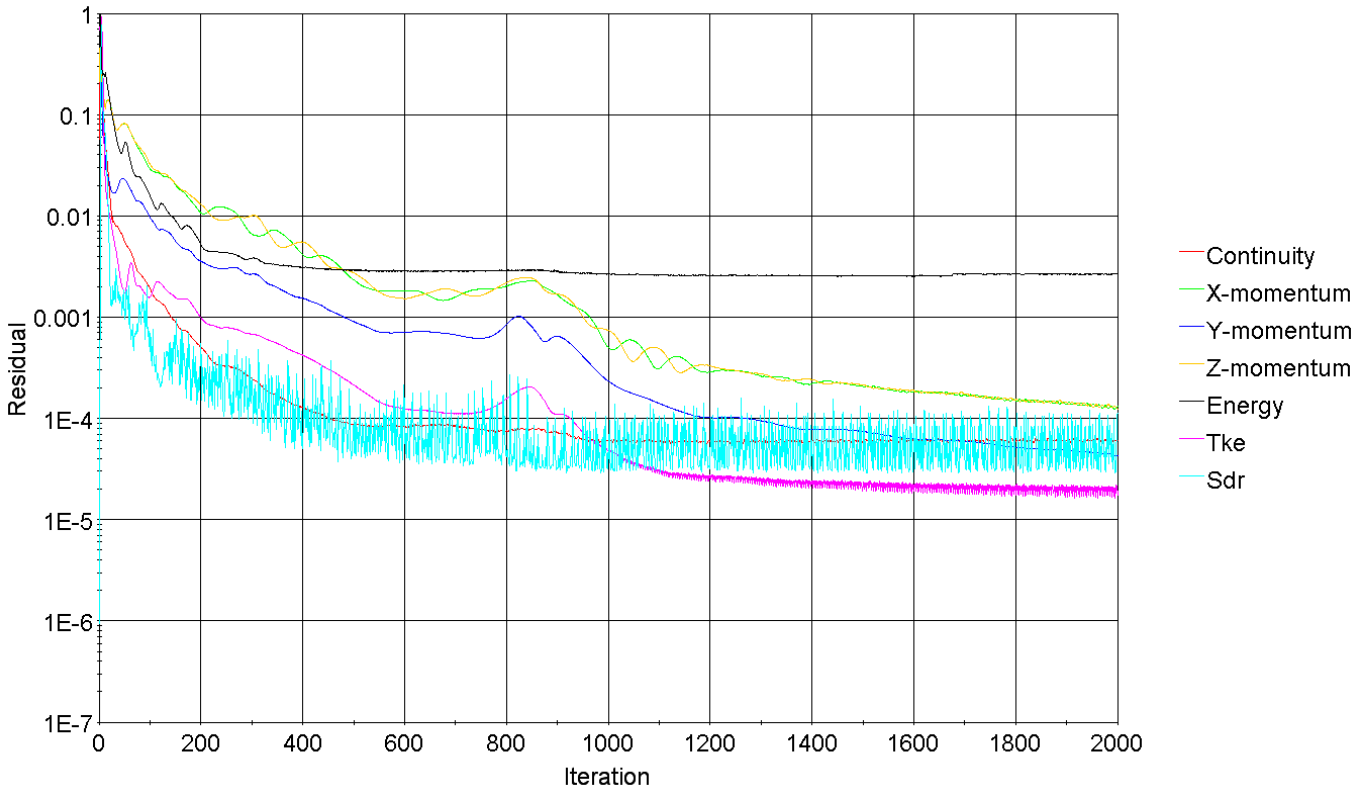

Figure 3.16: Residual plot

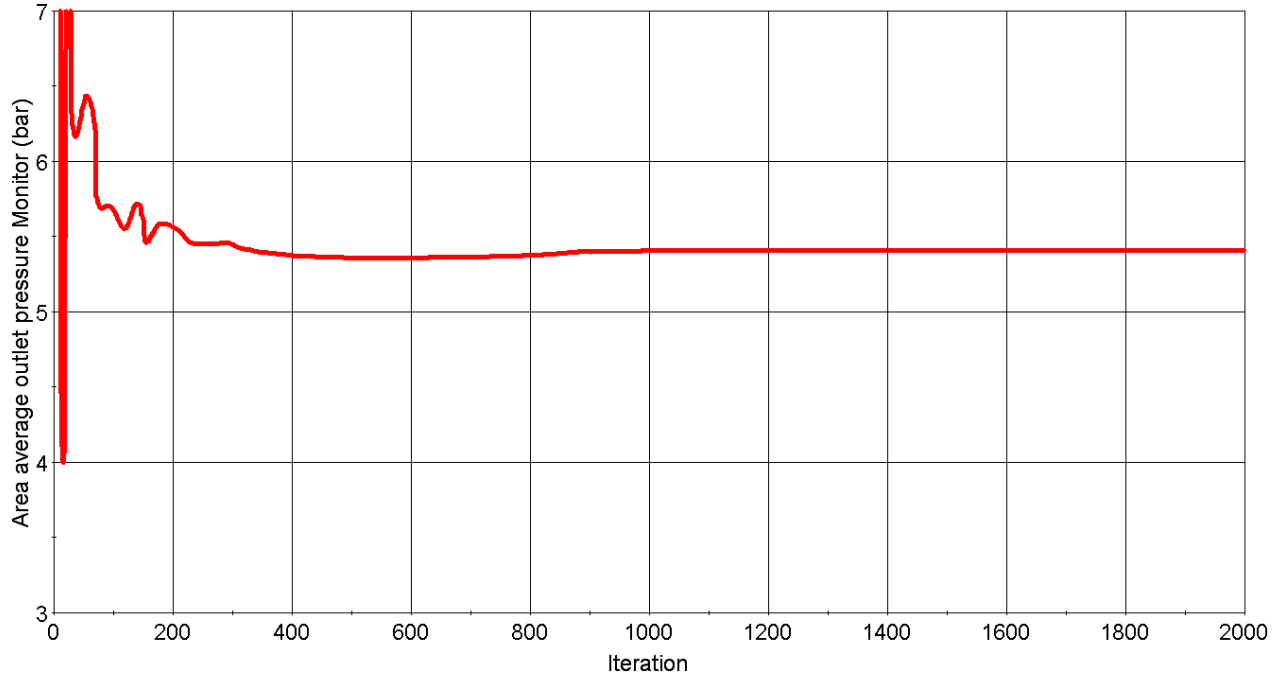

Figure 3.17: Outlet pressure plot

The final mesh that was used generated the following results:

Table 3.8: Final steady state parameters and results

Mesh 4						
12 369 550 cells						
Parameters		**Stagnation Inlet**		**Outlet Pressure (bar)**		**Difference**
Mass Flow rate (kg/s)	Speed (rpm)	Pressure (bar)	Temperature (K)	Meanline	CFD	Difference
12.73	5000	0.34	300	5.7	5.84	2.35%
15.46	5000	0.34	300	5.23	5.62	6.93%
18.19	5000	0.34	300	4.75	5.41	12.28%
20.92	5000	0.34	300	4.19	5.18	19.08%
23.64	5000	0.34	300	3.51	4.91	28.46%

The results can be visualised graphically in the graph below. In the scaled model the numerical predictions are always larger than what the meanline data suggested. The results show that the meanline data and numerical 3D predictions become increasingly different as the mass flow rate is increased. For low flow rates, the results show a good similarity. However, as the flow rate is increased the meanline data has a greater head drop-off than the CFD predictions. At the lowest flow rate (70% of the operating point) the difference between the two sets of results is only 2.35%. Yet, at 130% of the operating flow rate the difference increases to 28.46% which is a drastic increase. This shows that the meanline programme captured the characteristic head drop that occurs at high flow rates to a greater extent than the CFD model. Pump performance curves generally have a large decrease in the outlet pressure as the flow rate moves past the operating point. The meanline results capture this pressure decrease much better than the CFD model. Several other works indicate a higher numerical prediction than the meanline design data especially at higher flow rates. One example of this is Van der Merwe (2012) who designed a centrifugal air compressor impeller. Shojaeefard et al. (2012) also found that at higher flow rates the CFD predictions were not able to capture the head drop-off. Although the steady state result shows poor correlation at higher flow rates, the full scale impeller will show an improvement in this regard (Chapter 4). An interesting point that was noted was the effect of improving the Y+ values and increasing the number of cells in the tip gap. Rather than the pressure decreasing with the refined mesh, the outlet pressure actually increased, moving further away from the meanline predictions.

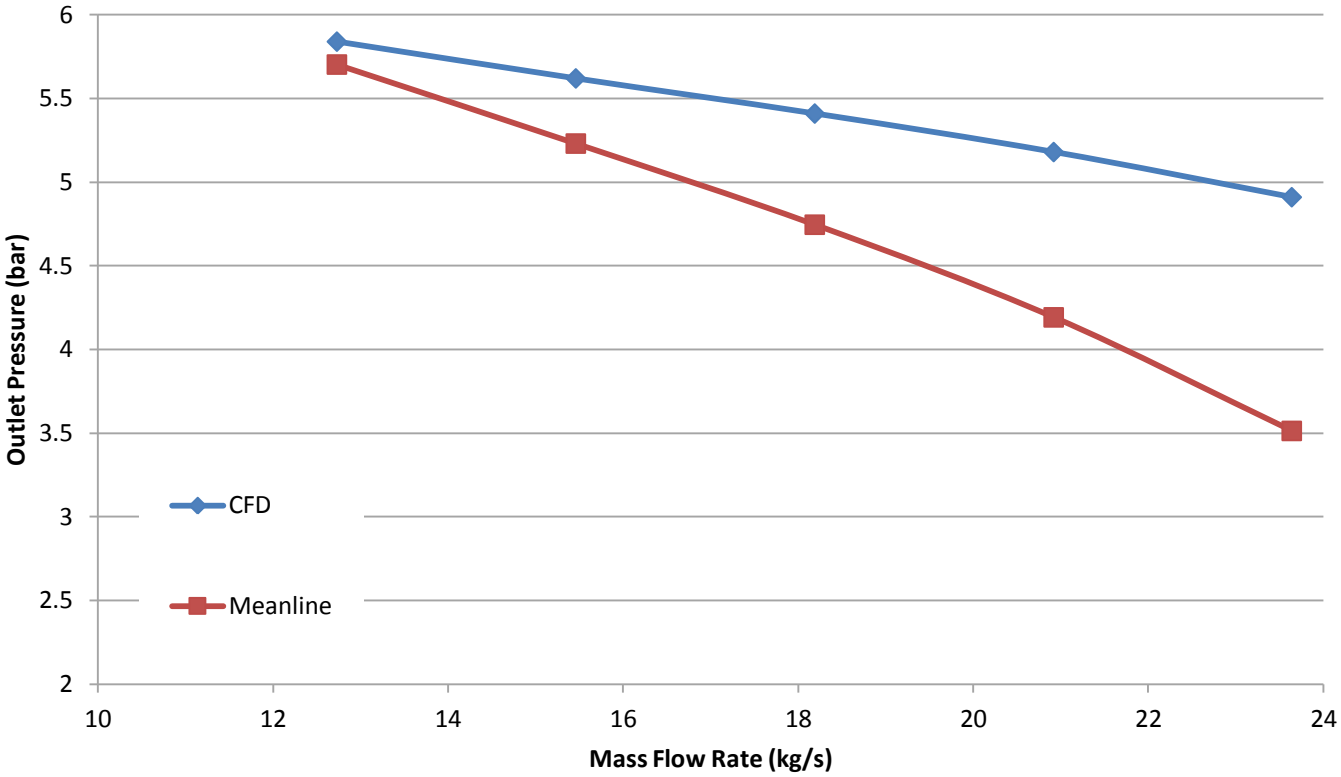

Figure 3.18: Final steady state results compared with the meanline predictions

Although the steady state model does not have the cavitation model implemented, a general idea of the cavitation can be seen through the pressures in the system. A scalar scene (figure 3.19) of pressure on the impeller shows that the pressure around the leading edge is below the vapour pressure of the fluid. Theoretically this indicates a small area of cavitating flow.

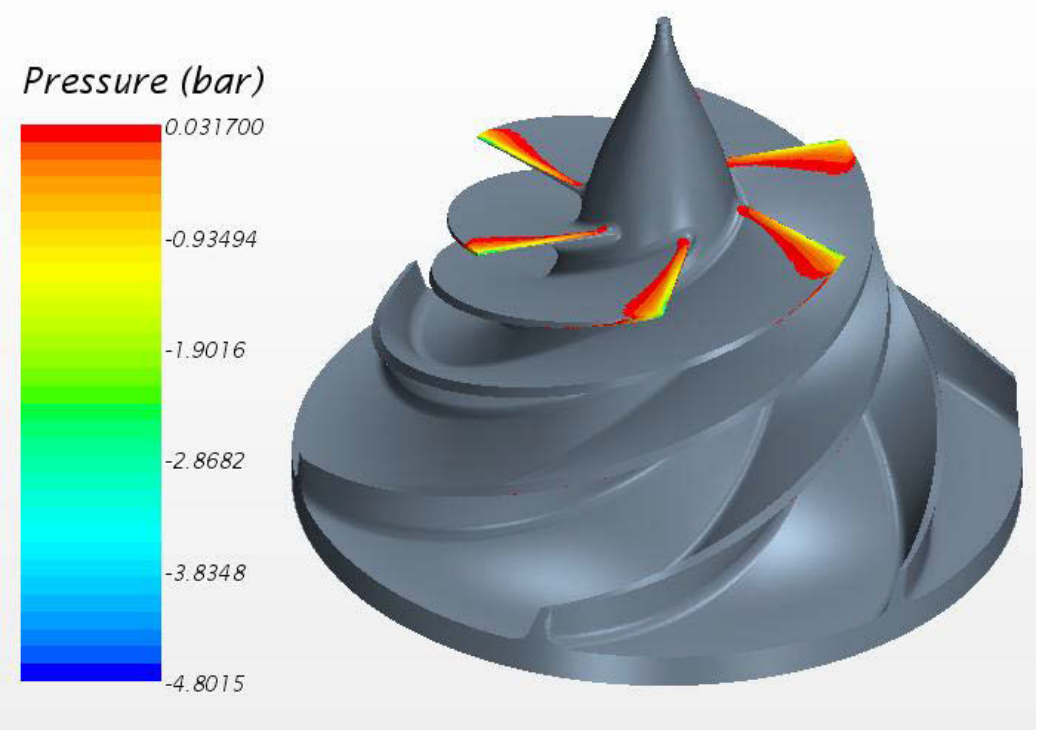

Figure 3.19: Low pressure regions

Figure 3.20 shows a 2D slice through the impeller. The scene shows shortened 3D streamlines running through the system which offers an insight into the smaller rotational swirls that would be missed using regular streamlines. The vortices at the outlet of the impeller can be seen which are due to the narrow vaneless diffuser.

As previously stated, the experimental rig needed to test the scaled impeller and provide the validation for the numerical analysis has not yet been completed. Once the rig is finalised and the impeller tested, a clearer understanding of the impeller's performance at higher flow rates may be established as part of ongoing research. The experimental data are needed to confirm the behaviour of the impeller so that the full scale CFD model can be used as validation for the meanline design. This is a necessity since experimental testing of a full size impeller is impractical given the power requirements.

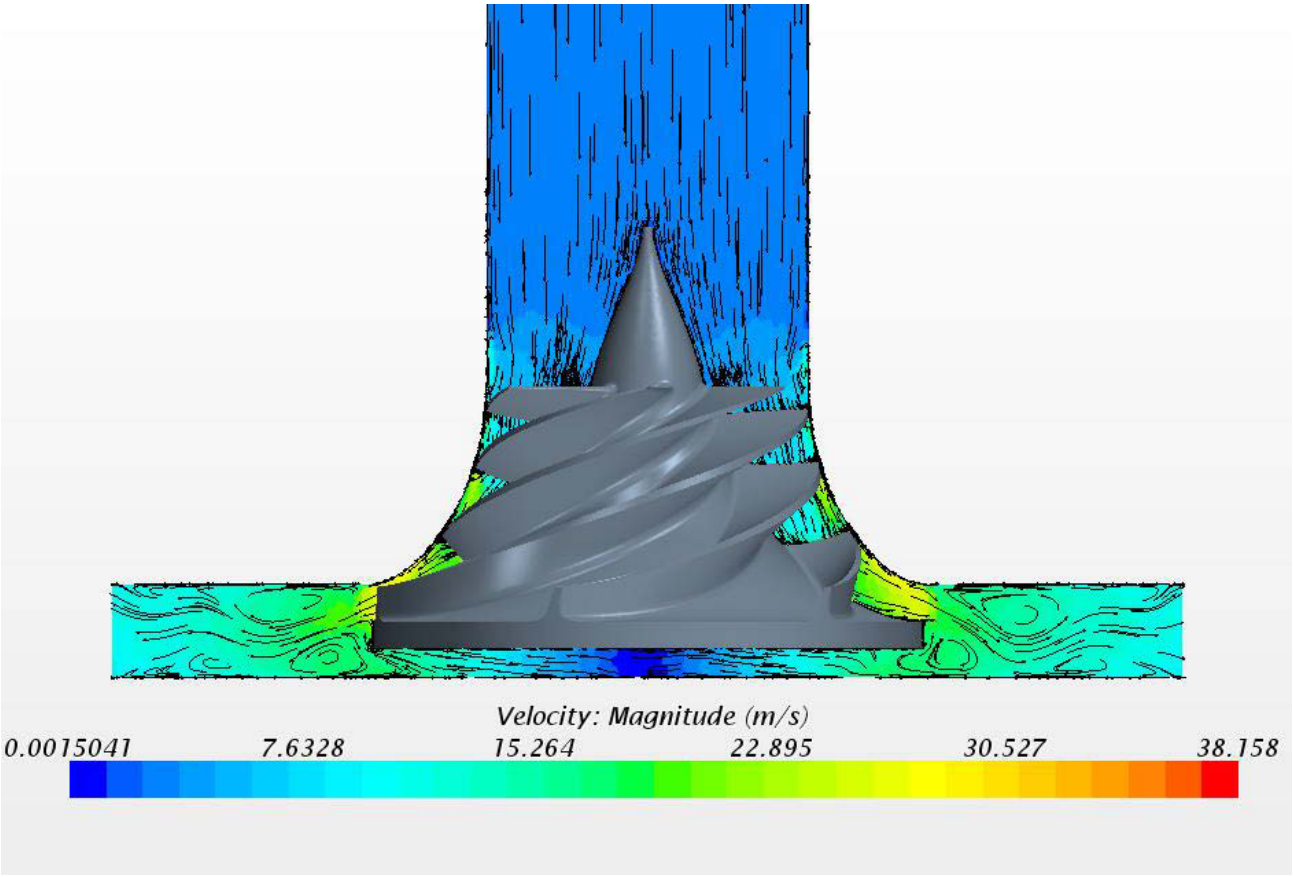

Figure 3.20: A 2D slice showing 3D streamlines through the system with the impeller superimposed in 3D form

3.6 Cavitation Model Development

To model cavitation certain parameters of the CFD model needed to be altered. Firstly the flow model had to be changed from a simple liquid to a multiphase flow model, namely invoking the Volume of Fluid model which was discussed in more detail in Chapter 1.

The model for "time" also had to be changed from steady to implicit unsteady to allow the cavitation model to be used correctly. A new motion was also introduced, rigid body motion, which physically rotates the impeller region rather than applying a rotating reference frame to the region. The rigid body motion model takes into account all the transient flow characteristics and allows a smooth transition between components (Zhu & Chen, 2012). This motion model can also only be used with an unsteady time model.

Using the implicit unsteady time model requires various new parameters to be set for the numerical model such as time step values, physical run time and the number of inner iterations. These parameters are related to the robustness of the model. The time step chosen for an unsteady model is vital as it depicts the distance travelled by the mesh between calculations. If the time step is too large,

the mesh will be displaced too much and the solution being transferred between cells will be inaccurate. However, if the time step is too small, the simulation will be extremely computationally expensive. The time step is related to the convective Courant number which offers a method of checking the validity of the chosen time step. The convective Courant number is the ratio of the physical time step to the mesh convection time scale. For time-accurate simulations the convective Courant number should be approximately 1 which means that the fluid moves roughly 1 cell for every time step. This provides a good indication of whether or not the time step is appropriate. A good time step for rotation results in 1 degree of rotation per time step, while the physical time for the solution should allow for at least three rotations of the solid body (CD-Adapco, 2013). Using these guidelines the time step was calculated as follows:

$$5000\ rpm = 0.012\ s/rev$$

$$\frac{0.012}{360} = 3.33 \times 10^{-5} s$$

This meant that a time step of $3.33 \times 10^{-5} s$ would allow one degree of rotation per time step. Once this value was used the convective Courant number was viewed in a scalar scene which can be seen in figure 3.21 The scene showed that the values were less than 1 which meant the time step was suitable for the given mesh and rotational speed.

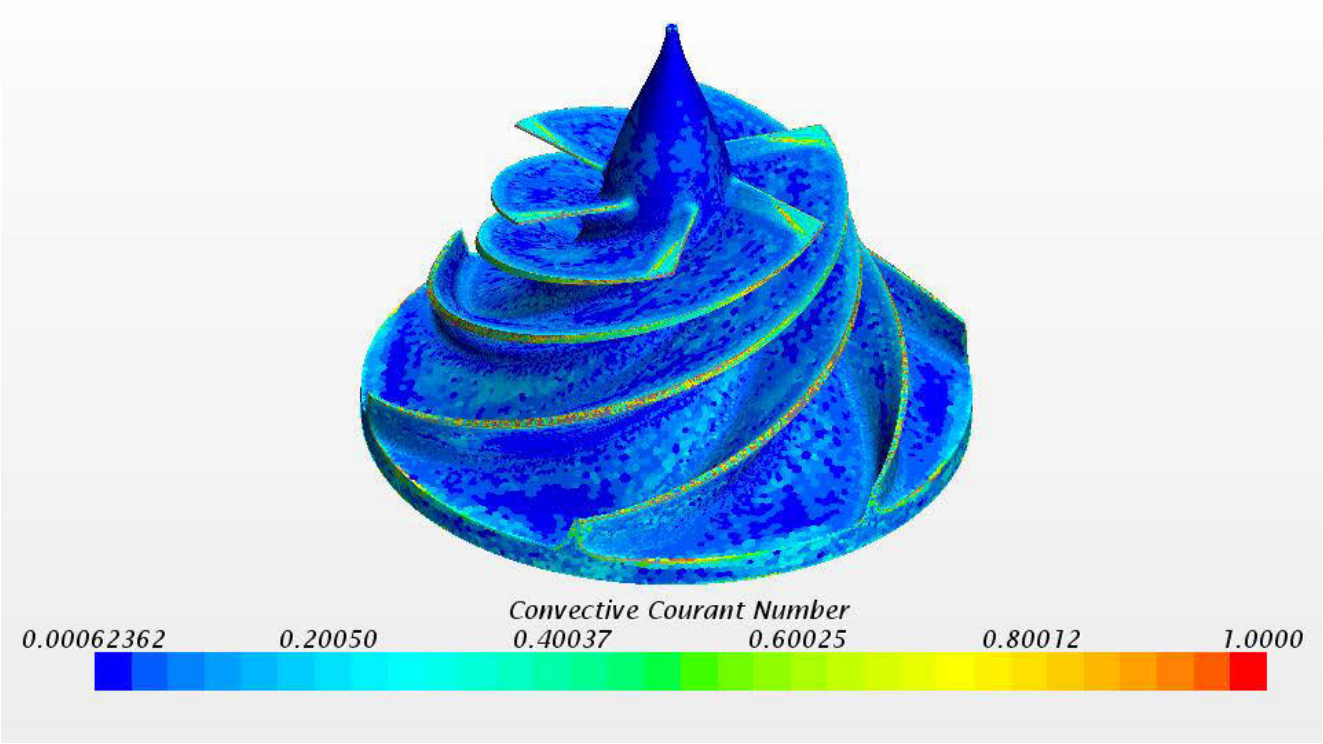

Figure 3.21: Convective Courant number

As already stated there was another new factor to be determined, the number of inner iterations, which prescribed the number of iterations that are carried out for each time step. The number of inner iterations determines the convergence of each time step. If the number of inner iterations is too low, the simulation would not converge. However, too many inner iterations and the simulations would be too computationally expensive. The default number of inner iterations is 5 which was deemed too low. The number of inner iterations was set to 10 after it was found that the simulation did not converge with only 5 iterations per time step.

New boundary conditions were also implemented with regards to the volume fraction of fluid. The inlet and outlet of the model were set to have only liquid flowing through them. This ensured that no vapour was present at the inlet nor at the outlet thus implying that any vapour present in the system was the result of low pressure zones and was indeed cavitation. These boundary conditions also ensured that any cavitation vapour formed on the rotor had condensed before leaving the system. This was done by setting the volume fraction of liquid water to 1 and the vapour fraction to 0 at these boundaries, implying that no vapour bubbles entered or left the model. The same procedure was followed for the initialization of the solution where initial conditions were set for the volume fraction of fluid. The vapour pressure of the fluid was already known within the software as water is a popular fluid medium. The default of 400 Pa was used as the vapour pressure because the temperature of the

fluid matched the default temperature set by the software. In other words the vapour pressure of the fluid matched the default set by the software so no change was required.

3.7 Cavitation Model Results

The cavitation model was run for the final mesh only and at the operating flow rate due to the high computational cost of the transient simulation. Naturally the residuals of the transient simulation look different to the steady state residuals as the mesh is moving every 10 iterations which causes a jump in residuals. This meant that the residuals could not be used as a convergence check, however if they had increased endlessly there would have been an issue. However, the residuals did provide a small insight into the intra time step convergence. During each time step the residuals decreased sufficiently (more than one order of magnitude) for the 10 inner iterations before increasing as the simulation changes to the next time step.

The pressure plot (figure 3.22) of the simulation can be seen below where the outlet pressure is relatively stable for a transient cavitating solution. The outlet pressure shows negligible change with the introduction of the cavitation model which suggests minimal cavitation formation. This is supported by the scalar scene of the volume fraction around the impeller where only a small portion of the flow on the impeller shows cavitation. The cavitation is formed on the leading edge of the impeller blades and dissipates quickly. The outer edge of the leading edge appears to produce a greater portion of cavitation due to the higher linear speed of the edge of the blade. It is also notable that the area of cavitating flow in figure 3.23 corresponds to the small area on the impeller where the pressure was below the vapour pressure in the steady state simulations.

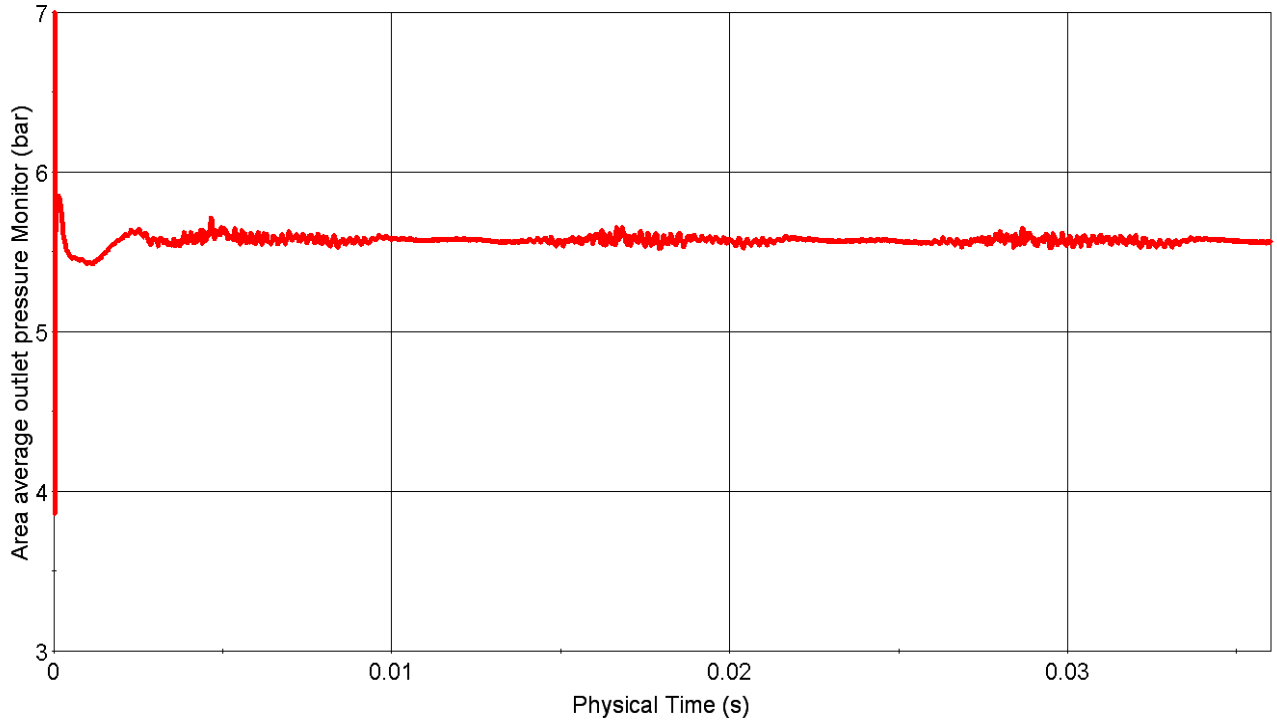

Figure 3.22: Cavitation model static pressure at impeller outlet

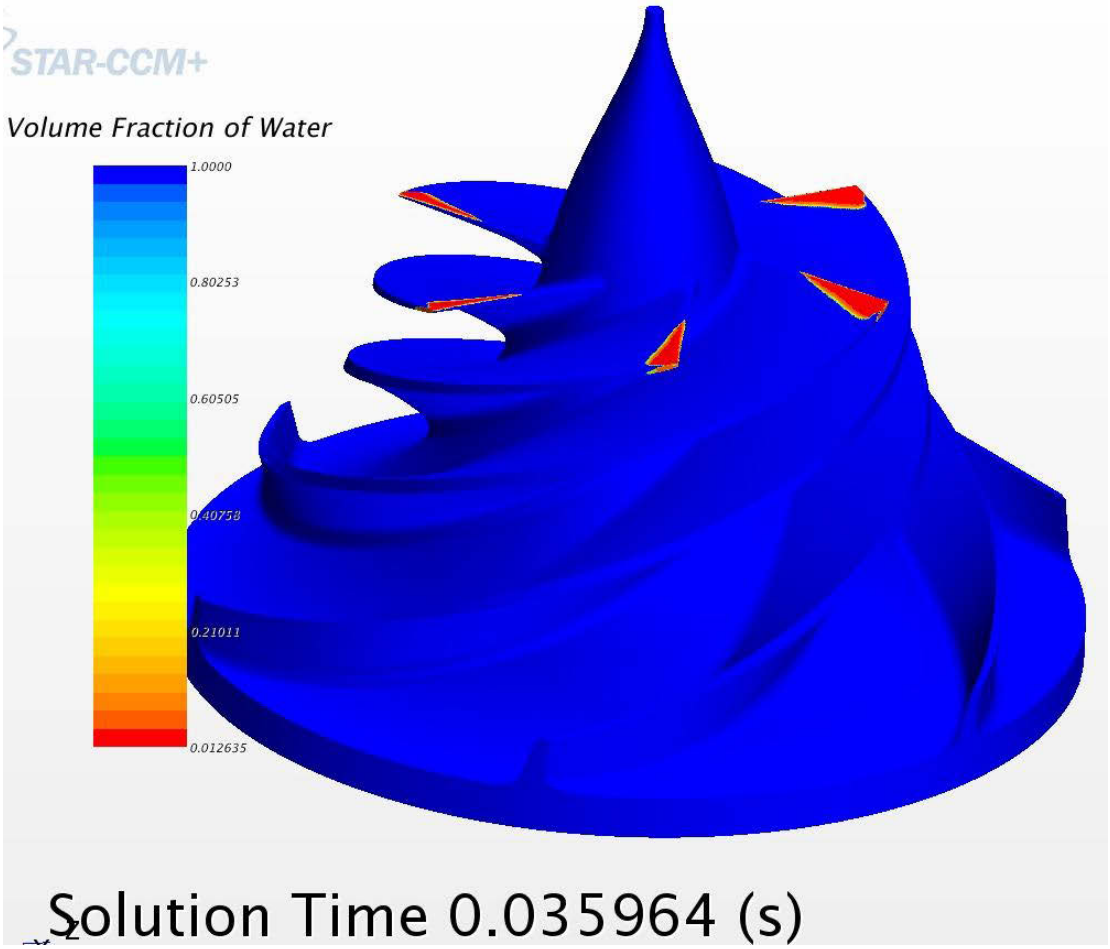

Figure 3.23: Volume fraction of water vapour indicating two phase flow

Figure 3.24 shows an ISO surface where the volume fraction of water is 0.9 meaning that the surface indicates an area where the water vapour makes up over 10% of the volume fraction. The figure confirms that the water vapour generates on the leading edge of the blade, similar to leading edge cavitation discussed in the literature review of section 2.5.1.

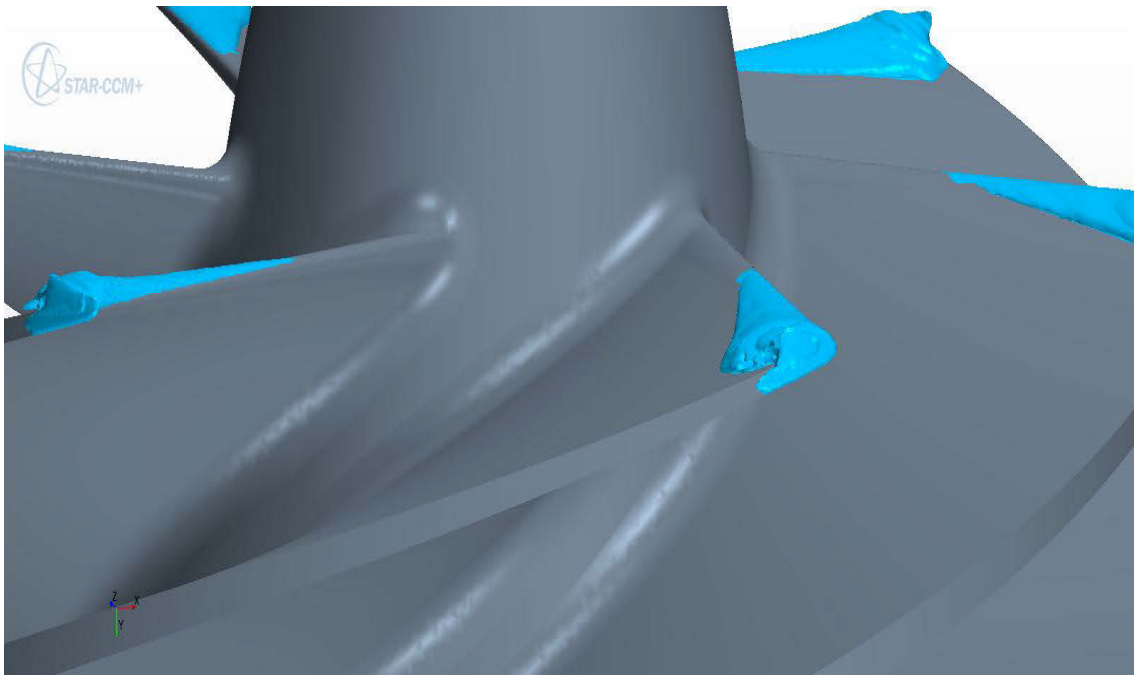

Figure 3.24: ISO surface where the volume fraction of water is 0.9

The above results indicate that while the numerical model struggles to predict the head drop that is a characteristic of pump curves at high flow rates, there is still a good agreement between the two sets of results at the operating point. The cavitation prediction shows a small fraction of the flow exhibiting signs of two phase flow. This is known as incipient cavitation where it can be assumed that the very limited degree of cavitation development does not have a significant effect on the pump performance (Franc, 2006). The cavitation in this model is generated by the leading edge of the blade as expected. The area of cavitating flow also corresponds with the low pressure zones of the steady simulations which provide a degree of confidence in the results. Due to the low level of cavitation the pressure at the outlet has not decreased significantly in the presence of the two phase flow. The experimental data, once obtained, will provide verification of the Rayleigh-Plesset equation and the two phase flow model within Star CCM+. This however requires difficult modifications to the inlet section of the pump casing where a viewing window is needed in the pipeline to visually assess the cavitation production. Without the viewing window, it will be difficult to confirm the area in which the cavitation is occurring as well as how far the cavitation vapour bubbles travel down the rotor blade passages.

4 Full sized impeller

The following chapter deals with the model development for the full size impeller. This CFD model was developed in the same manner as the first CFD model. However there are several major differences between the two models which are discussed below. After the model set up is described the results are presented and discussed.

4.1 Introduction

A similar approach was taken to that discussed in Chapter 3 when modelling the full sized impeller. One major difference was the fluid being modelled. Only the scaled impeller could be tested in a laboratory since the 1MW required for the full size rotor was unattainable. The full sized impeller however was modelled to predict how the pump would perform pumping kerosene; a situation appropriate to its role in the propulsion system required to transport a payload into orbit.

Another notable difference, which added considerably to the computational cost of the full size model was the speed ramping that took place. Unlike the scaled model, the full size model could not simply have the operating speed (14500 rpm) set from the beginning. This resulted in a crash of the system as it is unrealistic for a real pump to make the jump from zero to 14500 rpm instantly. Rather, the simulation was started at a lower speed (4500rpm). Once the simulation had reached a steady state, the speed was ramped up to 7250rpm. This process was repeated until the full speed was achieved. The flow rates were then altered to generate a pump curve for the operating speed.

The CAD model was prepared in the same way as the scaled impeller, also with a tip gap of 0.5 mm. The impeller geometry can be seen in figure 4.1. The computational domain was also the same for the full size impeller where there were three regions, the inlet, the rotating region and the outlet. As before, the volute was not modelled and the pressure values at outlet were measured on a cylindrical plane situated at the impeller exit.

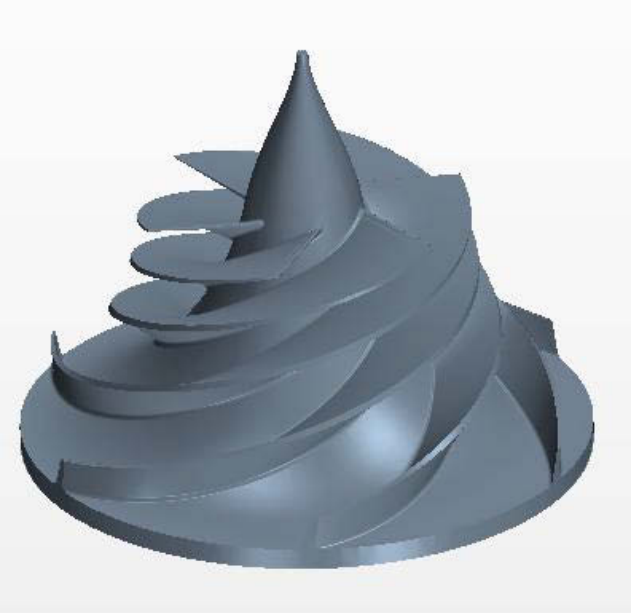

Figure 4.1: Full size impeller geometry

4.2 Mesh Generation

The approach to meshing the full size impeller was the same as the approach taken in the scaled impeller. The process was shortened as the base line mesh for the model had been defined with the scaled impeller. Again a polyhedral mesh was used with prism layers lining the walls of the model.

After each mesh had been successfully generated, the model was run at flow rates determined by the meanline data provided by Smyth (2013) which is provided in Table 4.1. Naturally the key data points were at the full speed (14500 rpm) since the flow rates and pressures required by the combustion of the propulsion system were specified at this speed. The other points were simply used to ramp the system up and prevent the divergence of the solution. After each run the results were analysed and the mesh was improved.

Table 4.1: Meanline data points for full size simulations

Mass flow rate (kg/s)	20.65	30.985	72.30	87.8	103.29	118.78	134.27
Speed (rpm)	7250	10875	14500	14500	14500	14500	14500

Having already meshed the scaled impeller it was known that certain areas needed special attention in the form of volumetric controls. However, the first full scale CFD model was meshed and run without the refinement of the tip gap region and the gap therefore only had 2 polyhedral cells in place

(compared to 14 for the scaled model) to capture the character of the flow. This allowed the effect of the mesh in this region to be noted in later mesh configurations. The first mesh that was generated for the full size impeller was defined in terms of the general values and values in the areas that required additional refinement:

Table 4.2: Initial mesh characteristics

General Values		Base size (mm)	5
		Minimum surface size (mm)	1.25
		Absolute surface size (mm)	5
		Prism layer number	12
		Prism layer thickness (mm)	2
Refined Areas	Tip Gap	Number of cells	2
	Blade	Leading edge (mm)	0.2
		Minimum surface size (mm)	0.5
		Absolute surface size (mm)	2
	Hub	Minimum surface size (mm)	1
		Absolute surface size (mm)	2
Total Number of Cells			4 018 237

The measured output for the mesh study was the static pressure at the outlet plane of the impeller. The results of the mesh independence study can be seen in table 4.3 where the percentage difference of outlet pressure from one mesh to the next is given. The results can also be seen in figure 4.2 which shows a graph of each set of results. Both the table and the figure show that all four mesh configurations have similar results, the largest difference is 2.92% between the first and second mesh at the maximum flow rate of 134.27 kg/s. Despite the low percentage difference between early mesh configurations, efforts to optimise the modelling of the flow in the tip region continued.

Table 4.3: Results of mesh independent study for the full size impeller

Flow rate (kg/s)	Difference between 1 and 2	Difference between 2 and 3	Difference between 3 and 4
72.3	0.27%	0.11%	1.24%
87.8	1.02%	0.33%	1.59%
103.29	1.76%	0.21%	1.15%
118.78	2.34%	0.35%	0.57%
134.27	2.92%	0.53%	0.04%

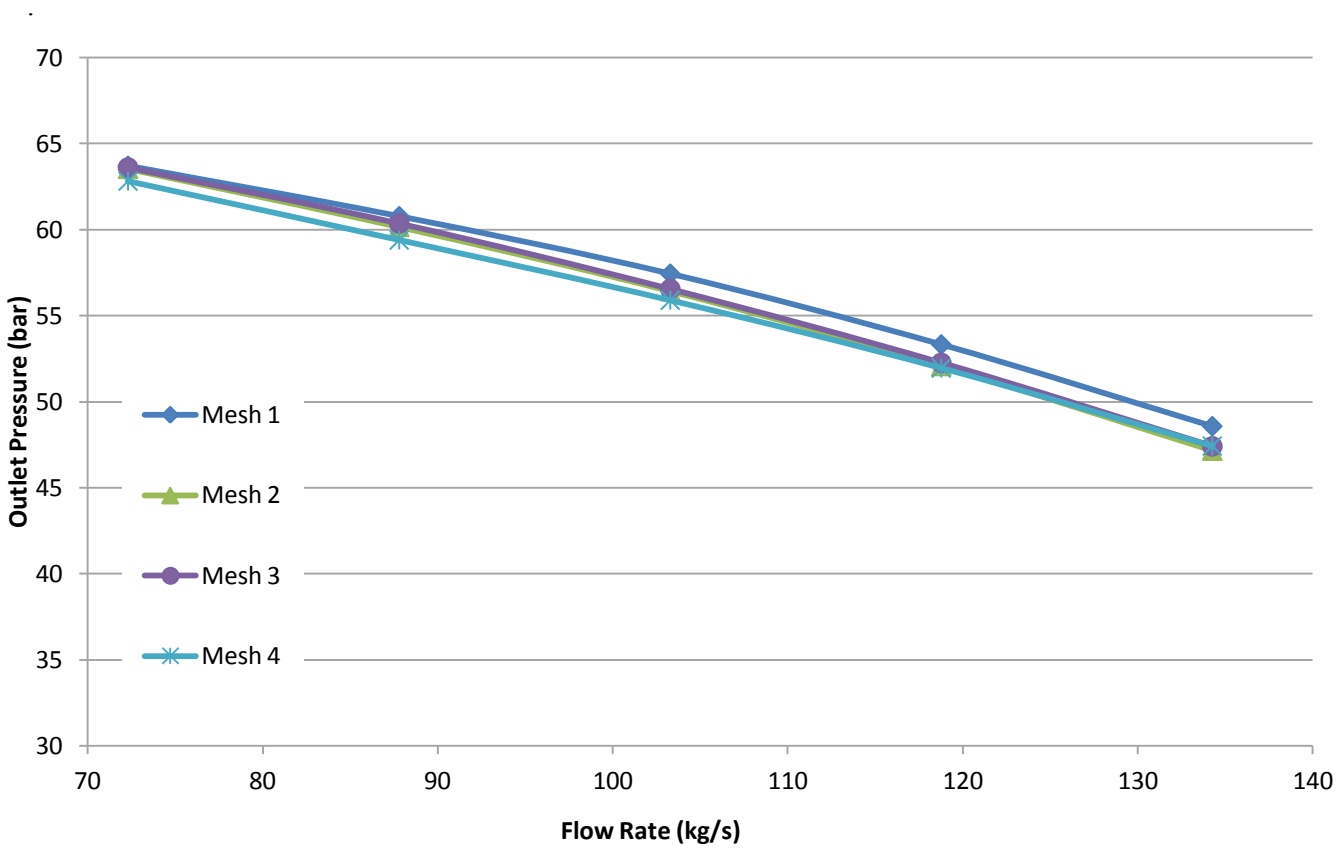

Figure 4.2: Graph showing the pump curve for each mesh of the full size impeller

The mesh optimisation process was not as stringent as the refinement for the scaled model. The scaled model showed that the results did not reveal any significant changes when the Y+ value was decreased to 1. Therefore the wall Y+ aim for the full size model was not as low as 1. Rather, the goal Y+ value for the full model was approximately 3, which is still an acceptably low value.

The second mesh introduced a volumetric control into the tip gap but only polyhedral cells were used to define this region. This resulted in 5 polyhedral cells in the tip gap for the second mesh (0.1 mm cell size). 12 prism layers were used in the remainder of the model, with an overall thickness of 2 mm, yielding a Y+ value of approximately 10 on the impeller surface.

The third mesh increased the number of prism layers from 12 to 15, in turn reducing the Y+ to 2.5 (figure 4.3). This was deemed acceptable for a final value.

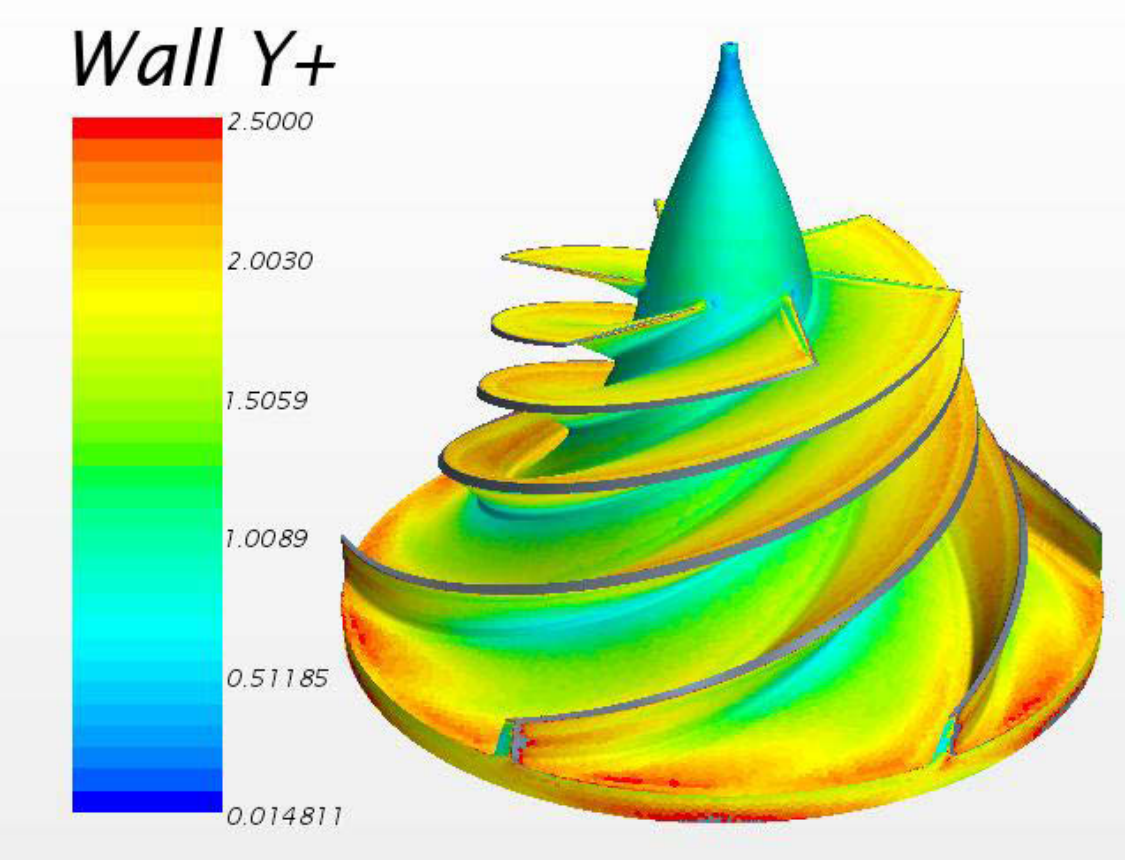

Figure 4.3: Wall Y+ of the full scale model

The fourth mesh introduced the prism layers into the tip gap by increasing the gap fill percentage to 45% and reducing the minimum thickness percentage to 4%. The general polyhedral cell size was 0.1 mm with 3 prism layers on each wall (the blade and shroud wall) resulting in 9 cells in the tip gap as seen in figure 4.4. Since increasing the number of cells in the clearance gap showed no significant change in the result for the scaled model, the configuration of 9 cells in the gap was left as the final optimisation.

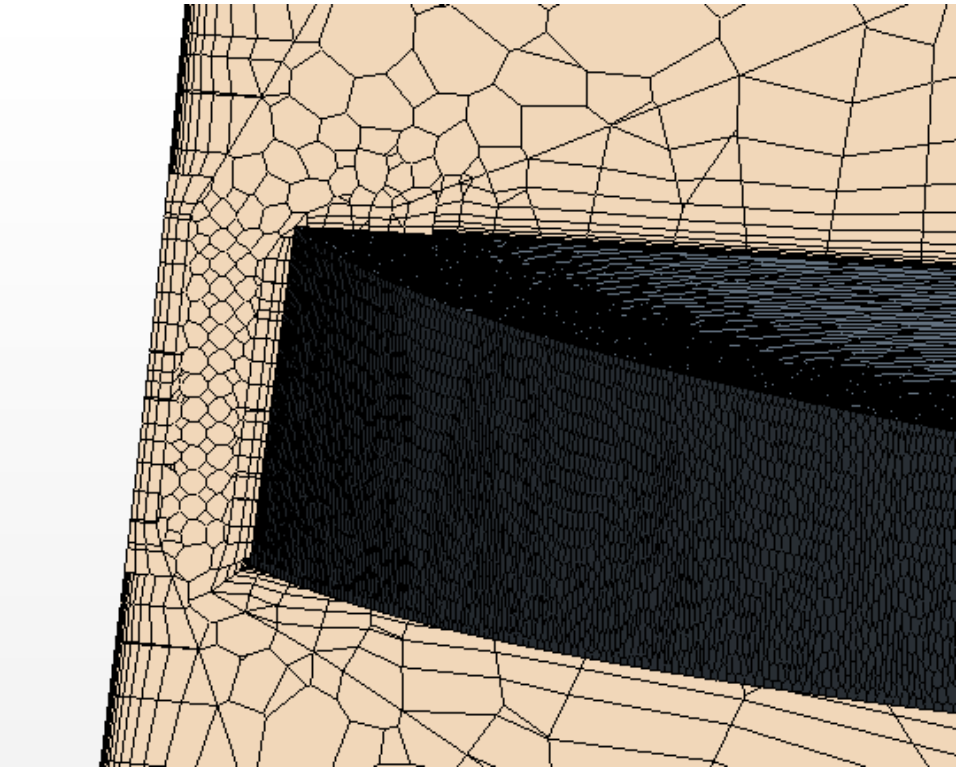

Figure 4.4: Tip gap mesh

The final mesh had the following characteristics and can be seen in its entirety in figure 4.5:

Table 4.4: Final mesh characteristics for the full size impeller

General Values		Base size (mm)	5
		Minimum surface size (mm)	1.25
		Absolute surface size (mm)	5
		Prism layer number	15
		Prism layer thickness (mm)	2
Refined Areas	Tip Gap	Base size (mm)	0.1
		Prism layer number	3
		Prism layer thickness (mm)	0.1
		Number of Cells	9
	Blade	Leading edge (mm)	0.2
		Minimum surface size (mm)	0.5
		Absolute surface size (mm)	2
	Hub	Minimum surface size (mm)	1
		Absolute surface size (mm)	2
Total Number of Cells			11 610 068

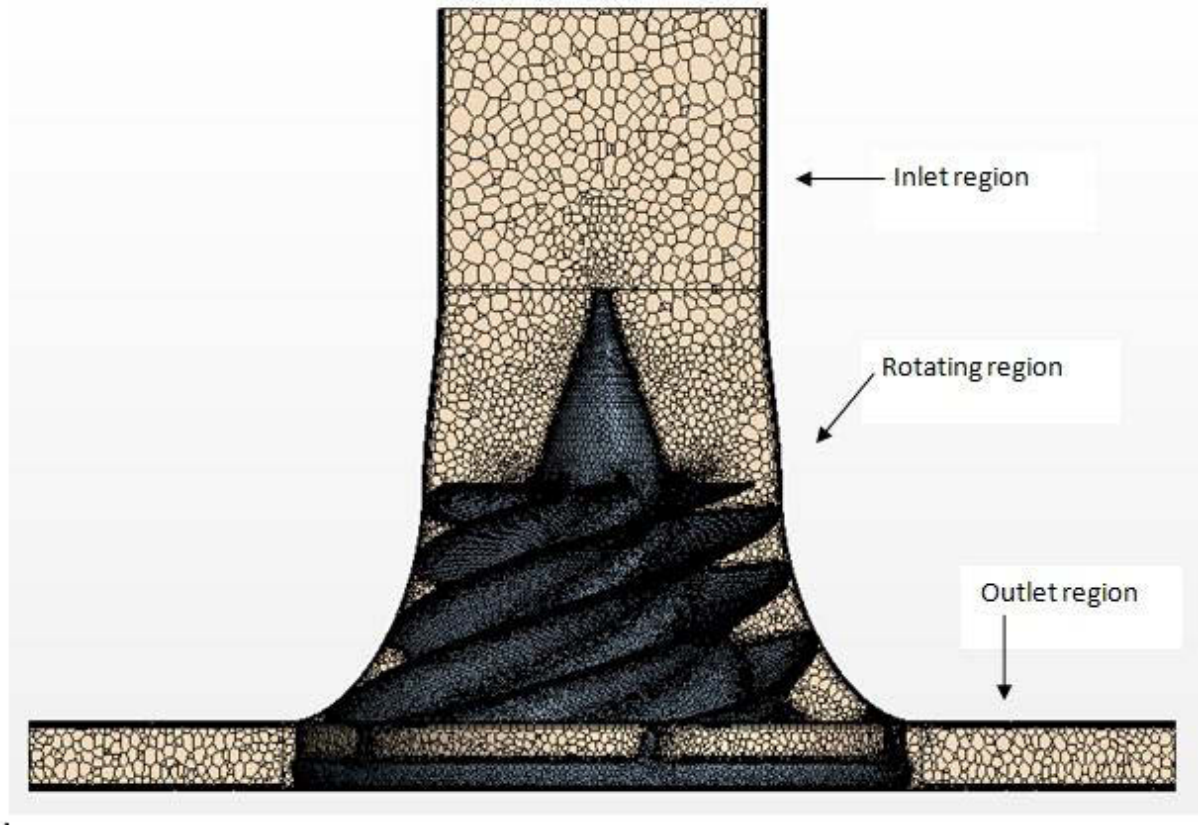

Figure 4.5: Final mesh distribution for the full size impeller

The cell relative velocity can be seen in figure 4.6 which depicts an acceptable mesh distribution since there are no rapid changes in velocity between cells. In other words the mesh sizing is appropriate for a smooth transition of velocity from one cell to the next. There are no discontinuities or jumps in velocity.

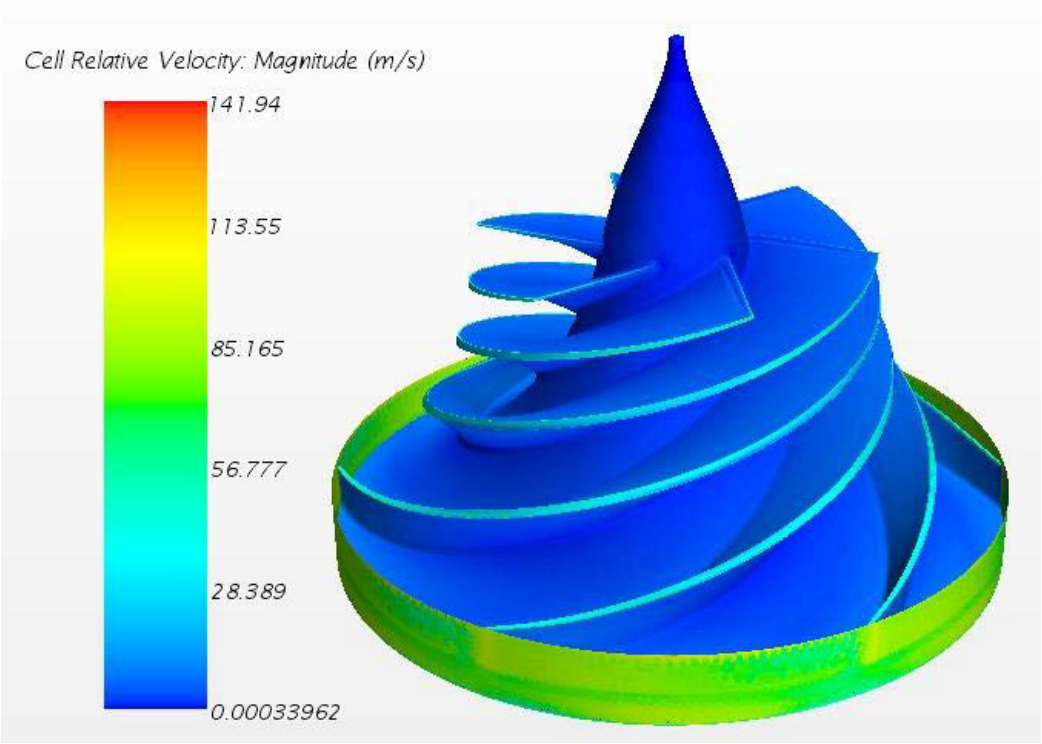

Figure 4.6: Cell relative velocity of the full scale impeller

4.3 Model Development

The majority of the physics models were the same for both the full size and scaled impellers. The boundary conditions used consisted of a stagnation inlet where the temperature and total pressure were defined. The outlet boundary condition was a mass flow outlet which was varied according to the meanline data points seen in table 4.5 and were defined by Smyth (2013). Table 4.5 also contains the inlet characteristics defined by the total temperature and total temperature.

Table 4.5: Boundary conditions and parameters for full size model

Parameters	Mass Flow rate (kg/s)	20.65	30.985	72.30	87.80	103.29	118.78	134.27
	Speed (rpm)	7250	10875	14500	14500	14500	14500	14500
Stagnation Inlet	Pressure (bar)	3.49	3.49	3.49	3.49	3.49	3.49	3.49
	Temperature (K)	300	300	300	300	300	300	300

Despite the similarities, there were two major differences in the model set up. The first change was the speed ramping which has already been discussed. The second change was the fluid being used. The original design work of Smyth (2013) used Kerosene RP-1 fuel. The database that Star CCM+

offers for different fluids does not contain this fuel. However, it does list Jet A fuel which has very similar properties. One of the differences, by 2%, was the density. This was consequently reset manually to 819 kg/m^3, to match the data as defined by the meanline data.

4.4 Steady State Results

The pressure outlet of the impeller was measured in the same manner as the scaled model where the surface area average was taken on a cylindrical plane placed at the impeller outlet. Due to the speed ramping, the computational cost of the full size model was far greater than the scaled model. Each different speed or flow rate was run for 1000 iterations once the model had reached the operating speed of 14500 rpm. This meant that it took 5000 iterations to obtain results for the operating point (103.29 kg/s at 14500 rpm). Figure 4.7 shows the time per iteration for the full scale model. The time can be seen to be roughly 30 seconds per iteration, resulting in a total run time of just less than 42 hours to obtain results for the operating point. A further 2000 iterations was required to obtain a full pump curve (1000 iterations for each flow rate above the operating point). A full pump curve now taking 58 hours, is seen as clear support for reducing the extent to which the tip gap is defined. The computational cost of the model was already significantly high at 42 hours, so further mesh optimisations that had proven inefficient in the scaled model (Chapter 3.3) were discarded by the author.

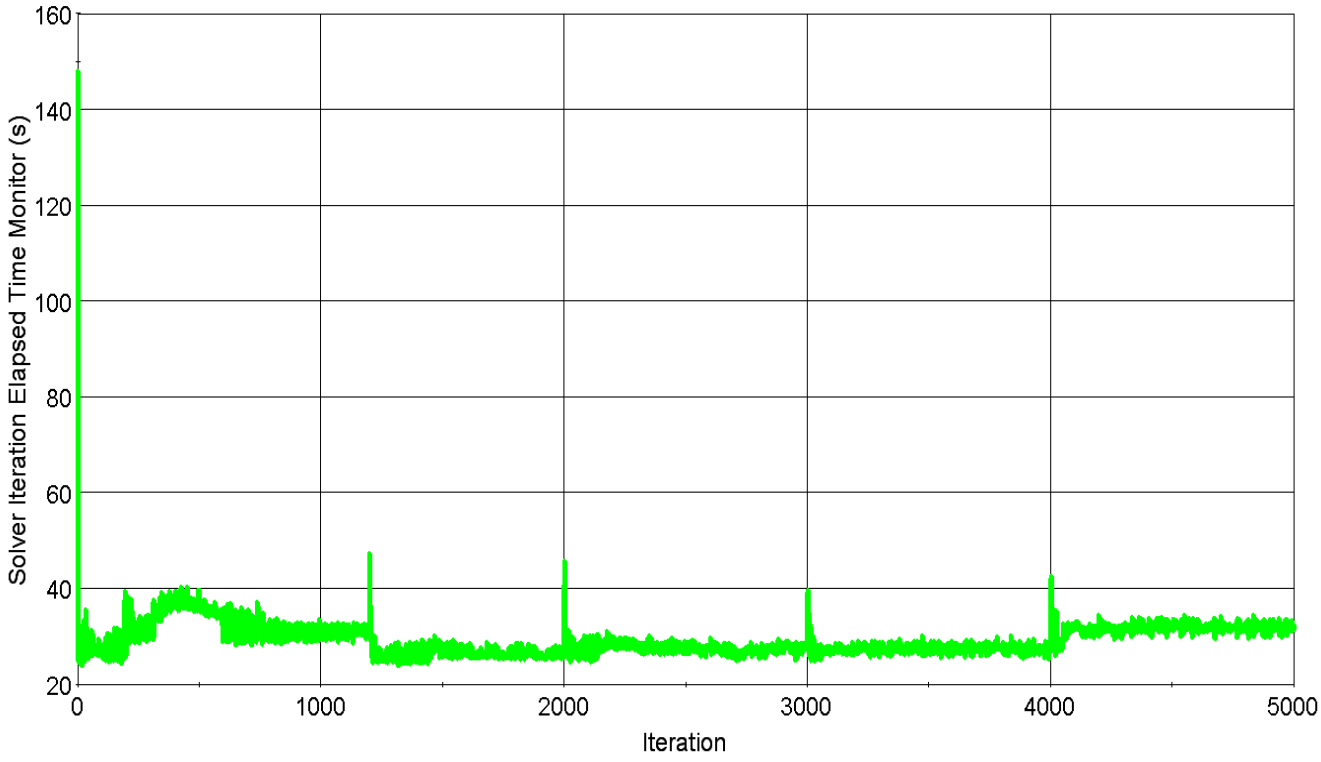

Figure 4.7: Elapsed time plot

To ensure convergence of the full model, the pressure plot was monitored for each stage of the speed ramping and can be seen in figure 4.8. The first section of the plot does not last long as the conditions used for that portion were below the conditions prescribed by the meanline data and were merely used to prevent divergence when starting with the meanline data points. After that section each flow rate was run for approximately 1000 iterations. The operating speed begins at iteration 2000 with the operating point beginning at iteration 4000. The graph shows the convergence for each data set through the stability of the graph before the change in variables occurs.

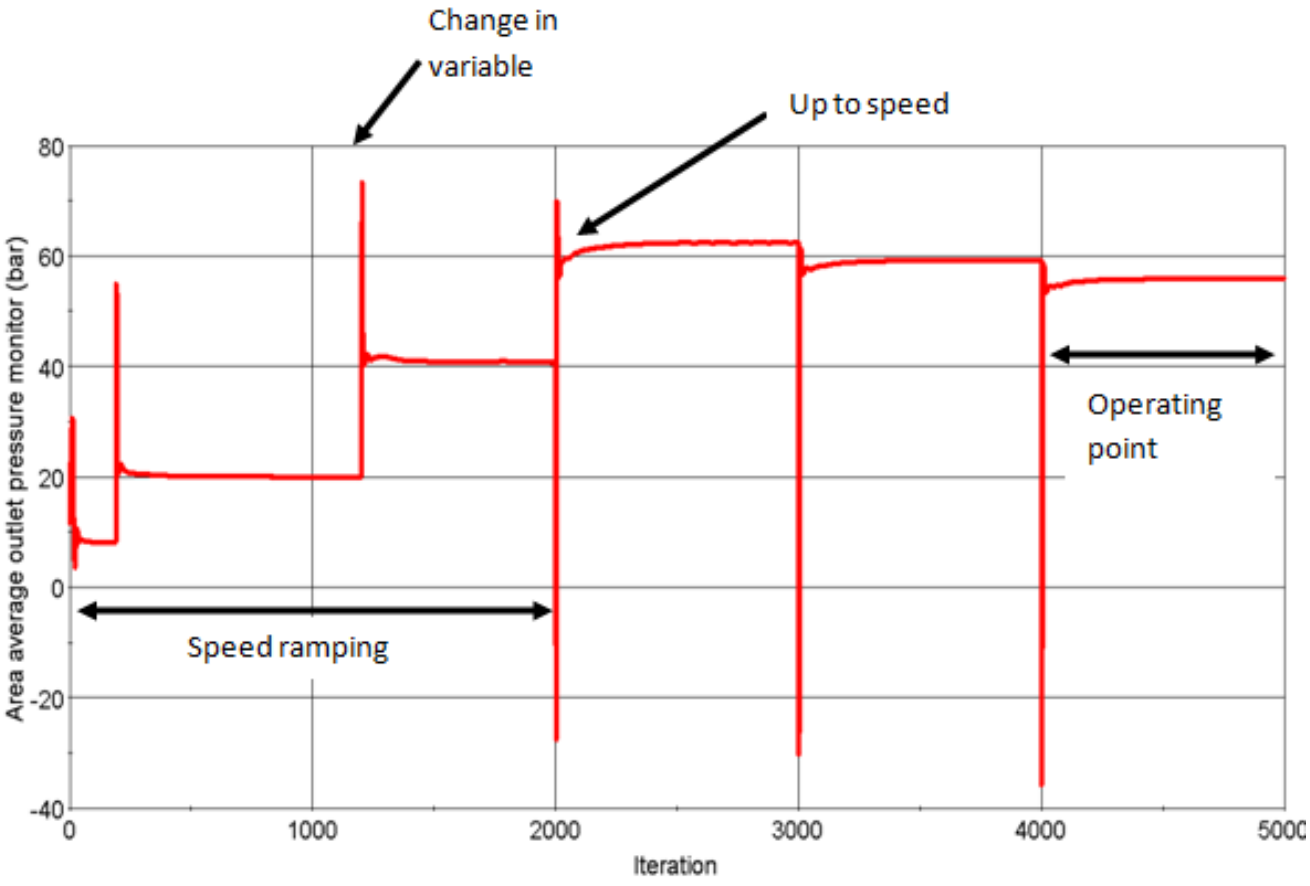

Figure 4.8: Outlet pressure results of the full scale model

The time-steady results show exceptional correlation between the numerical predictions and the meanline data. The comparison between the two sets of results can be seen in table 4.6 and figure 4.9 where the table includes the data points of the two low speeds used to ramp the model. Unlike the scaled impeller, the full size model under-predicts the head rise at lower flow rates. Then, at higher flow rates, the head rise is over-predicted by the CFD model. As with the scaled model, the meanline analysis captures the decrease in outlet pressure better than the numerical predictions. The full size model captures the head drop off better than the scaled model but is still high relative to the meanline data.

The greatest deviation from the meanline results is 8.56% at the largest flow rate used (134.27 kg/s). At the operating point the two sets of results are in good agreement with only a 1.31% difference. Using the same method of average differencing used by Shojaeefard, et al. (2012) the average difference percentage at the operating speed is 5.18%.

Table 4.6 Final steady state results for the full size impeller

11 610 068 cells						
Parameters		**Stagnation Inlet**		**Outlet Pressure (bar)**		**Difference**
Mass Flow rate (kg/s)	Speed (rpm)	Pressure (bar)	Temperature (K)	Meanline	CFD	Difference
20.65	7250	3.498	300	21.1	20.18	4.56%
30.985	10875	3.498	300	43.77	41.12	6.44%
72.3	14500	3.498	300	66.82	62.82	6.37%
87.8	14500	3.498	300	62.59	59.4	5.37%
103.29	14500	3.498	300	56.63	55.9	1.31%
118.78	14500	3.498	300	49.73	51.96	4.29%
134.27	14500	3.498	300	43.37	47.43	8.56%

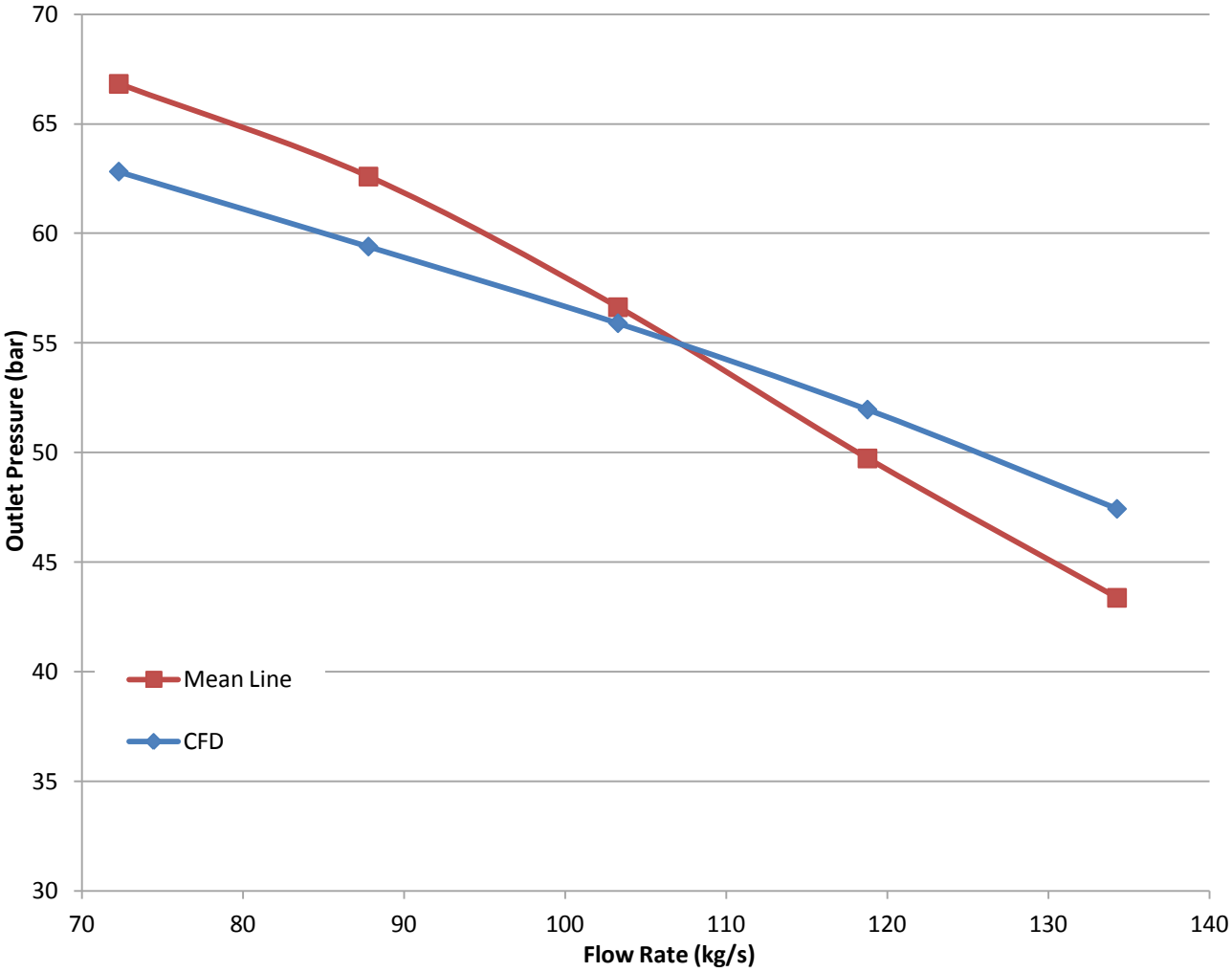

Figure 4.9: Graphical comparison of the steady state results for the full scale impeller

4.5 Cavitation Model Development

The transient analysis required the use of rigid body motion, the volume of fluid model, as well as the implicit unsteady time model. The cavitation model used for the full size impeller saw two fundamental changes from the scaled model. The first important change was the fluid, which was also prescribed in the steady state model. However, the saturated vapour pressure needed to be prescribed for the transient analysis. There are various different grades of Kerosene, as discussed earlier, and specific data such as the saturation pressure is difficult to obtain. The saturated vapour pressure however, was found to be 364 Pa, almost one tenth that of water.

The second change was the time step value. Since the full size impeller has a much faster rotational speed the time step needed to be decreased. The aim for the time step value was 1^{o} of rotation per time step and the calculation can be seen below. This yielded a time step of $1.15 \times 10^{-5} s$ and the second

order temporal discretisation was employed for increased accuracy. The physical time for the simulation was originally set to 0.0166 s to allow for 4 full rotations of the impeller but was increased to 0.0207 s to include a fifth rotation as the pressure value was otherwise unstable. The number of inner iterations was also set to 10 to allow convergence within each time step. The convective Courant number was checked and figure 4.10 shows the value to be less than 1 on the impeller surface which indicates an acceptable mesh for transient analysis.

$$14500\ rpm = 0.00413\ \ s/rev$$

$$\frac{0.00413}{360} = 1.15 \times 10^{-5} s$$

As with the scaled model, the full size model prescribed the volume fraction of liquid and vapour at the inlet and outlet boundaries. Naturally the volume fraction of Kerosene liquid was set to 1 at both of the aforementioned boundaries as well as within the model as an initial condition. In other words it was assumed that at start-up, there was no vapour present in the flow.

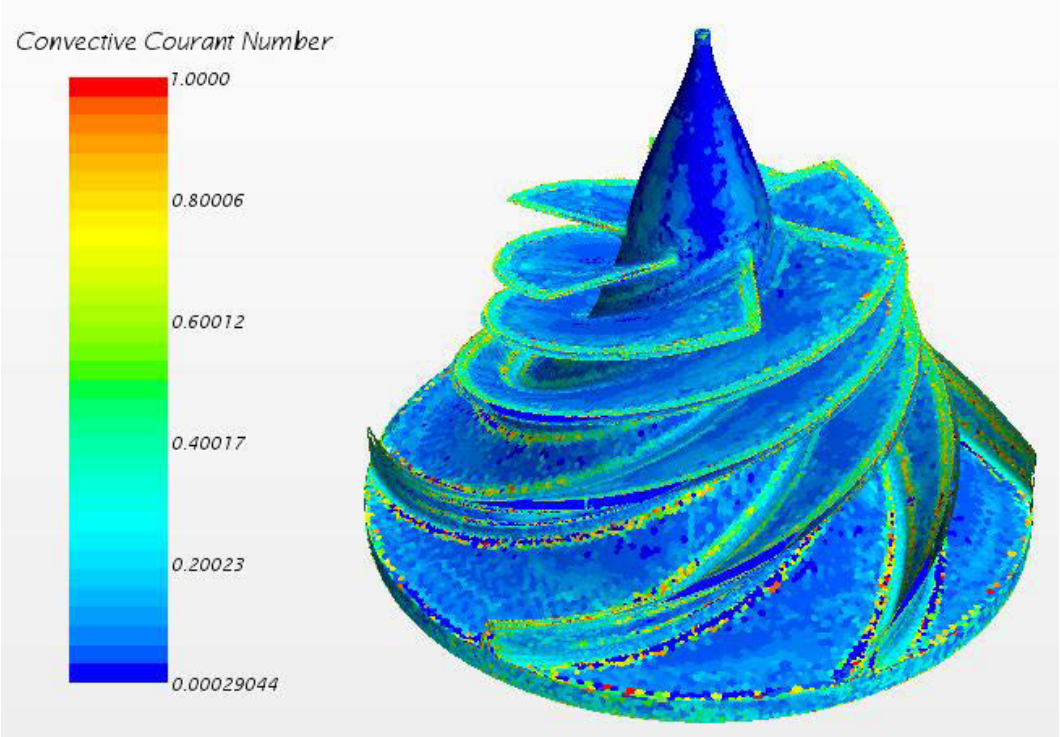

Figure 4.10: Convective Courant number associated with the full scale model

4.6 Cavitation Model Results

The cavitation results of the full size impeller had a greater impact on the impeller performance than in the scaled model (Section 3.7). As before, the residuals were observed as a check for the convergence of each time step. The pressure plot however (figure 4.11), took longer than anticipated

to stabilise which meant the physical time of the model was extended to include a fifth rotation of the impeller. Although the pressure plot did not stabilise completely, the oscillations of the plot were reducing and an average of roughly 45 b can be seen for the pressure value.

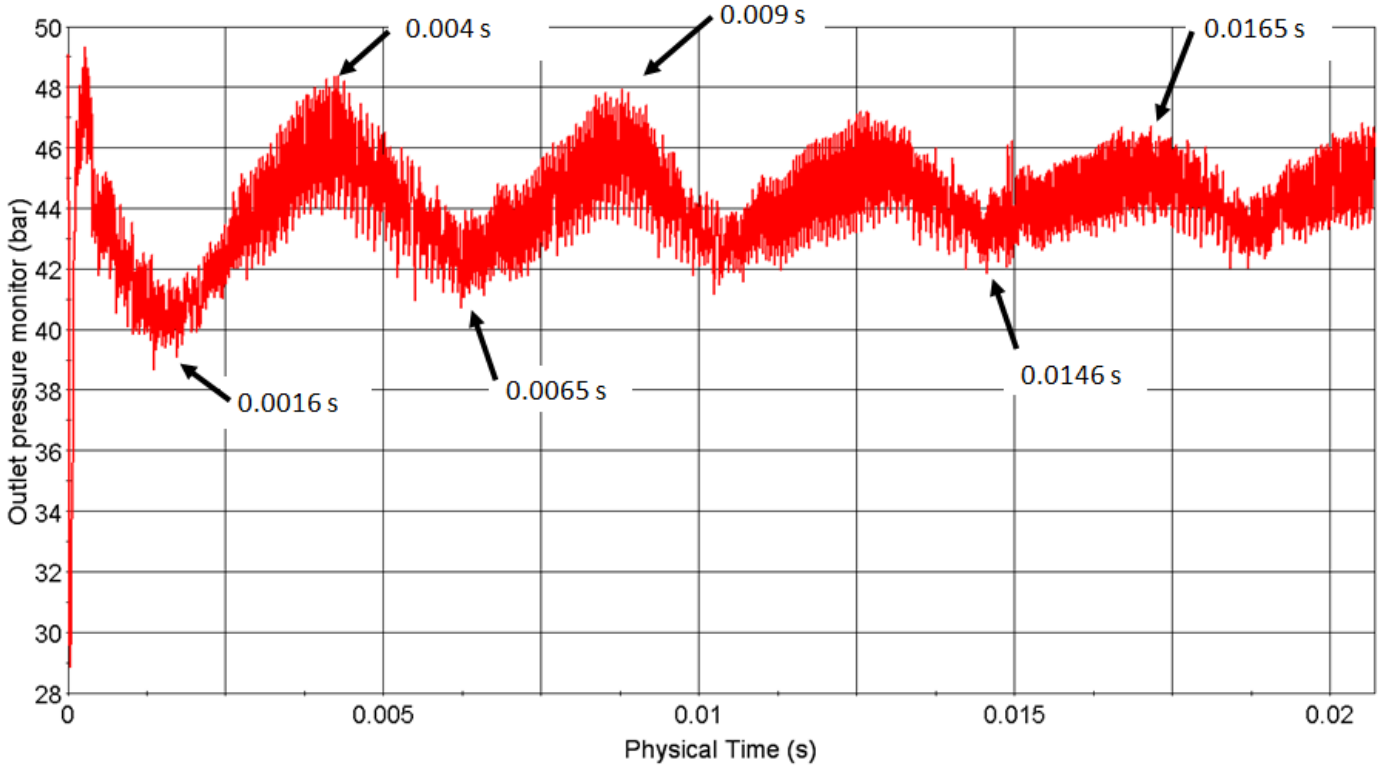

Figure 4.11: Static pressure outlet plot

The oscillations seen in the pressure plot are related to the cavitation and the flow blockage that the cavitation causes. This can be seen in the figures below which shows the presence of two phase flow at times which correspond to the troughs and peaks of the pressure plot. The presence of the two phase flow is shown through the use of a threshold that was generated where the volume fraction of liquid kerosene was less than 0.9. The first comparison of the amount of two phase flow corresponds to the first major trough and peak pairing (the initial peak has been neglected since it occurs very early on in the simulation). The first trough and peak take place, according to the pressure plot above, at approximately 0.0016 s and 0.004 s respectively. Figure 4.12 (a) shows a greater presence of two phase flow which explains the decrease in pressure at 0.0016 s. Figure 4.12 (b) shows a much smaller level of two phase flow and hence the pressure outlet was peaking at this time.

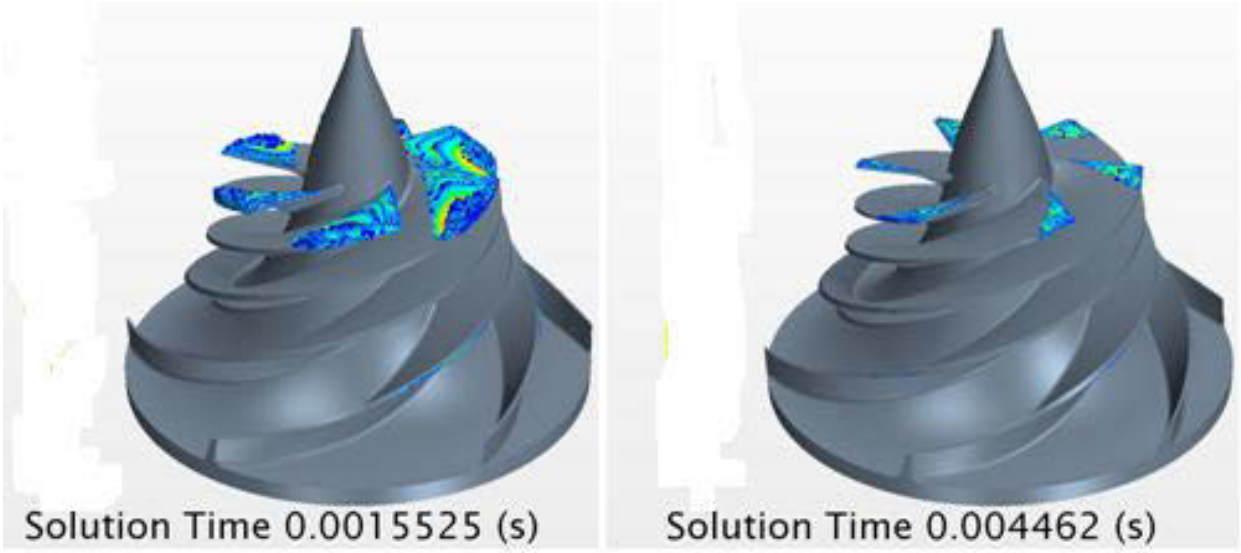

Figure 4.12: Presence of two phase flow at a) 0.0015525 s and b) 0.004462 s

The second oscillation shows similar results where the two phase flow is greater during the trough period at 0.0065 s. As the pressure peaks, the cavitation levels decrease which is depicted by figure 4.13 (b).

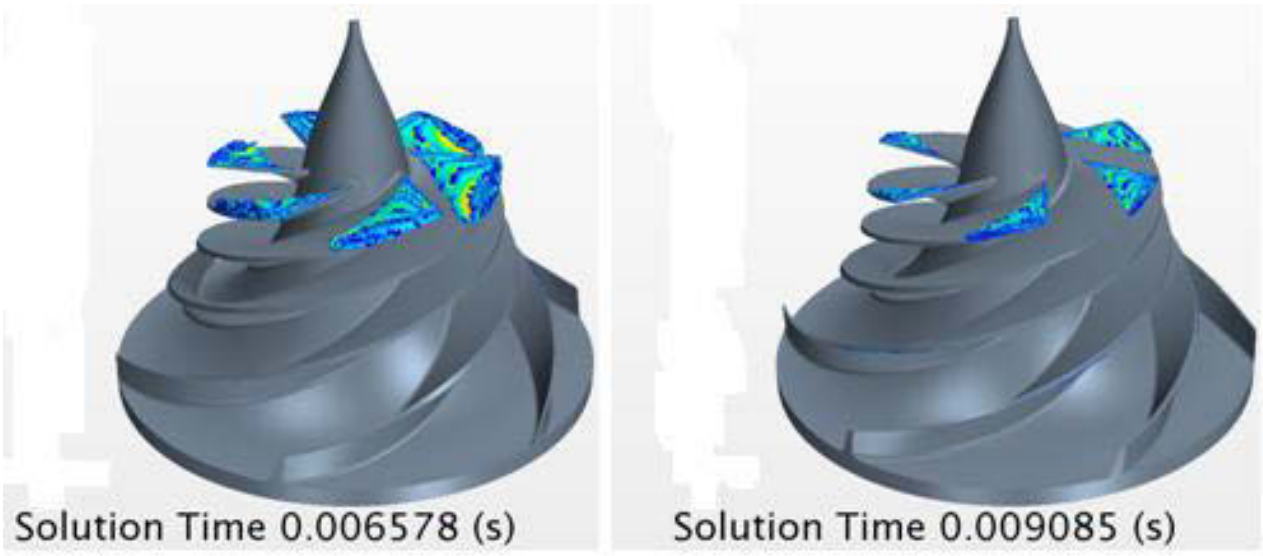

Figure 4.13: Presence of two phase flow at a) 0.006578 s and b) 0.009085 s

However, the oscillations get smaller as the amount of two phase flow levels out. Figure 4.14 shows the presence of cavitation at the fourth oscillation where the presence of two-phase flow has evened out. In other words, the area of the threshold at the trough (figure 4.14 (a)) is significantly smaller than that of figure 4.12 (a) (the first major decrease in pressure) and the size of the threshold at the peak has also increased. This levelling out of the area of the surface that is cavitating causes the pressure plot to stabilise as the flow blockage becomes more consistent.

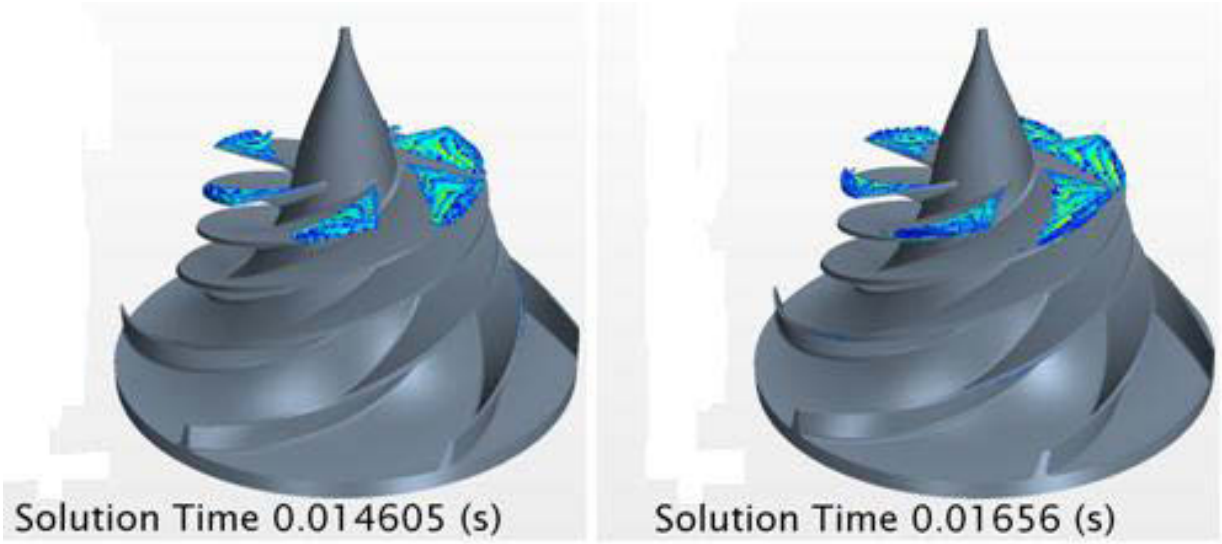

Figure 4.14: Presence of two phase flow at a) 0.014605 s and b) 0.01656 s

As expected, the cavitation developed on the leading edge of the impeller blades and propagated down the blade passage, effectively blocking and therefore affecting the flow incidence onto the blade leading edge and decreasing the pressure rise of the turbopump. Figure 4.15 shows the early signs of cavitation where the portion of two phase flow is minimal but has generated at the blade tip and along a narrow band at the leading edge. The pressure outlet in the presence of cavitation stabilises at roughly 45 b which is a 10.9 b decrease from the steady state model and an 11.63 b difference from the meanline prediction. Although the meanline data took into account cavitation through the use of a cavitation number defined in the meanline software as 0.087, the level of cavitation seen in the 3D model is greater than expected. The level of cavitation at the end of the fifth rotation can be seen in figure 4.16. This shows the predicted constant level of cavitation as the pressure output has almost reached a steady state.

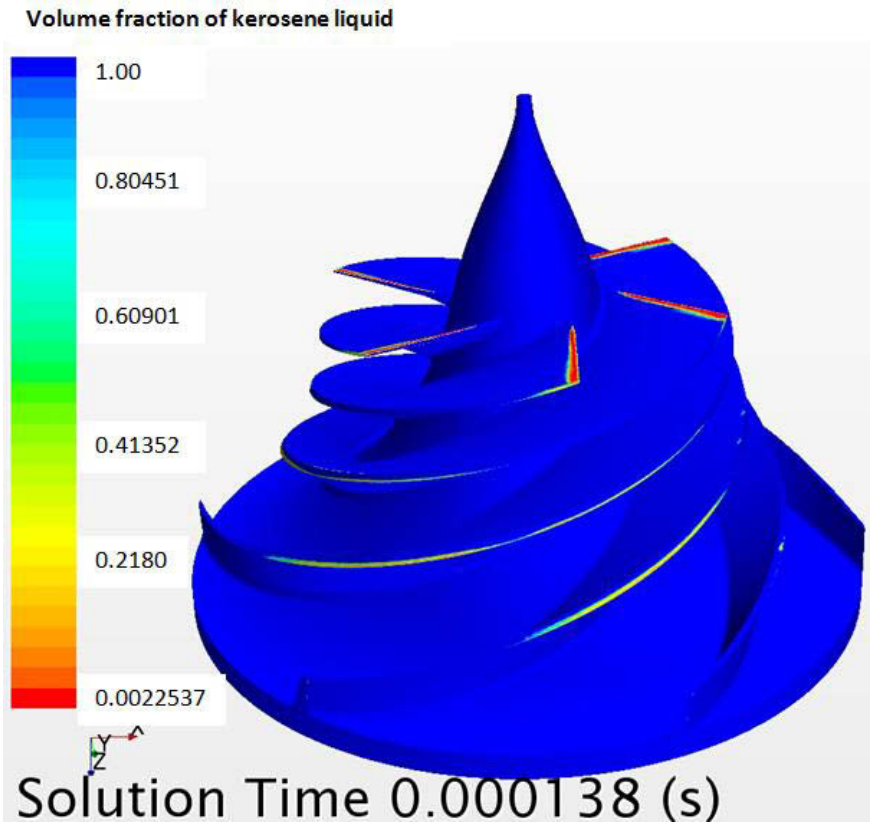

Figure 4.15: Early signs of cavitation

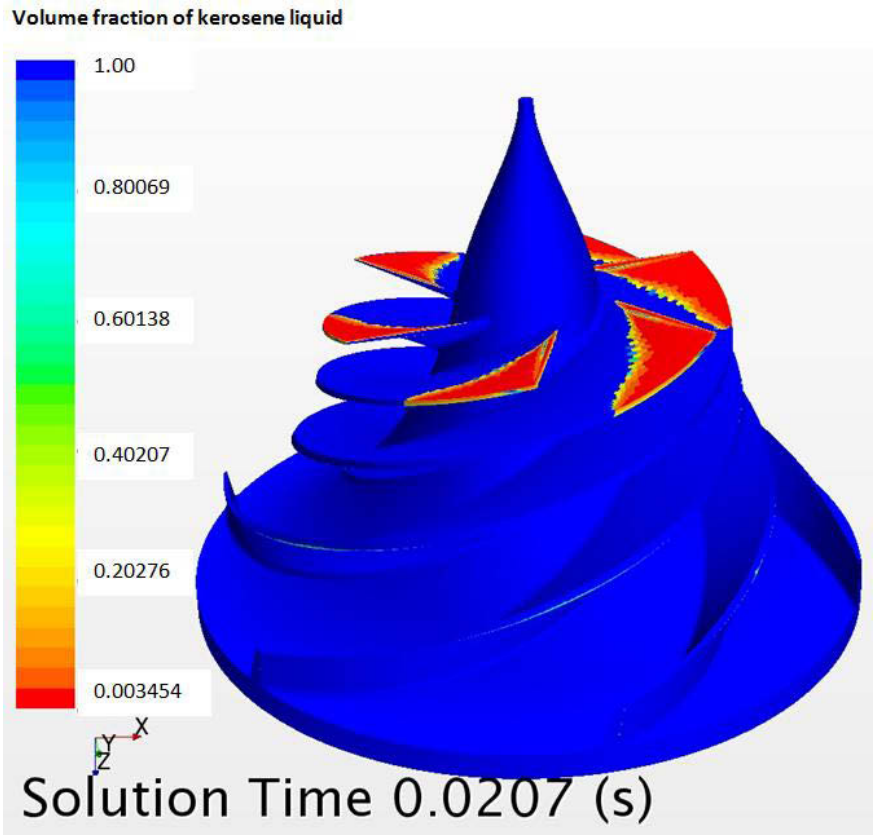

Figure 4.16: Stabilised cavitation level

5 Conclusion

The main aim of this work was to create a numerical model capable of predicting the behavior of two centrifugal turbopumps and in doing so to confirm an earlier meanline design of the impellers by Smyth (2013). Both the CFD models were constructed on the same principles and made use of the same models. Key factors in the CFD models were the turbulence model, the mesh optimization process as well as the time and motion models. This work forms part of a larger project aimed at developing a turbopump able to launch a hypothetical vehicle from a South African launch site. Although the manufacture of the scaled impeller has been completed; the experimental rig is being developed in a separate project and requires a redesigned volute before testing can begin. When the rig alteration is complete it will provide a third set of data for the scaled impeller and assist in the validation of the CFD model and the meanline design. Once the scaled CFD model is validated against test data in a future project, it will be indirectly validating the full scale model due to the fact that the two CFD models were developed using the same principles, turbulence and physics models. Therefore, by validating the scaled impeller design through experimental testing the validation of the meanline design for the full size turbopump can occur through the comparisons drawn between the numerical and meanline results.

5.1 Mesh Optimisation

The mesh process for the scaled impeller was more intense than for the full model since the computational cost to carry out a mesh study was lower in the scaled model. The mesh optimization process dealt with the tip gap of the model, which is the clearance gap between the blade and shroud wall, in great detail. The short study dealt only with the scaled impeller and the results were then used in the full size model. The study started with only polyhedral cells in the tip gap and then moved on to include prism layers which were increased in number. The original mesh of the scaled impeller only had 2 polyhedral cells in the clearance gap while the final mesh had 6 prism layers on the shroud wall, 2 polyhedral cells and then 6 prism layers on the blade, yielding 14 cells in the gap. The study found that this improvement of the gap mesh provided negligible change in result with the outlet pressure increasing by 2% between mesh 1 and 4. Due to the negligible change in result, the author did not define the tip gap of the full size model with as many cells. Instead, the full size model had only 9 cells in the gap, 3 prism layers on each wall and 3 polyhedral cells. Despite the low cell number in the gap, it is still an acceptable number of cells when compared to other similar studies.

The mesh optimization also dealt with the boundary layer mesh in that it focused on lowering the wall Y+ value to approximately 1. The Y+ value was decreased by reducing the near-wall prism layer thickness. This thickness was calculated using the shear stress on the impeller surface. Care had to be

taken to ensure the stretching of the prism layers was not too high. To overcome this issue, the prism layers were generated using the stretching factor method, to keep an acceptable stretching factor, until the Y+ was close to 1. Then, in the final mesh the near-wall layer was altered to bring the Y+ down to a low enough value. The effect of reaching such a low value was also found to be insignificant when predicting the global performance of the pump. Due to the minimal effect that this property had on the results, it was not enforced in the full scale model. Rather, in the full scale model the stretching factor method was used for all the mesh configurations and the number of layers was increased until an acceptable Y+ value was obtained. The overall prism layer thickness was taken from the scaled model. The wall Y+ was roughly 2.5 on the impeller surface of the full scale model. This is, however, an acceptable value when compared to other relevant studies in the literature.

This research has found that extensive refinement of the clearance gap between the blade wall and the shroud has little affect on the accuracy of the three dimensional model. If anything, the extensive refinement of the tip gap has a negative consequence for the CFD model as the computational time for the model increases with the number of cells in the model. As the tip gap is generally very small in shrouded impellers, the number of cells used to refine the gap is large. Therefore the increase on computational time is also great which takes away one of the advantages of computational analysis which is speed at which results can be obtained. The research also found that the reduction of the wall Y+ value to as low as 1 had no significant effect on the results of the numerical model. For this reason the second CFD model did not reduce the wall Y+ values as much as the first.

5.2 CFD Results

With regard to the prediction of the performance of the impellers, the scaled model was in good agreement with the meanline data for low flow rates as well as at the operating point. However, the scaled model failed to capture the characteristic head drop-off for the pump curve found in the meanline prediction. Despite this the full scale model provided a good correlation with the meanline data for all data points, with an average difference of only 5.18%.

Although the scaling laws were applied, some small geometric characteristics were altered by Smyth (2013) when attempting to achieve similar flow characteristics in terms of the blade loading. While the scaling process was aimed at keeping all flow characteristics similar the cavitation production in each impeller was vastly different. The original meanline design work showed that the scaled impeller had a blade cavitation number of 0.091 and the full scale impeller had a blade cavitation number of 0.087. This puts the cavitation performance of each impeller in a similar range and should be the case in the CFD models as the cavitation number originates from the inlet conditions of the pump, prescribed by Smyth (2013). The numerical model predicted otherwise. The scaled impeller showed

only a small amount of two phase flow while the full scale model showed a large presence of two phase flow which created a blockage and affected the performance of the pump. The pressure output of the full scale pump decreased by nearly 20% when the multiphase flow model was activated. This is a large difference when compared to the scaled impeller which showed almost no drop in performance. The scaled impeller showed a relatively constant level of two phase flow which led to a stable pressure plot as discussed. The presence of cavitation in the full size impeller however, was less stable and created an unsteady output. The oscillations of the pressure output however were decreasing and the pressure plot stabilizing after the fifth rotation of the impeller.

The difference in the behaviour of the impellers can possibly be attributed to the scaling process. While the scaling process looked to keep certain dimensionless coefficients constant to provide similar flow characteristics, the scaled design was altered geometrically to obtain a similar blade loading pattern. When comparing the geometry of the two impellers, it can be seen that the blades on the scaled impeller have a smaller wrap around angle. In other words the blades of the full size impeller pass through 247^{o} while the scaled impeller blades only wrap 211^{o} around the impeller. Naturally this affects the amount of time the fluid spends in the blade passage which will alter the characteristics of the flow from one impeller to the next. Cavitation scaling is very sensitive especially the inception of cavitation where scaling across different fluid mediums, speeds and geometric sizes produces many difficulties (Brennen, 1995). As previously stated, the three requirements described by Fox, et al., (2010) for accurate scaling are geometric, kinematic and dynamic similarity. Due to the larger wrap angles in the full size impeller, the geometric similarity of the model has been compromised.

As already stated the experimental testing on the scaled impeller has not yet been completed. This will provide an insight into the behaviour of the scaled impeller and produce a third set of results which can be used for verification of the meanline design as well as the CFD model. The experimental results will certainly shed light on the performance of the scaled impeller at high flow rates where the CFD model struggled to predict with sufficient accuracy the head drop-off. Despite the discrepancies at high flow rates, the CFD models performed well and provided a good idea of the behaviour of the impellers, whilst also offering an improved insight into the formation of cavitating flows for which no equivalent prediction or experimental data was available. Unfortunately the lack of experimental data has meant the comparison for the cavitation prediction has been limited. The experimental rig had aimed to have the capability to perform the appropriate testing for cavitation production. Had the test rig been ready and cavitation data been available the author could have compared the cavitation prediction for the scaled impeller more thoroughly.

While no experimental data were available for this project, confidence can be gained through the fact that the CFD model was developed using principles that have been verified (in similar studies) through experimental testing. Significant effort was expended to align the present work with computational analyses conducted elsewhere and validated experimentally.

5.3 Future Work

As this work forms part of a larger project to develop a liquid rocket engine there are various components still to be designed for the rocket booster engine. Currently research is focusing on a matched turbine design, using the overall vehicle parameters designed by Smyth (2013). Since the numerical predictions for the full size impeller show a pressure deviation of roughly 11 bar from the meanline design a solution needs to be found to ensure the fuel is at a high enough pressure. The presssure recovery can be solved in two ways.

The first involves a redesign of the impeller. Using the results of this study and going back to the meanline design, an optimisation can be done to ensure sufficient pressurisation of the fuel. However, recovering the loss of 11 bar would probably represent a formidable challenge.

The second method of ensuring the pressure outlet is high enough is to introduce an inducer into the system. An inducer is used to improve the cavitation performance of impellers. An inducer increases the static pressure of the liquid just before it enters the impeller. This allows an impeller to perform in a clean non-cavitating flow. Naturally, futher simulations would need to be done to confirm the performance of the pump with the inducer present.

However, before the redesign can occur the final phase of the turbopump programme must be completed to generate test data and validate the computational analysis. While the majorty of the test rig is complete and testing with the KSB impeller has been done to verify the rig, modifications to the rig are needed to fit the impeller of the turbopump. The KSB impeller is larger than the designed impeller so an insert into the volute is required to provide a better suited casing with a clearance of 0.5 mm as designed by Smyth (2013). To allow the study of cavitation to be done a viewing window needs to be implemented on the inlet section of the pipe. This is necessary to allow the formation of the cavitation vapour to be seen by the operator of the rig. Without proper visual confirmation of the cavitation it will be unclear as to where the cavitation has been formed and how far down the rotor passage the vapour bubbles travel. However, inserting the window is not an easy task. The pipe is curved so a normal transparent section of piping will distort the image. The window will also require proper sealing to avoid any leaks in the system.Another added diffilculty is the fact that there will be an inserted casing, as mentioned earlier, to allow the impeller to fit properly within the original pump

casing. Visual access will need to be obtained down the rotor passage to view the vapour bubbles moving down the blade passages. This means that the inserted modification will need to be designed with the viewing window in mind.

Once visual access has been obtained, a camera is needed to capture the cavitation production. As the numerical results show, the cavitation production occurs extrememly quickly. For accurate comparison, timestampped photographs would be required. These could then be compared to the timestamped scalar scenes of the two phase flow present in the CFD model. This data would then allow the proper validation of the CFD model of the scaled impeller. Once the validation of the scaled model is complete, confidence can be had in the accuracy of the full scale CFD model and the performance predicted by this numerical analysis.

6 References

Asnaghi, A., Jahanbakhsh, E. & Seif, M. S., 2010. Unsteady Multiphase Modelling of Cavitation Around NACA 0015. *Journal of Marine Science and Technology ,* 18(5), pp. 689-696.

Bacharoudis, E. C., Filios, A. E., Mentzos, M. D. & Margaris, D. P., 2008. Parametric Study of a Centrifugal Pump Impeller by Varying the Outlet Blade Angle. *The Open Mechanical Engineering Journal,* Volume 2, pp. 75-83.

Balasubramanian, R., Sabini, E. & Bradshaw, S., 2011. Influence of Impeller Leading Edge Profiles on Cavitation and Suction Performance. *Proceedings of the Twenty-Seventh International Pump Users Symposium.*

Barrio, R., Fernandez, J., Parrondo, J. & Blanco, E., 2010. Performance Prediction of a Centrifugal Pump Working in Direct and Reverse Mode Using Computational Fluid Dynamics. *International Conference on Renewable Energies and Power Quality,* March.

Brennen, C. E., 1995. *Cavitation and Bubble Dynamics.* New York: Oxford University Press.

CD-Adapco, 2013. *User Guide Star CCM+ Version 8.06.*

Davidson, L., 2011. *An Introduction to Turbulence Models,* Chalmers University of Technology, Goteborg, Sweden.)

De Beristain, I. G., 2012. *Aerodynamic Analysis of Fan Unsteady Simulations,* MSc Dissertation, University of the Basque Country, Leioa, Spain.

de Souza, A., 2013. *NAFEMS-CFD Jargon Explained.* [Online]
Available at: http://www.nafems.org/join/resources/cfdjargon/
[Accessed March 2013].

Dick, E., Vierendeels, J., Serbruyns, S. & Vande Voorde, J., 2001. Performance Prediction of Centrifugal Pumps with CFD-Tools. *Task Quarterly,* 5(4), pp. 579-594.

Ferziger, J. H. & Peric, M., 2002. *Computational Methods for Fluid Dynamics.* 3rd ed. New York: Springer.

Fox, R. W., Pritchard, P. J. & McDonald, A. T., 2010. *Introduction to Fluid Mechanics*. 7th ed. Hoboken: Wiley Publishers.

Franc, J.-P., 2006. *Physics and Control of Cavitation,* Educational Notes, University of Grenoble, Grenoble, France.

Hellstroom, F., Gutmark, E. & Fuchs, L., 2012. Large Eddy Simulation of the Unsteady Flow in a Radial Compressor Operating Near Surge. *Journal of Turbomachinery,* Volume 134.

Jafarzadeh, B., Hajari, A., Alishahi, M. M. & Akbari, M. H., 2010. The Flow Simulation of a Low-Specific-Speed High-Speed Centrifugal Pump. *Applied Mathematical Modelling,* Volume 35, pp. 242-249.

Liuzzi, D., 2012. *Two-Phase cavitation Modelling,* Ph.D Dissertation, University of Rome, Rome, Italy.

Lucius, A. & Brenner, G., 2010. Unsteady CFD Simulations of a Pump in Part Load Conditions Using Scale-Adaptive Simulation. *International Journal of Heat and Fluid Flow,* Volume 31, pp. 1113-1118.

Martensson, H., Andersson, S., Trollheden, S. & Brodin, S., 2008. Rocket Engines: Turbomachinery. *NATO R&T.*

Montomoli, F., Massini, M. & Salvadori, S., 2010. Geometrical Uncertainty in Turbomachinery: Tip Gap and Fillet Radius. *Computers and Fluids,* Volume 46, pp. 362-368.

Pope, S. B., 2000. *Turbulent Flows.* Cambridge: Cambridge City Press.

Qiu, X., Anderson, M. & Japikse, D., 2010. An Integrated Design System for Turbomachinery. *Journal of Hydrodynamics,* 22(5), pp. 358-365.

Ranade, V. V. & Krishnan, Y., 2002. CFD Predictions of Flow Near Impeller Blades in Baffled Stirred Vessels: Assessment of Computational Snapshot Approach. *Chemical Engineering Communications,* Volume 189, pp. 895-922.

Shojaeefard, M. H. et al., 2012. Numerical Study of the Effects of Some Geometric Characteristics of a Centrifugal Pump Impeller that Pumps a Viscous Fluid. *Computers and Fluids,* Volume 60, pp. 61-70.

Smyth, J., 2013. *The Design and Analysis of a Kerosene Turbopump for a South African Commercial Launch Vehicle,* MSc Dissertation, University of KwaZulu-Natal, Durban, South Africa.

SpaceX, 2011. *Why the US Can Beat China: The Facts About SpaceX Costs.* [Online]
Available at: http://www.spaceref.com/news/viewpr.html?pid=33457
[Accessed 11 September 2013].

Spence, R. & Amaral-Teixeira, J., 2009. A CFD Parametric Study of Geometrical Variations on the Pressure Pulsations and Performance Characteristics of a Centrifugal Pump. *Computers and Fluids,* Volume 38, pp. 1243-1257.

Sutton, G., 2006. History of Liquid Propellant Engines. *AIAA,* Reston, Virginia.

van der Merwe, B. B., 2012. *Design of a Centrifugal Compressor Impeller for Micro Gas Turbine Application,* MSc Dissertation, University of Stellenbosch, South Africa.

Viswanathan, A. K., 2006. *Detached Eddy Simulation of Turbulent Flow and Heat Transfer in Turbine Blade Internal Cooling Ducts,* Ph.D Dissertation, State University, Faculty of Virginia Polytechnic Institute, Virginia.

Westra, R. W., Broersma, L., van Andel, K. & Kruyt, N. P., 2010. PIV measurements and CFD Computations of Secondary Flow in a Centrifugal Pump Impeller. *Journal of Fluids Engineering,* Volume 132.

Wilcox, D. C., 1993. *Turbulence Modelling for CFD.* California: DCW Industries.

Zhu, B. & Chen, H.-x., 2012. Cavitating Suppression of Low Specific Speed Centrifugal Pump With Gap Drainage Blades. *Journal of Hydrodynamics,* 24(5), pp. 729-736.

7 Appendix A

Scaled Model Results:

Mesh 1 Results:			
Flow rate	**Meanline (bar)**	**CFD (bar)**	**Difference**
12.73	5.70	5.79	1.50%
15.46	5.23	5.56	5.92%
18.19	4.75	5.3	10.46%
20.92	4.19	5.07	17.32%
23.64	3.51	4.78	26.51%

Mesh 2 Results:			
Flow rate	**Meanline (bar)**	**CFD (bar)**	**Difference**
12.73	5.70	5.81	1.84%
15.46	5.23	5.59	6.43%
18.19	4.75	5.36	11.46%
20.92	4.19	5.08	17.49%
23.64	3.51	4.83	27.27%

Mesh 3 Results:			
Flow rate	**Meanline (bar)**	**CFD (bar)**	**Difference**
12.73	5.70	5.83	2.18%
15.46	5.23	5.61	6.76%
18.19	4.75	5.42	12.44%
20.92	4.19	5.2	19.39%
23.64	3.51	4.92	28.60%

Mesh 4 Results:			
Flow rate	**Meanline (bar)**	**CFD (bar)**	**Difference**
12.73	5.70	5.84	2.35%
15.46	5.23	5.62	6.93%
18.19	4.75	5.41	12.28%
20.92	4.19	5.18	19.08%
23.64	3.51	4.91	28.46%

Full scale results:

Mesh 1 Results:			
Flow rate (kg/s)	**Meanline (bar)**	**CFD (bar)**	**Difference**
72.3	66.82	63.71	4.88%
87.8	62.59	60.78	2.98%
103.29	56.63	57.44	1.41%
118.78	49.73	53.33	6.75%
134.27	43.37	48.58	10.72%

Mesh 2 Results:			
Flow rate (kg/s)	**Meanline (bar)**	**CFD (bar)**	**Difference**
72.3	66.82	63.54	5.16%
87.8	62.59	60.16	4.04%
103.29	56.63	56.43	0.35%
118.78	49.73	52.08	4.51%
134.27	43.37	47.16	8.04%

Mesh 3 Results:			
Flow rate (kg/s)	**Meanline (bar)**	**CFD (bar)**	**Difference**
72.3	66.82	63.61	5.05%
87.8	62.59	60.36	3.69%
103.29	56.63	56.55	0.14%
118.78	49.73	52.26	4.84%
134.27	43.37	47.41	8.52%

Mesh 4 Results:			
Flow rate (kg/s)	**Meanline (bar)**	**CFD (bar)**	**Difference**
72.3	66.82	62.82	6.37%
87.8	62.59	59.4	5.37%
103.29	56.63	55.9	1.31%
118.78	49.73	51.96	4.29%
134.27	43.37	47.43	8.56%